RIO

PUC

Tese de Doutorado

Multiscale elastostatic cloaking via static condensation

Vinicius Oliveira Fontes

Pontifícia Universidade Católica do Rio de Janeiro
Centro Técnico Científico
Departamento de Engenharia Mecânica (DEM)

Rio de Janeiro, 17 de Outubro de 2025

Pontifícia
Universidade
Católica do
Rio de Janeiro

Multiscale elastostatic cloaking via static condensation

Vinicius Oliveira Fontes

Orientador: Professor Anderson Pereira

Tese apresentada como requisito parcial para a obtenção do grau de Doutor em Engenharia Mecânica pelo programa de Pós-Graduação em Engenharia Mecânica, no Departamento de Engenharia Mecânica.

Rio de Janeiro, 17 de Outubro de 2025

Pontifícia
Universidade
Católica do
Rio de Janeiro

Multiscale elastostatic cloaking via static condensation

Vinicius Oliveira Fontes

Tese apresentada como requisito parcial para a obtenção do grau de Doutor em Engenharia Mecânica. Aprovada pela Comissão examinadora abaixo:

Professor Anderson Pereira
Orientador
Departamento de Engenharia Mecânica – PUC-RIO

Professor Ivan Fabio Mota de Menezes
Pontifícia Universidade Católica do Rio de Janeiro (PUC-Rio)

Professor Jessé Augusto dos Santos Paixão
Pontifícia Universidade Católica do Rio de Janeiro (PUC-Rio)

Professor Daniel Milbrath De Leon
Universidade Federal do Rio Grande do Sul (UFRGS)

Professor Pablo Andrés Muñoz Rojas
Universidade do Estado de Santa Catarina (UDESC)

Rio de Janeiro, 17 de Outubro de 2025

Pontifícia
Universidade
Católica do
Rio de Janeiro

Vinicius Oliveira Fontes
Graduou-se em Engenharia Mecânica pela Universidade Federal Fluminense (UFF) em 2018 e recebeu o grau de mestre em Engenharia Mecânica pela Pontífica Universidade Católica do Rio de Janeiro (PUC-RIO) em 2021.

Ficha Catalográfica

Fontes, Vinicius Oliveira

Multiscale elastostatic cloaking via static condensation / Vinicius Oliveira Fontes ; orientação: Anderson Pereira. – 2025.
124 f. : il. color. ; 30 cm

Tese (doutorado)–Pontifícia Universidade Católica do Rio de Janeiro, Departamento de Engenharia Mecânica, 2025.
Inclui bibliografia

1. Engenharia Mecânica – Teses. 2. Camuflagem mecânica. 3. Condensação estática. 4. Análise multiescala. 5. Otimização topológica. 6. Método dos elementos finitos. I. Pereira, Anderson. II. Pontifícia Universidade Católica do Rio de Janeiro. Departamento de Engenharia Mecânica. III. Título.

CDD: 621

Acknowledgments

I thank the Lord Jesus Christ, my family, my advisor Professor Anderson Pereira, and my colleagues. I am very grateful for my wife, Larissa, who endured long work days and restless nights working.

I also acknowledge the support from the Department of Mechanical Engineering of PUC-Rio, and the supporting agencies, FAPERJ and CAPES, for the aids granted, without which this work could not have been accomplished.

This study was financed by Carlos Chagas Filho Foundation for Research Support of the State of Rio de Janeiro (FAPERJ), Process SEI E-26/202.573/2022 (277082).
This study was financed in part by the Coordenação de Aperfeiçoamento de Pessoal de Nível Superior - Brasil (CAPES) - Finance Code 001.

Abstract

Fontes,Vinicius O.; Pereira, Anderson (Advisor). **Multiscale elastostatic cloaking via static condensation**. Rio de Janeiro, 2025. 124p. Tese de Doutorado – Departamento de Engenharia Mecânica, Pontifícia Universidade Católica do Rio de Janeiro.

Mechanical cloaking is the idea of hiding the influence of a hole in a structure by designing a surrounding region known as a cloak. Due to the complexity of this problem, many solutions to this problem proposed in the literature introduce some sort of multiscale topology optimization approach with mechanical metamaterials, i.e., materials that derive their properties from both their constituents and architecture. Great part of the approaches found in the literature presume scale separation using homogenization theory, despite its limitations, due to the prohibitive computational cost of analyzing complex multiscale structures. Moreover, the selection of type and density of candidate metamaterials is typically done with data-driven approaches that require a complex preprocessing and implementation. In this work, we developed solutions to mechanical cloaking inspired by the recent compatible boundary condition (CBC) paradigm, in which the cloaking device is optimized apart from the surrounding structure. First, we combined the discrete material optimization algorithm to select homogeneous candidates in the solution of an elastostatic cloaking problem using the CBC paradigm. Then, we solved a similar problem using our original bottom-up gradient-based multiple metamaterial optimization method, developed from a modified version of the discrete material optimization method. Additionally, our multi-material framework was adapted to the solution of a shape matching problem, displaying its versatility. Finally, we propose two ways in which static condensation can be explored in the future in the context of mechanical cloaking, including the design of unbiased cloaking devices and a CBC-based homogenizationless multiscale optimization method.

Keywords

Mechanical cloaking, static condensation, mutiscale analysis, topology optimization, finite element method.

Resumo

Fontes,Vinicius O.; Pereira, Anderson. **Camuflagem mecânica multiscala via condensação estática**. Rio de Janeiro, 2025. 124p. Tese de Doutorado – Departamento de Engenharia Mecânica, Pontifícia Universidade Católica do Rio de Janeiro.

Camuflagem mecânica é a ideia de ocultar a influência de um furo em uma estrutura, projetando uma região ao redor conhecida como manto. Devido à complexidade desse problema, muitas soluções propostas na literatura introduzem algum tipo de abordagem de otimização topológica multiescala com metamateriais mecânicos, isto é, materiais que derivam suas propriedades tanto de seus constituintes quanto de sua arquitetura. Grande parte das abordagens encontradas na literatura presume separação de escalas usando a teoria da homogeneização, apesar das suas limitações, dado o custo computacional proibitivo da análise de complexas estruturas multiescala. Além disso, a seleção do tipo e densidade de metamateriais candidatos é tipicamente feita com abordagens baseada em dados que requerem um preprocessamento e implementação complexos. Neste trabalho, nós desenvolvemos soluções para a camuflagem mecânica inspiradas no recente paradigma da condição de contorno compatível (CCC), no qual o dispositivo de camuflagem é otimizado separadamente da estrutura circunjacente. Primeiramente, nós combinamos o algoritmo de otimização discreta de material para selecionar candidatos homogêneos na solução de um problema de camuflagem elastostática usando o paradigma CCC. Em seguida, resolvemos um problema similar com o nosso metodo "bottom-up" original de otimização baseada em gradiente com múltiplos metamateriais, desenvolvido a partir de uma versão modificada do método de otimização discreta de material. Adicionalmente, nossa estrutura multimaterial foi adaptada para para a solução de problemas de correspondência de forma, demonstrando sua versatilidade. Finalmente, nós propomos duas formas como a condensação estática pode ser explorada no futuro no contexto de camuflagem mecânica, incluindo o design de mantos não enviesados e um método de otimização multiescala baseado no CCC e sem homogenização.

Palavras-chave

Camuflagem mecânica, condensação estática, análise multiescala, otimização topológica, método dos elementos finitos.

Table of contents

List of figures

List of tables

List of Abbreviations

CBC – *Compatible Boundary Condition*

CFD – *Central Finite Difference*

CSM – *Complex Step Method*

DCP – *Discrete-Continuous Parameterization*

DLT – *Direct Lattice Transformation*

DMO – *Discrete Material Optimization*

DOF – *Degree of Freedom*

FEA – *Finite Element Analysis*

FEM – *Finite Element Method*

FFD – *Forward Finite Difference*

MMA – *Method of Moving Asymptotes*

Q4 – *4-node Quadrilateral*

RMSE – *Root Mean Square Error*

RUC – *Repeating Unit Cell*

RVE – *Representative Volume Element*

SEM – *Superelement Method*

SIMP – *Simplified Isotropic Material with Penalization*

TO – *Topology Optimization*

List of Symbols

Math Operators

$\cdot$	Single contraction operator
$:$	Double contraction operator
$\|\|\bullet\|\|$	Euclidian norm operator

Continuum Mechanics

$\boldsymbol{e}_i$	Basis vector in the i-th direction
$\boldsymbol{X}$	Initial position vector (material coordinates)
$\boldsymbol{x}$	Initial position vector (spatial coordinates)
$\boldsymbol{u}$	Displacement vector
$\boldsymbol{v}$	Velocity vector
$\boldsymbol{I}$	Second-order identity tensor
$\boldsymbol{F}$	Deformation gradient tensor
$\boldsymbol{C}$	Right Cauchy-Green deformation tensor
$\boldsymbol{E}$	Green-Lagrange strain tensor
$\boldsymbol{\varepsilon}$	Small-deformation strain tensor
γ_{ij}	Component ij of the shear deformation strain tensor
$\boldsymbol{n}$	Normal vector
$\boldsymbol{t}^{(n)}$	Traction vector on surface with normal $\boldsymbol{n}$
$\boldsymbol{\sigma}$	Cauchy stress tensor
$\boldsymbol{b}$	Body force vector per unit mass
$\boldsymbol{\mathcal{C}}$	Elastic constitutive tensor

Finite Element Method, Homogenization and Static Condensation

Ω	Domain of the structure

Γ	Boundary of the domain
$\delta\Pi$	Virtual work functional
$\mathbf{u}, \delta\mathbf{u}$	Displacement solution vector: trial and test
$\boldsymbol{\xi}$	Vector of natural coordinates
N_k	k-th interpolation function
$\mathbf{J}$	Jacobian of the transformation
$\mathbf{B}$	Strain-displacement matrix
$\mathbf{K}$	Stiffness matrix
$\mathbf{f}$, $\mathbf{f}^b$, $\mathbf{f}^s$	External load vector: total, body forces and surface traction
$\mathbf{I}$	Identity matrix
$\overline{\sigma}_{ij}$, $\overline{\varepsilon}_{ij}$	Component ij of volume-averaged tensors: stress and strain
$\mathcal{C}^H_{ijkl}$	Component $ijkl$ of the homogenized elasticity tensor
$\mathcal{C}^H_{ij}$	Component ij of the homogenized elasticity tensor (matrix form)
$c_{ij,n}$	n-th curve-fitted interpolation coefficient of $\mathcal{C}^H_{ij}$
m, s	Master and slave degrees of freedom
$\mathbf{f}_R$, $\mathbf{K}_R$	Reduced force vector and stiffness matrix

Properties, Geometry and Loads

ρ	Density
E	Young modulus
ν	Poisson's ratio
L, H, t	Geometric dimensions: length, height and thickness

Optimization and Mechanical Cloaking

Ω_{ref}, Ω_{sur}, Ω_{hole}	Partitions of the structure domain: reference, surrounding and hole
Γ_{in}, Γ_{out}, Γ_{BC}	Partitions of the structure domain's boundary: inner, outer and "boundary condition"
$z_m^{(e)}$	Design variable associated with candidate material m of element e
$y_m^{(e)}$	Filtered variable associated with candidate material m of element e

$\mathcal{F}$	Objective function
g_i	i-th constraint function
λ_i	i-th lagrnage nmultiplier
$\mathcal{L}$	Langragian
$\mathbf{W}$	Weight function for displacement error objective function
$\Delta\mathbf{u}_{\text{out}}$, $\Delta\mathbf{f}_{\text{out}}$	Nodal displacement and nodal force error at the outer boundary
$\mathbf{z}$	Multi-material optimization design variable vector
$\boldsymbol{\rho}$	Multi-material optimization density vector
$\boldsymbol{\xi}$	Multi-material optimization material fraction vector
$w_i^{(e)}$	DMO weight component of element e and candidate i
$\overline{w}_i^{(e)}$ or $\phi_i^{(e)}$	DMO normalized weight component of element e and candidate i
$\overline{\mathbf{w}}^{(e)}$, $\mathbf{C}_{ij}^{(e)}$	DCP vectors of weights and elasticity tensors of element e
r_{filter}	Filter radius
q	Filter exponent
$w_{e,i}$	Filter weight for elements e and i
β_{ini}, β_{max}, β_{frq}	Projection sharpness parameter: initial and maximum values, and update frequency
η	Projection Threshold parameter
p	SIMP penalization parameter

For which of you, intending to build a tower,
sitteth not down first, and counteth the cost,
whether he have sufficient to finish it?

Luke 14:28, *The Holy Bible (King James Version).*

1
Introduction

Mechanical structures are devices for channeling loads, and they are the fundamental piece of study of the structural engineer. Bontempi et al. (2008) divided structural problems into two categories, namely:

A direct problem is an analysis that evaluates the structural response in a given design environment using an appropriate model that takes into account all relevant boundary conditions.

An inverse problem consist in finding the geometric and mechanical features of a model for which the response is already known.

Structural design is an inverse problem that can be defined as the process whereby an engineer creates a structure with geometry and properties suitable for a specific application while adhering to realistic design limitations. The introduction of numerical optimization to structural analysis resulted in the now well-known discipline of numerical structural optimization which now comprises a broad collection of tools, including parametric, shape and topology optimization (TO). The well-established TO literature like Sigmund and Maute (2013) span several applications including but not limited to compliance minimization and stress constraints (Bruggi and Duysinx, 2012), buckling problems (Ferrari and Sigmund, 2019), vibration problems (Zargham et al., 2016), compliant mechanisms (Sigmund, 1997), and crashworthiness (Patel et al., 2009). The wide range applications and complexity of topology optimization has been acknowledged in the literature, for instance:

> To date, topology optimization has proven to be the most beneficial, yet most complex, structural optimization technique available to engineers and scientists. (Munk et al., 2019)

In 2006, Leonhardt (2006) published an article on optical cloaking, which spurred renewed interest in the scientific community in developing physical cloaks. In this context, cloaking an object means to conceal it with respect to a physical field, i.e., neglect its influence in the surrounding region, so it appears as if the object was not there. In optics, the main application is to make an object effectively invisible by distorting the light rays around it. At the same time, Pendry et al. (2006) proposed to use metamaterials for generating the rich distribution of properties required in the design of these optical cloaks. In our work, we define metamaterials as materials whose effective properties are derived freom their architecture at a smaller (possibly microscopic) scale as well as their constituents.

The concept of cloaking has ever since been extended to other areas of physics, such as mechanics. A mechanical cloaking device is the region around a hole that reduces its impact on the surrounding displacement field. In our work, we classify mechanical cloaking in a wider class of **target behavior** problems, which can be divided into the two following categories.

Shape matching is the type of problem where a structure must deform according to a predefined shape when subject to a given boundary condition. Applications of shape matching are found in cases where a arbitrary mechanical behavior is already known, such as in the design flexible link of soft robots that deforms precisely when subject to a mechanical load as an input.

Mechanical cloaking is the type of problem where the original mechanical behavior (e.g. , displacement field) of a structure is recovered after the introduction of a structural feature (e.g. , a hole) by designing a mechanical cloak that surrounds said feature. While not ubiquitous as other types of TO problems, mechanical cloaking can be used primarily to reinforce already designed or built structures, as tunnel shafts. However, an arguably more interesting application can be used to modify specific parts of bigger structures without affecting the mechanical behavior of its surrounding, such as introducing an additional window to an aircraft fuselage.

Despite their fundamental differences, both shape matching and mechanical cloaking can be addressed using the same numerical TO formulation: minimize the error between a target and current displacement field when subjected by known boundary conditions. Conceptually, their difference is the source of this target displacement field and the design region. Typically, the target displacement in mechanical cloaking problems is the displacement field of a reference structure without a hole, and the design region is a region around the hole. In shape matching problems, the target displacement (both values and degrees of freedom) and design region are arbitrary, such that the objective is that the structure deforms in a certain way when loaded. These concepts as illustrated in Figure 1.1.

Even in the linear elastic quasi-static condition adopted in this study, referred to as an elastostatic setting, it is challenging to distribute material around a hole such that the entire displacement field of the surrounding structure matches that of another structure (the one without the hole). The design space can be expanded by either introducing different candidate materials (Fachinotti et al., 2018) or utilizing mechanical metamaterials (Wang

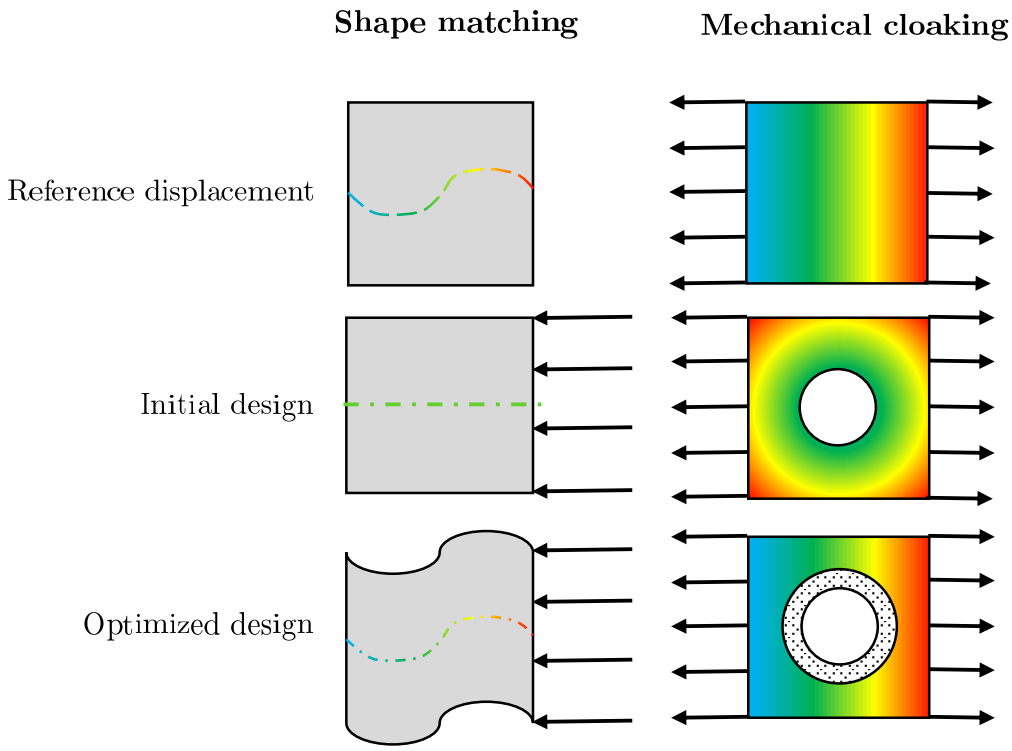

Figure 1.1: Elastostatic target behavior problems can be classified as shape matching (left) or mechanical cloaking (right). The reference displacement field (top row) must be approximated by modifying the initial design (middle row). The optimized multiscale structure in the design domain is represented as a square grid (bottom row).

et al., 2022). It is challenging to make a continuous multi-material structure, which may yield compatibility issue in both the structural optimization and manufacturing steps of design. Likewise, mechanical materials require an appropriate multiscale structural analysis framework, to accurately predict the influence of the microstructural architecture on the structural response at macroscopic level.

The combination multiscale analysis and structural optimization led to the development of multiscale optimization methods, most of which rely on homogenization theory. From the topology and properties of a microstructure, we can determine macroscopic behavior by assuming two hypotheses: ideal separation of macro and micro scales, and infinite repetition of the microstructure at a macroscopic material point (infinite periodicity). In practice, these multiscale structures are often fabricated utilizing additive manufacturing, in which neither of these assumptions are sufficiently satisfied, drastically affecting the cloaking performance of the optimized design as-built.

Another concern with aperiodic multiscale structures is the enforcing the connectivity of adjacent microstructures. To address this problem, a data-driven solution proposed by Schumacher et al. (2015) to generate a distribution

of compatible metamaterials, which has been extend to TO applications like shape matching (Wang et al., 2020b).

On top of the difficulties intrinsic to topology optimization, the high sensitivity to disturbance found in mechanical cloaking problems and challenges from multiscale analysis make this a worthy problem. It can be stated that currently there is no solution to mechanical cloaking in the literature (including our work) that presents all of the following desirable features when scaled to larger problems: numerical accuracy, computational efficiency, and fabricability. For instance, homogenization-based data-driven approaches sacrifice numerical accuracy in favor of faster solutions (once the machine learning training is finished) and manufacturability (from compatible designs). In these cases, the loss of performance comes from the aperiodicity required to expand the design space. While these issues can be addressed by smoothing the transition between adjacent microstructures (Chan et al., 2022), this does not fully solve the problem, and it increases its complexity. While these solutions have their applications, they may not be currently scalable depending on the application.

As a result of these many difficulties, many optimized multiscale structure articles do not give a sufficient validation of the results in a refined full scale analysis (i.e., without dividing the scales), let alone experimental results. It is worth noting that experimental results for the classic mechanical cloaking problem shown in Figure 1.1 may be biased, as simply reinforcing the hole with a reasonable amount of material may significantly reduce the influence of the hole. This occurs because reinforcing a hole is part of the process of cloaking its impact on its surrounding, so a clear distiction between these two concepts is fundamental, as discussed by Senhora et al. (2025).

In our work, we proposed an efficient integrated framework for the solution of the elastostatic cloaking problem. Inspired by the compatible boundary condition (CBC) paradigm (Cheng et al., 2023), we present a formulation based on static condensation, which permits us to design a cloak apart from the surrounding structure. In the elastostatic case, this yields a discretized formulation of the CBC paradigm, which enforces the compatibility of the force and displacement fields at the cloak-surrounding interface as a necessary condition for the cloaking problem. Here, we implement this paradigm with multiple candidate materials and metamaterials. Our multiple metamaterial framework is a data-driven approach, but it does use homogenization for finding effective mechanical properties. Lastly, we also discuss how static condensation can be further exploited to design unbiased cloaks, those that work for virtually any loading case. Numerical results show the effectiveness of our methods, with a discussion weighing the pros and cons

of each method, and a comparison with the literature when applicable.

1.1 Objectives

Our general objective in this work is "to develop an efficient topology optimization method for the design of multiscale structures in the mechanical cloaking problem".

Our specific objectives can be detailed as follows:

- Review the state of the art of multiscale topology optimization applied to the solution of the mechanical cloaking problem;
- Develop a multi-material approach for mechanical cloaking and shape matching;
- Test all of these methods with benchmark problems and compare their results with the literature.

1.2 This work's contributions

In this work, we present the following original contributions:

- A novel discrete-form derivation of the CBC paradigm is presented, and extended to shape matching problems
- A multi-metamaterial selection algorithm is developed by adapting the discrete-continuous paradigm to the simultaneous optimization of microstructural family and density

Additionally, we proposed novel extensions to the application of static condensation to the development of unbiased cloaks and microstructure design without homogenization.

1.3 Outline

This manuscript is organized as follows:

- Chapter 2 reviews relevant works in multiscale topology optimization and mechanical cloaking, including the current state of the art;
- In Chapter 3, we review the fundamentals of continuum, finite element analysis, homogenization theory, and numerical optimization relevant to this work;

– Chapter 4, we present our approach to mechanical cloaking based on static condensation, and its extensions to unbiased cloaks;

– Chapter 5 introduces our multi-material homogenization-based mechanical cloaking method;

– Chapter 6 shows our numerical results and discussion;

– Chapter 7 ends with our final remarks and suggestions for future works.

2
Previous Work

In this chapter, we review works related to topology optimization and mechanical metamaterials, followed by the research on mechanical cloaking and shape matching. We finish this chapter reviewing papers on the use of static condensation and related techniques to topology optimization.

2.1
Inception and development of numerical topology optimization

The fundamental problem in TO-based structural design is determining how to distribute material in a domain in such a way that it optimizes a specific performance metric. In general, a mono-scale topology optimization could be posed as the optimization problem

$$\min_{\boldsymbol{\rho}} \quad \mathcal{F}(\boldsymbol{u}(\boldsymbol{\rho}), \boldsymbol{\rho}) \tag{2-1a}$$

$$\text{s.t.} \quad g_i(\boldsymbol{u}(\boldsymbol{\rho}), \boldsymbol{\rho}) \leq 0 \tag{2-1b}$$

$$\rho(\boldsymbol{x}) \in \{0, 1\}, \quad \forall\, \boldsymbol{x} \in \Omega\ , \tag{2-1c}$$

where $\mathcal{F}$ is the objective function, g_i are the constraints, and both may depend on the displacement field $\boldsymbol{u}$ and the material distribution represented by a density variable ρ. At each point $\boldsymbol{x}$ in the design domain Ω, the density represents either the absence of material ($\rho = 0$) or its presence ($\rho = 1$). Consider that the domain has been discretized into a suitable finite element mesh, and structural response is obtained with Finite Element Analysis (FEA).

The first work in numerical topology optimization is often attributed to Bendsøe and Kikuchi (1988). They suggested using a composite material that could be described by a locally periodic microstructure whose features are described by its smallest repeating part, the repeating unit cell (RUC). The density of the unit cells with previously defined topologies would define a family of microstructures whose effective properties could be computed via homogenization and interpolated, as illustrated in Figure 2.1, which includes the influence of the rotation of the unit cell. In practice, the density was allowed to continuously change between 0 and 1, relaxing the box constraint in Equation (2-1c) and enabling the use efficient gradient-based algorithms instead of prohibitively expensive integer programming.

The steps in the topology optimization with homogenization can be summarized into five steps (Bendsøe and Kikuchi, 1988):

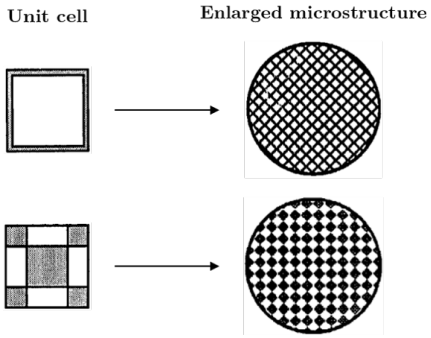

(a) RUC of a porous microstructure.

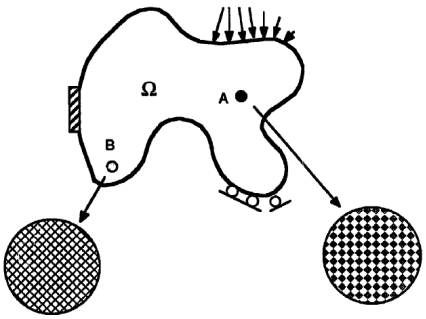

(b) Problem domain with spatially-varying properties due to microstructures at different points.

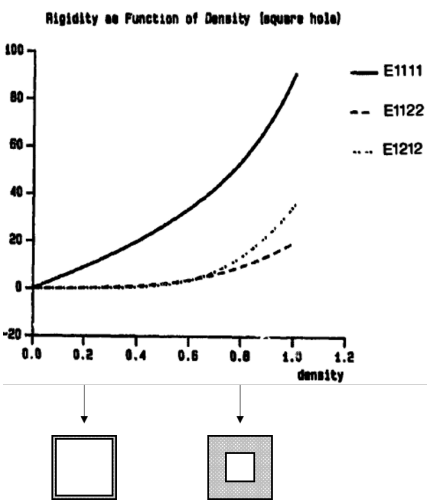

(c) Effective properties as a function of density.

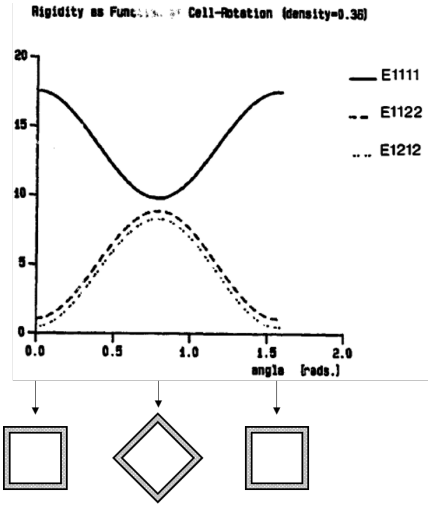

(d) Effective properties as a function of rotation

Figure 2.1: Homogenization-based topology optimization proposed by Bendsøe and Kikuchi (1988).

1. Select a domain and boundary conditions that accurately describe the structure and whose structural response can be examined using FEM.

2. Choose a composite material whose geometric properties can be defined as a continuous function of a set of parameters, such as density and unit cell rotation.

3. Define the effective material properties as a function of the previous step's parameters. This can be accomplished in a number of ways, for example:

   – From a data set obtained through homogenization for several density values, the material properties can be written as analytical functions of the density using interpolation or curve fitting.
   – "Rotating" the elasticity tensor with transformation matrices can be used to consider unit cell rotation.

4. Compute the optimal set of parameters at each element to minimize a chosen objective function, using an optimization algorithm.

5. Interpret results to define an "appropriate" optimal shape.

Although this homogenization-based topology optimization laid the foundation for this field, its results required "interpretation" in the last step since they were hardly manufacturable. To that end, some sort of post-processing results such as using a de-homogenization method developed later (see Figure 2.2).

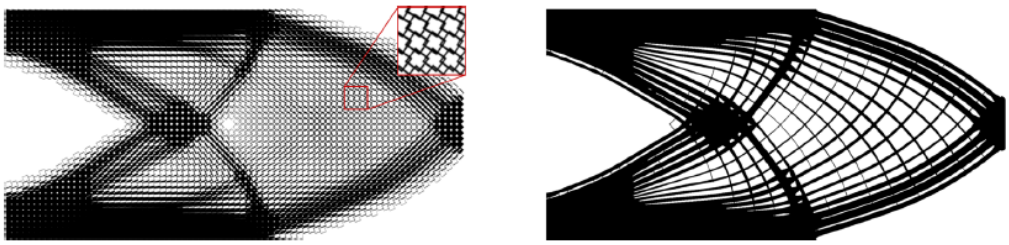

Figure 2.2: Optimized Michell cantilever beam: original solution using unit cells (Bendsøe and Kikuchi, 1988) (left); de-homogenized design (Groen and Sigmund, 2018) (right).

The relaxation of the density in this homogenization-based approach to topology optimization implicitly addressed the lack of solution in the minimization problem stated in Equation (2-1). However, most approaches developed since are **mono-scale**, that is, each finite element is either fully occupied by the candidate material or not. In practice, this means that the optimal density values are either 0 or 1 (even if the density may assume intermediate values during the optimization process). This restriction leads to some well-known problems, e.g. checkerboard patterns and mesh-dependent designs, that are often solved using mathematical techniques such as filters and projections. Bendsøe and Sigmund (2002) presented an excellent review on the main approaches to topology optimization, dividing them into the five categories shown in Table 2.1.

The power-law often used in density-based methods is more commonly known as the simplified isotropic material with penalization (SIMP) or solid isotropic microstructures with penalty (Mlejnek, 1992), and is one of the most common tools used in the literature and commercial software, e.g. Abaqus (Smith, 2015). Many educational SIMP-based codes spurred from two well-known references (Wang et al., 2021): `top99` (Sigmund, 2001) and `PolyTop` (Talischi et al., 2012). The structural analysis and optimization codes developed for this work were based on `PolyTop` and its extensions.

Table 2.1: Original implementation of the main approaches to topology optimization

Name and Reference	Description
Density-based (Bendsøe, 1989)	The density of each element is used as a design variable in an optimization algorithm. A "power-law" is often used to steer the density to 0 or 1 values.
Evolutionary (Xie and Steven, 1993)	Material is removed where a rejection criterion (*e.g.*, von Mises stress) is below a given ratio. The current design evolves at each iteration until a convergence criterion is met.
Topological derivatives (Sokolowski and Zochowski, 1999)	The influence on the objective function with the introduction of a hole at a specific point is computed as a derivative to find the best location to introduce a hole.
Level set (Allaire et al., 2002)	The optimized structure is the domain where a level set function is positive. This function is updated according to a differential equation that evolves the boundaries of the current design.
Phase field (Bourdin and Chambolle, 2003)	Optimal density distribution is obtained as the solution to the minimization of a functional containing a double well function that naturally penalizes intermediate densities.

2.2 Applications and modeling of mechanical metamaterials

Metamaterials are materials whose properties come from both their constituents and their architecture, with geometric features commonly found at the microscale and nanoscale. The structural hierarchy found in these materials are often exploited by reducing their size at nanoscale to exhibit unusual properties, e.g., "ultrahigh strength-to-density ratios, extraordinary resilience, and energy absorption with brittle constituents" (Surjadi et al., 2019). A review by Surjadi et al. (2019) states that mechanical metamaterial is a concept that spans a variety of materials. For instance, ultralight thin-walled nanolattices may "transform a strong and dense brittle ceramic into a strong, ultralight, energy-absorbing, and recoverable metamaterial" (Meza et al., 2014), as shown in Figure 2.3.

The unusual metamaterial properties that come when material size is

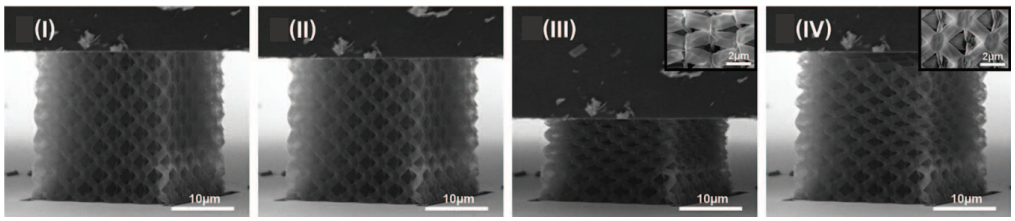

Figure 2.3: Compression test on a thin-walled ceramic nanolattice (from I to IV) displays higher recoverability of some ceramic metamaterials (Meza et al., 2014).

reduced below a certain scale is called the "size-effect", like strong-yet-ductile metallic glasses (Jang and Greer, 2010), for example. However, creating multi-scale structures with space-varying properties that leverage such properties is still a challenge, because the size-effect typically occurs when features are below submicron length scales (Schwaiger et al., 2019). While applications with mechanical metamaterials already exist, there are difficulties in designing these multiscale structures due to their high computational cost in simulation and optimization, as reviewed in the following section.

Another challenge in the application of these topologically complex multi-scale structures is simulating its mechanical behavior using finite element analysis (FEA). Analyzing structures with a single domain that considers all geometric features spanning multiple scales, that is, a **full-scale analysis**, carries a prohibitive cost due to their sheer size and complexity. Alternatively, one may separate the scales with a **multiscale analysis**, greatly reducing computational time.

In the context of the finite element method (FEM), multiscale analysis can be done in different ways, including but not limited to: constructing special multiscale base functions as done in the multiscale finite element method (Hou and Wu, 1997); or solving a boundary condition problem at each integration point of the macroscale, i.e., the multilevel finite element (Feyel, 2003). The multiscale finite element method does not separate the scales explicitly, can be extended to more complex nonlinear problems Efendiev et al. (2004), and has been used in structural optimization of periodic microstructures (Liu et al., 2018).

In practice, effective properties of materials with complex microstructures (typically composites) can be approximated by homogenization, a method based on variational approaches (Hashin and Shtrikman, 1963) that estimate these properties from a boundary value problem with periodic boundary condition. In the context of composites, the domain of this problem must be a sufficiently large to represent the behavior of the material, and it is called the **representative volume element** (RVE). There are two main assumptions

adopted in homogenization (Torquato and Haslach Jr, 2002): that the heterogeneities are periodic and in a separate (much smaller) scale compared to the macroscale. Overall is a powerful tool since it allows the designer to know effective properties of a initially complex structure, like synthetic bone implants (Hollister, 2005), articular cartilage implant (Kemppainen and Hollister, 2010), and wax scaffolds for bone tissue (Dias et al., 2012).

Real metamaterials are not infinitely periodic with perfect scale separation as assumed by homogenization theory, which may yield a significant divergence between the actual structural behavior and its response obtained in a finite element analysis (Hollister and Kikuchi, 1992). Despite this lower accuracy, homogenization is still used in concurrent multiscale design using mechanical metamaterials due to its acceptable error margins, especially when "the gradient of material properties is sufficiently small" (Garner et al., 2019).

2.3 Topology optimization of multiscale structures

Topology optimization of multiscale structures is a wide research field owing to the many ways it can be executed. Wu et al. (2021) reviewed several approaches presented in the literature classifying them based on how restricted unit cell design is. We summarize their classification in what follows:

I **Optimal set of elasticity tensor**: A geometry parameterization is performed to find the optimal distribution of properties, which can be found with rank-N laminates;

II **Unrestricted unit cell design**: The microstructure of each element is optimized concurrently with the macrostructure;

III **Restricted unit cell design**: Same as the previous category, but restrictions are applied, typically to ensure connectivity of neighbouring unit cells, while limiting design freedom;

IV **Parameterized unit cell with multiple parameters**: The properties are precomputed in a database of parameterized families of unit cells with more than one parameter, where one is usually unit cell rotation;

V **Parameterized unit cell based on density**: Same as the previous category, but with only a single parameter, the unit cell density.

This classification is complemented by defining whether the density values in the structure are (A) unrestricted, (B) restricted, or (C) fixed. Notice that even if density is fixed, topology optimization can be performed, e.g. by

selecting different microstructures from a database, or by rotating the unit cell. At this point, we clarify that the term metamaterial can be used to describe these microstructures when they are part of a database (Bastek et al., 2022), but many authors may refer to them as simply microstructures depending on the context.

A vast majority of multi-scale topology optimization use homogenization to separate the scales as reviewed in the previous section, and two related methods are important within the same context:

Inverse homogenization consists in finding a microstructure for given homogenized material properties (Sigmund, 1994);

De-homogenization is essentially finding an equivalent high resolution mono-scale structure of an optimized multi-scale structure during post-processing (Pantz and Trabelsi, 2008).

Inverse homogenization can be used either to separate the scales in concurrent topology optimization (categories II and III) or to create the database of microstructures with specific properties in categories IV and V. De-homogenization is often applied to generate mono-scale structures from multi-scale topologies that contain optimal unit cell rotation. The reader is referred to the aforementioned review for many examples of works in each category (Wu et al., 2021).

In the last decade, a data-driven approach has been introduced to multi-scale design and adapted to topology optimization. This approach was suggested by Schumacher et al. (2015) who developed a database of families of microstructures, that were then used to place optimal candidates to approximate a target property distribution in a structure with predefined topology (see Figure 2.4). Since these families of microstructures would overlap in the property space, they developed an algorithm to select the best candidate that would enforce connectivity of neighbouring microstructure. Additionally, the precomputed database ensured all microstructures were fabricable with additive manufacturing, but the numerical coarsening approach (Kharevych et al., 2009) adopted (instead of the typical homogenization) yielded significant error in laboratory tests, which was also affected by the aperiodic tiling with high density gradient.

This data-driven approach has gained some traction and typically is implemented with some form of machine learning algorithm (e.g. deep neural networks) in the inverse design of an enriched database of metamaterials (Bastek et al., 2022). For instance, Wang et al. (Wang et al., 2020b) applied it to multiscale topology optimization with a database that spanned a wide range

Figure 2.4: Multi-scale structure created with data-driven design by matching soft (blue) and stiff (red) microstructures. Left to right: target properties, optimized design and structure fabricated with laser sintering (Schumacher et al., 2015).

of mechanical properties that was achieved by smoothly modifying a smaller set of unit cells used as the initial seeds. The implementation of this approach to topology optimization is often done in **two stages**, namely: (1) finding the distribution of optimal properties in the design domain; (2) finding the optimal microstructure that better approximates the target properties found in the previous step.

Wang et al. (2020b) also introduced two convenient categories for defining optimization frameworks: **top-down**, where the unit cells are created to approximate precomputed macroscopic loads; and **bottom-up**, in which the unit cells come from an existing parameterized database of similar shapes. In other words, a multiscale optimization framework is classified as either bottom-up or top-down depending on whether the unit cells are designed prior to or after the main optimization process, respectively.

In stark contrast to data-driven approaches, some authors suggested using a limited database of metamaterials, focusing on fabricability and perfomance, and a deterministic (instead of data-driven) approach for material selection. A recent example is shown in Figure 2.5 for an optimized cantilever beam built with two metamaterial families.

In order to fabricate multi-scale structures, enforcing compatibility of neighbouring unit cells is paramount to avoid disconnected geometric features. This problem is particularly pronounced in the so-called top-down frameworks with unrestricted cell design, though bottom-up frameworks such as the one initially proposed by (Bendsøe and Kikuchi, 1988) do not intrinsically enforce any connectivity either. A non-exhaustive list of methods that enforce connectivity is shown in table 2.2, in which we suggested the method's name

when it was not clearly stated by the reference.

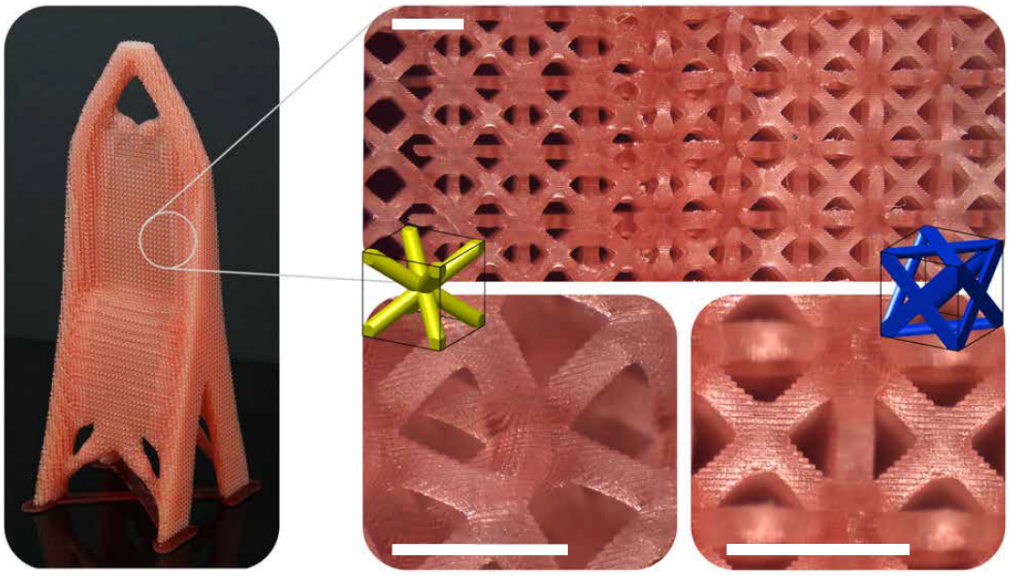

Figure 2.5: Optimized cantilever beams with two candidate metamaterials (Sanders et al., 2021b).

Table 2.2: Methods proposed in the literaturre to enforce connectivity.

Name (Reference)	**Description**
Kinematical connective constraint (Zhou and Li, 2008)	Chosen elements close to boundary of the unit cell are fixed as solid during inverse homogenization to serve as connectors.
Pseudo load (Zhou and Li, 2008)	Boundary conditions including a small (pseudo) load are added during inverse homogenization to promote connectivity where they are applied.
Unified formulation with nonlinear diffusion (Zhou and Li, 2008)	A nonlinear diffusion term is added to the objective function in order to penalize disconnect and checkerboard patterns. The extra term is added as an integral over all repeated unit cells instead of being applied to a single unit cell (as in the previous methods by the same author).
Functionally graded compatible unit cells (Radman et al., 2013)	An evolutionary optimization with a filter was used to successively create connecting functionally graded unit cells with similar topologies and smoothly varying properties.

Optimal tiling (Schumacher et al., 2015)	Previously synthesized microstructure families with overlapping properties are used to place an optimal candidate unit cell (or tile) in the design domain. As there are several candidates that approximate the target properties, an algorithm chooses a combination that increases performance and connectivity.
Full-scale optimization (Alexandersen and Lazarov, 2015)	Structural analysis and optimization is performed without separating the scales with homogenization, naturally promoting connectivity.
Interpolated microstructures (Cramer et al., 2016)	Microstructures optimized for a property (e.g. bulk modulus) at different solid fractions have their shape interpolated for other values, yielding a family of microstructures with smoothly varying geometry and properties.
Connective index (Du et al., 2018)	An index that measures if adjacent unit cells are connected is added as a constraint forcing interfacing cells to be compatible.
Compound formulation (Garner et al., 2019)	A concurrent multi-scale optimization is performed to optimize a property (e.g. maximize the bulk modulus) of individual unit cells and also of an extended (or compound) set of neighbouring unit cells to promote compatibility.
Spinodal interpolation (Senhora et al., 2022)	An interpolation function is used to enforce well-connected spinodal features. Spinodal architected materials naturally present geometric features that can be interpolated at the interface.

The accuracy of homogenization-based optimization frameworks is another problem that limits its performance. Separation of scales and periodicity are basic assumptions of homogenization theory that are not perfectly reproduced in practice since fabricated microstructures are not infinitely smaller than the macrostructure length scale, nor are they infinitely periodic. Wu et al. (2021) suggests to repeat a unit cell at least 5 to 10 times so the homogenized properties can be trusted. However, several frameworks represent each unit cell by a single finite element, so repeating cells may reduce the design freedom from aperiodic designs.

We finish this section addressing the topic of nonlinear multi-scale

topology optimization, for which a rather limited amount of work has been published so far. Though nonlinear homogenization has been used, it is often limited to inverse homogenization of singular unit cells (Wallin and Tortorelli, 2020). Experimental tests of optimized nonlinear microstructures seem to be limited to periodic designs and still present significant error (Behrou et al., 2021). A review on the topic (Xia and Breitkopf, 2017) also showed a computationally expensive implementation based on the multilevel finite element method that reportedly took approximately two weeks to optimize a cantilever beam mesh with 100×50 elements. Xia and Breitkopf (2017) also provided some discussion on implementing model reduction to expedite the high cost of nonlinear multi-scale topology optimization, though research on this topic is still limited.

2.4 Mechanical cloaking and shape matching

To cloak an object, from a physical perspective, means to hide its influence on a system with respect to a physical field. For instance, the introduction of a hole for a doorknob in a door will likely change the displacement, strain and stress fields on that door. One of the first ideas on mechanically hiding a hole was to introduce specific reinforced holes in a plane sheet that would not modify its stress distribution. These so-called "neutral holes" (Mansfield, 1956) are a particular form of a mechanical cloaking, that in the most general sense consist in designing a device around a hole that would remove its influence on the rest of the structure with respect to the displacement field compared to the structure without the hole.

This device or "cloak" may require a complex property distribution achievable with mechanical metamaterials. In 2006 two groups seemed to have simultaneously and independently published works on how to design "an invisibility device to guide light around an object as if nothing were there" (Leonhardt, 2006). Pendry et al. (2006) also suggested using metamaterials to redirect electromagnetic field to optically cloak an object as shown in Figure 2.6.

The mathematical technique developed for optical cloaking is based on coordinate transformation, the foundation of the field currently known as transformation optics. Coordinate transformation has been applied to many other physical fields other than optics, including but not limited to acoustics (Cummer et al., 2008), electric induction (Yang et al., 2012), heat conduction (Guenneau et al., 2012), matter waves (Zhang et al., 2008), and some even included tests with metamaterials (Farhat et al., 2008; Popa et al., 2011).

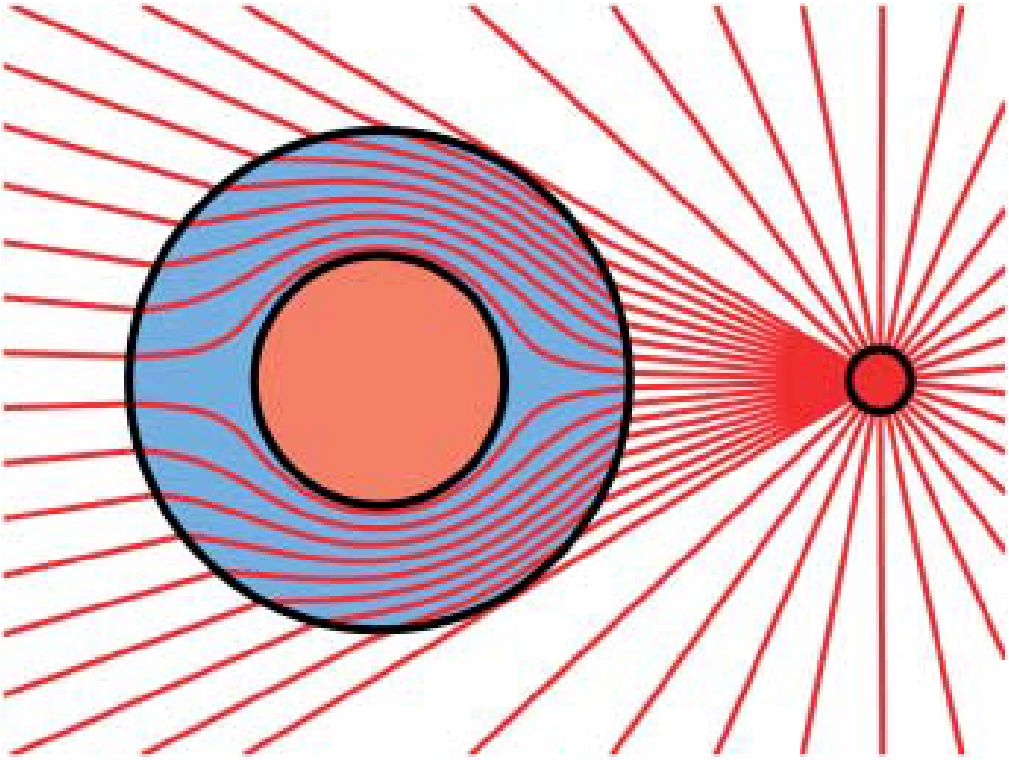

Figure 2.6: The electric displacement field generated by a point charge is distorted around a sphere, but leaves the highly anisotropic cloak region undisturbed (Pendry et al., 2006).

Mechanical cloaking of elastic waves is possible (Brun et al., 2009), though under very specific conditions such as the medium (thin plates) and at only certain frequencies.

The coordinate transformation technique requires the governing partial differential equation to be form invariant. Unfortunately, it has been proven that this does not hold for the general elastic problem (Milton et al., 2006; Norris and Shuvalov, 2011), as it would require the medium to be of a complex Cosserat material (Cosserat and Cosserat, 1909).

An elasto-mechanical "unfeelability cloak" was designed and fabricated using pentamode metamaterials (Bückmann et al., 2014). Bückmann et al. (2015) indirectly designed a mechanical cloak with coordinate transformation by first applying it to a well-known application (e.g. electrodynamics) and then re-interpreting the result as the dimensions of a lattice structure for an analogous mechanical problem. This method known as direct lattice transformation (DLT) is illustrated in Figure 2.7.

Due to the difficulties in applying the coordinate transformation technique to mechanical cloaking, topology optimization was proposed as a numerical approximation for designing a device with high cloaking performance. The first authors to propose this (Fachinotti et al., 2018) used a combination

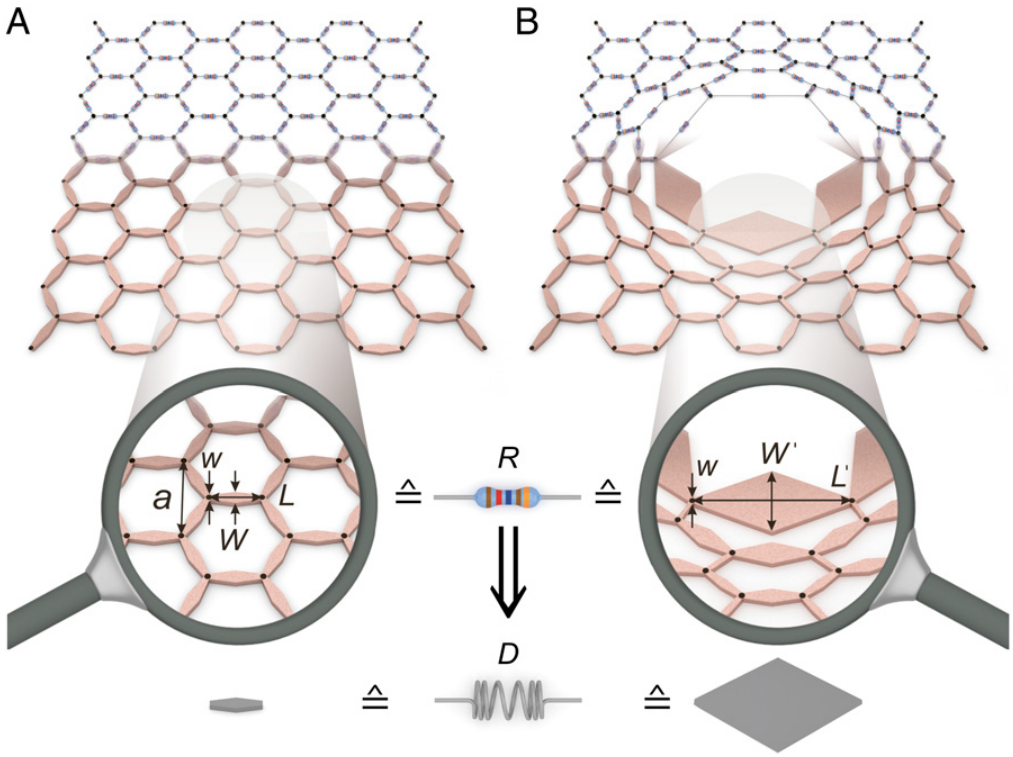

Figure 2.7: The hexagonal lattice in A is rearranged into a structure with an electrically cloaked hole. Swapping the resistors to equivalent Hooke springs with the same dimensions and analogous parameters yields a mechanically cloaked structure (Bückmann et al., 2014).

of two different materials in the cloak region, one with high stiffness and one with low stiffness compared to the reference material in the original structure without the hole . The discrete material optimization (DMO) (Stegmann and Lund, 2005) was implemented to choose the optimal material distribution in the cloak region. This work was later extended to the thermoelastic problem, which required solving a coupled PDE system for both the displacement and temperature fields (Álvarez Hostos et al., 2019).

Optimization has been used to optimize the stiffness parameters of a ground structure generated from a 2D lattice whose nodal positions were obtained using the DLT coordinate approach (Sanders et al., 2021a), as shown in Figure 2.8. A weighted least-squares objective function was suggested and multiple load cases were considered simultaneously, resulting in a structure with remarkable cloaking performance for uniaxial tension in multiple directions, outperforming the designs obtained using the original DLT approach.

The data-driven design has also been applied to the design of cellular metamaterials (Wang et al., 2020b), which consists in creating optimal topologies by placing aperiodic metamaterials with compatible boundaries as introduced in the previous section. A series of articles have been written in data-driven designs since then, like Chan et al. (2021), who found that reducing the

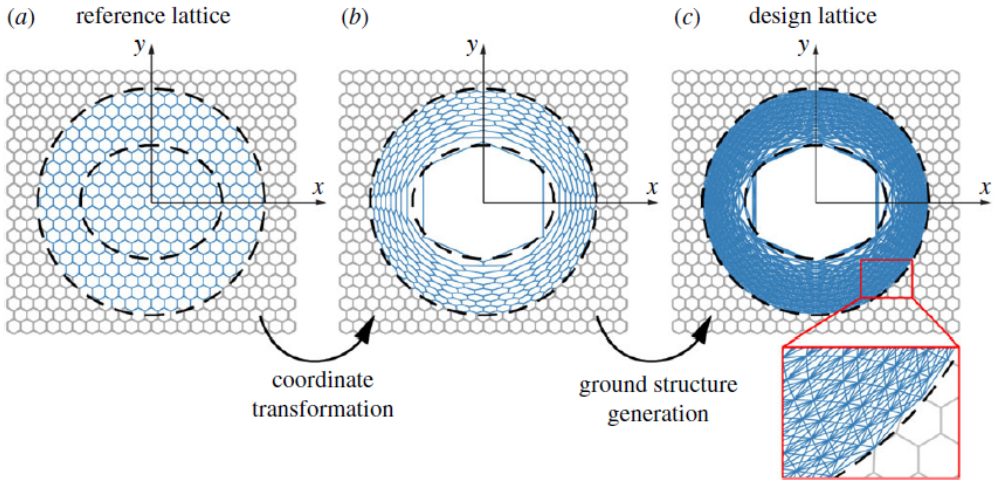

Figure 2.8: A 2D lattice in (a) is modified into (b) with coordinate transformation, and enriched into the ground structure in (c) that is used in the optimization of the mechanical cloak region (in blue) (Sanders et al., 2021a).

database to a smaller set of unit cells could save time when selecting optimal cells while improving structural performance. These data-driven frameworks are often tested with shape matching problems, as illustrated in Figure 2.9.

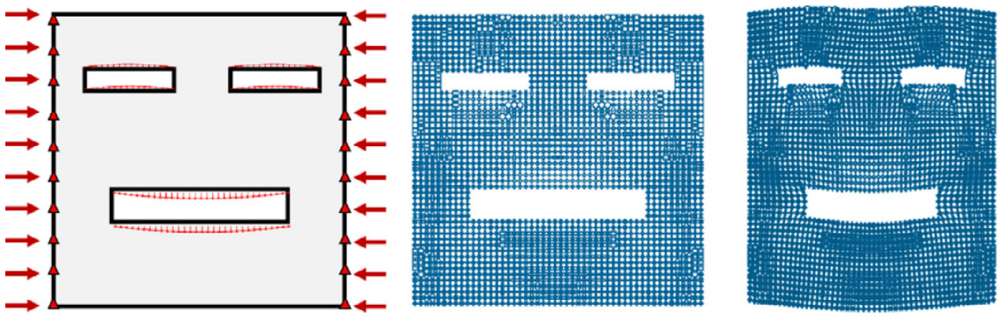

Figure 2.9: "Smiley face" shape matching problem (Wang et al., 2020a): problem definition (left); unloaded structure (middle); loaded structure (right).

The coordinate transformation method has been successfully used in the design of an elastostatic cloak, displaying remarkable cloaking performance in experimental tests (Xu et al., 2020). This was achieved with polar metamaterials, whose balance of angular momentum in a large body is maintained differently, effectively achieving asymmetric stress. Despite the interesting features of this approach, such as cloaking external loads of any arbitrary orientation, the physical principles behind it could potentially limit its performance[1]. We also note that the authors had to fabricate a complex four layered structure that could potentially limit this method to 2D applications in practice. For this

[1]The base materials in the microstructure are still subject to the conventional balance of angular momentum from Cauchy theory, thus curbing the scale in which this method is effective.

reason, works on mechanical cloaking include the ad-hoc design of metamaterials, like the top-down concurrent multiscale framework presented by (Lu and Tong, 2023), in which both scales are designed simultaneously during the optimization process.

A bottom-up approach by Senhora et al. (2022) implemented four biomimetic spinodal metamaterials to multi-scale topology optimization, where both unit cell rotation and density were considered. Figure 2.10 shows that connectivity was enforced by interpolating pixels, which ensured that the optimized design could be manufactured with masked stereolitography. These metamaterials inspired by naturally-occurring microstructures couple their spatially varying anisotropic properties with fabricable topology optimized multiscale structures.

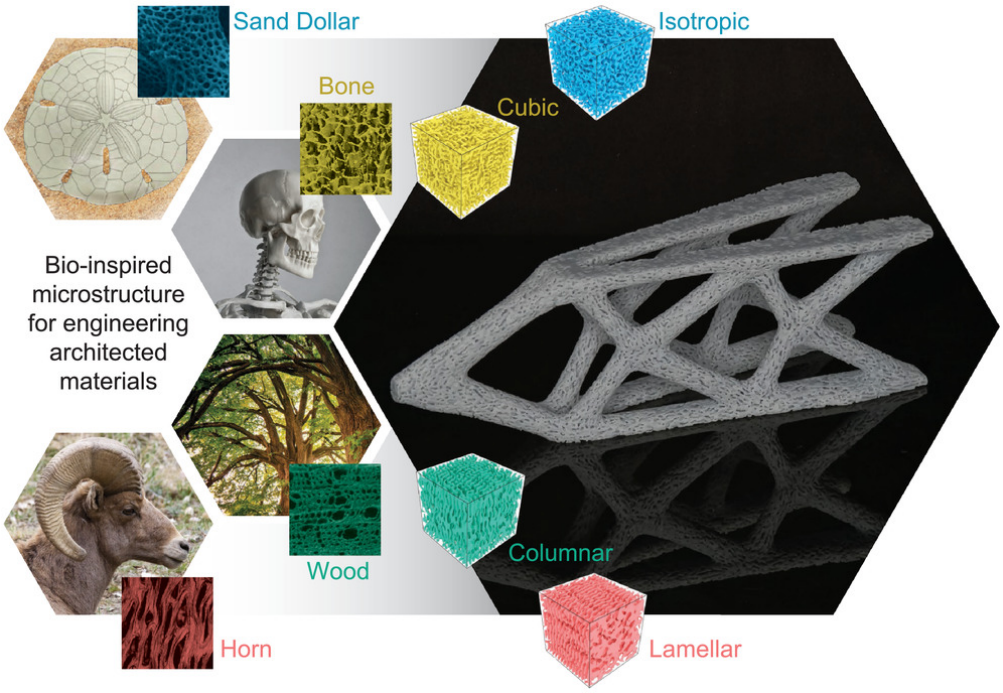

Figure 2.10: Biomimicry of mechanical recently used in the creation of spinodal architected materials (Senhora et al., 2022).

Data-driven approaches have also been presented as a valid alternative to target behavior problems: Chan et al. (2022) adapted a shape blending scheme to create smoothly graded microstructures applied to both compliance minimization and shape matching problems; Wang et al. (2022) designed and fabricated mechanically cloaked structures, and presented experimental results showing noticeable cloaking performance.

Recently, Cheng et al. (2023) proposed the the compatible boundary condition (CBC) paradigm for elastostatic cloaking, which requires the boundary conditions at the cloak-surrounding interface to match that of a reference in

order to recover the displacement field. Unlike traditional optimization-based cloaking, the CBC paradigm permits the cloaking device to be optimized apart from the rest of the structure, drastically reducing the number of degrees of freedom and allowing for a more efficient process. Furthermore, it provides insight on the root cause of the cloaking problem, by contrasting the discrepancy between the current design's and target force field on the interface. Cheng et al. (2023) implemented the CBC without a multiscale framework, generating efficient and well-connected structures. However, this may not scale well for larger problems, or when finer geometric details are required to achieve sufficient cloaking performance.

2.5 Static condensation and superelement method in topology optimization

In this last section, we review some of the TO works that leveraged some sort of condensation or model order reduction technique, as they relate to the strategy proposed in our work. It is possible to separate larger structures into substructures known as superelements, which have lower computational cost when interior or less-relevant degrees of freedom are condensed during finite element analysis. Superelements have long been employed in topology optimization, for example in weight minimization under static and eigenvalue loads (Patel, 1992) and in accelerating the optimization of vehicular panel substructures (Yang and Lu, 1996). These works leverage these techniques to accelerate the TO process, which can also be achieved utilizing reduced order models as done by Yoon (2010), Yano et al. (2021) and Kazakis and Lagaros (2022). Reduced-order modelling has also been used to efficiently design thermal cloaks (Sinigaglia et al., 2022).

The TO applications of static condensation and model reduction in general are not limited to increasing the computational efficiency of the optimization process, but they can also be utilized as a tool for multiscale analysis. Alternatives to the simulation and design of metamaterials without homogenization have been investigated for over a decade now (Czech, 2012), and condensation techniques seem to be a valid replacement for multiscale analysis outside the homogenization limits. For example, Qiu et al. (2009) optimized periodic unit cells for minimum compliance with the superelement method, and (Chung and Du, 2021) designed optimized multi-material celullar structures using a level-set method and Guyan reduction in the context of thermoelastic analysis.

In our work, we leverage static condensation equations to provide a mathematical foundation for the CBC paradigm to mechanical cloaking,

which can be further explored to design cloak devices that work for virtually any loading case, i.e., an unbiased cloak. Additionally, we discuss how the superelement method can be used to bridge the scales, permitting the a-posteriori design of unit cells' microstructures in a top-down approach.

3
Fundamentals of Multiscale Finite Element Analysis and Optimization

In this chapter, we provide a concise review of the fundamental concepts of homogenization-based multiscale finite element analysis. We begin with detailing the main concepts and equations in continuum mechanics, for both the kinematics and dynamics of deformable bodies. This is followed by the derivation of the finite element equations for linear elastostatic structural analysis. Then, we introduce the essential principles of homogenization theory as applied to the design of mechanical metamaterials, focusing on its application to multiscale topology optimization, which is the foundation for the multimaterial selection algorithm introduced in Chapter 5. Finally, some relevant aspects of numerical optimization are presented closing this chapter.

3.1
Continuum Mechanics Review

Although matter is formed by discrete parts at an atomic and molecular levels, common structures, e.g. a steel rod, typically seem to occupy all of the physical space comprised within its boundaries. The basis of continuum mechanics is accepting that, at the so-called macroscopic scale (or simply macro-scale), matter is continuous. For the sake of brevity, we will go over the main concepts needed for our multiscale TO application, so the reader is referred to the well established literature for further information (Mase et al., 1999; Holzapfel, 2002).

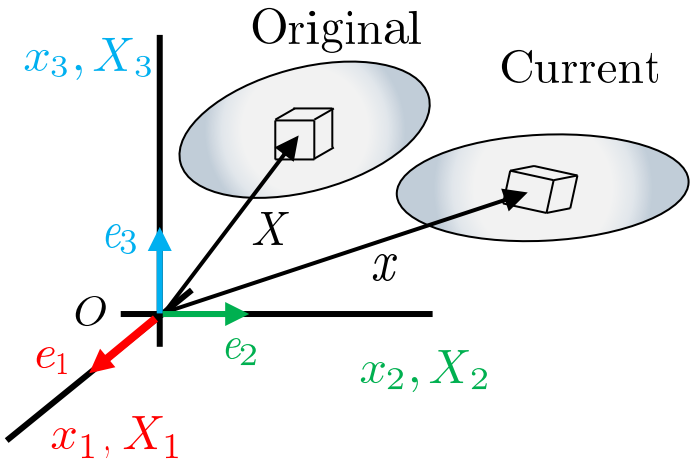

Figure 3.1: Body $\mathcal{B}$ in the original and deformed configurations.

Let us consider a body $\mathcal{B}$ shown in Figure 3.1 defined as a set of particles

(or material points) that occupy an initial position $\boldsymbol{X}$ of physical space at time $t = t_0$ denoted by:

$$\boldsymbol{X} = X_1\boldsymbol{e}_1 + X_2\boldsymbol{e}_2 + X_3\boldsymbol{e}_3 = X_i\boldsymbol{e}_i, \tag{3-1}$$

where X_i are the *material coordinates* of the particle and $\boldsymbol{e}_i$ are the basis vectors of geometric dimensions identified by the subscript $i = 1, 2, 3$. Hereafter, we adopt Einstein's convention, where repeated (or dummy) indices indicate summation. Let $\mathcal{B}$ undergo some deformation leading to a current configuration, such that a material point now occupies the current position with *spatial coordinates*

$$\boldsymbol{x} = x_1\boldsymbol{e}_1 + x_2\boldsymbol{e}_2 + x_3\boldsymbol{e}_3 = x_i\boldsymbol{e}_i. \tag{3-2}$$

For convenience, we store vectors as column vectors in the form

$$\boldsymbol{X} = \begin{bmatrix} X_1 & X_2 & X_3 \end{bmatrix}^T, \tag{3-3}$$

$$\boldsymbol{x} = \begin{bmatrix} x_1 & x_2 & x_3 \end{bmatrix}^T. \tag{3-4}$$

In what follows, we review the causes and effects of the motion of the deformation of a deformable body $\mathcal{B}$, that is, the kinematics and dynamics of deformation according to the continuum theory.

3.1.1 Kinematics of Deformation

We now seek to define a suitable metric for the local deformation of a body. Consider a vector $\Delta\boldsymbol{X} = \boldsymbol{X}_B - \boldsymbol{X}_A$ connecting two particles A and B at the original configuration. Taking the limit when $\Delta\boldsymbol{X} \to 0$, this vector can be thought of as a line $\mathrm{d}\boldsymbol{X}$ that changes into its infinitely-small spatial equivalent $\mathrm{d}\boldsymbol{x}$ in the current configuration. Since $\boldsymbol{x}$ is a function of $\boldsymbol{X}$, it follows that

$$\mathrm{d}\boldsymbol{x} = \boldsymbol{F} \cdot \mathrm{d}\boldsymbol{X}, \tag{3-5}$$

where the dot $(\cdot)$ is the contraction operator and $\boldsymbol{F}$ is the *deformation gradient* defined as

$$\boldsymbol{F} = \begin{bmatrix} \dfrac{\partial x_1}{\partial X_1} & \dfrac{\partial x_1}{\partial X_2} & \dfrac{\partial x_1}{\partial X_3} \\ \dfrac{\partial x_2}{\partial X_1} & \dfrac{\partial x_2}{\partial X_2} & \dfrac{\partial x_2}{\partial X_3} \\ \dfrac{\partial x_3}{\partial X_1} & \dfrac{\partial x_3}{\partial X_2} & \dfrac{\partial x_3}{\partial X_3} \end{bmatrix}. \tag{3-6}$$

The Euclidean norm (or 2-norm) of $\mathrm{d}\boldsymbol{x}$ measures how long the line connecting two neighboring points at the deformed configuration is. This quantity changes only upon deformation (i.e., it does not change with rigid-body motion). Substituting Equation (3-5) into the square of this norm yields

$$(\|\mathrm{d}\boldsymbol{x}\|_2)^2 = \mathrm{d}\boldsymbol{x}\cdot\mathrm{d}\boldsymbol{x} = (\boldsymbol{F}\cdot\mathrm{d}\boldsymbol{X})^T\cdot(\boldsymbol{F}\cdot\mathrm{d}\boldsymbol{X}) = \mathrm{d}\boldsymbol{X}^T\cdot\underbrace{\boldsymbol{F}^T\boldsymbol{F}}_{\boldsymbol{C}}\cdot\mathrm{d}\boldsymbol{X}, \tag{3-7}$$

where $\boldsymbol{C} = \boldsymbol{F}^T\boldsymbol{F}$ is the second-order *right Cauchy-Green deformation tensor*, a local metric of deformation that naturally arises from this derivation.

It can be shown from the polar decomposition theorem that $\boldsymbol{C}$ is a metric of pure stretch, i.e., it does not depend on rigid-body motion (Holzapfel, 2002). If we repeat the process shown in Equation (3-7) for the difference of the squares of the Euclidean norm between the current and original configurations, it yields

$$\|\mathrm{d}\boldsymbol{x}\|_2^2 - \|\mathrm{d}\boldsymbol{X}\|_2^2 = \mathrm{d}\boldsymbol{x}\cdot\mathrm{d}\boldsymbol{x} - \mathrm{d}\boldsymbol{X}\cdot\mathrm{d}\boldsymbol{X} = \mathrm{d}\boldsymbol{X}^T\cdot(\underbrace{\boldsymbol{C}-\boldsymbol{I}}_{2\boldsymbol{E}})\cdot\mathrm{d}\boldsymbol{X}, \tag{3-8}$$

giving raise to the Green-Lagrange strain tensor

$$\boldsymbol{E} = \frac{1}{2}(\boldsymbol{C}-\boldsymbol{I}), \tag{3-9}$$

where $\boldsymbol{I}$ is the second-order identity tensor. Unlike $\boldsymbol{C}$, $\boldsymbol{E}$ measures the relative change in deformation, as it vanishes for rigid-body motion (whereas $\boldsymbol{C}$ becomes $\boldsymbol{I}$).

Let us define the displacement vector

$$\boldsymbol{u} = \boldsymbol{x} - \boldsymbol{X}, \tag{3-10}$$

which permits us to rewrite Equation (3-9) as a function of displacement:

$$\boldsymbol{E} = \frac{1}{2}(\boldsymbol{\nabla}_0\boldsymbol{u} + (\boldsymbol{\nabla}_0\boldsymbol{u})^T + (\boldsymbol{\nabla}_0\boldsymbol{u})^T\boldsymbol{\nabla}_0\boldsymbol{u}), \tag{3-11}$$

where the material gradient operator $\boldsymbol{\nabla}_0$ denotes the gradient with respect to $\boldsymbol{X}$.

While the tensor $\boldsymbol{E}$ is suitable in the context finite strain, for sufficiently small displacements, we can neglect the quadratic terms in Equation (3-11), yielding the small deformation strain tensor

$$\boldsymbol{\varepsilon}(\boldsymbol{u}) = \frac{1}{2}(\boldsymbol{\nabla}_0\boldsymbol{u} + (\boldsymbol{\nabla}_0\boldsymbol{u})^T). \tag{3-12}$$

The tensor $\boldsymbol{\varepsilon}$ is a linear function of the displacements, and it greatly simplifies numerical implementation provided that deformations are small.

3.1.2 Dynamics of Deformation

Consider the body depicted in Figure 3.1 subject to an arbitrary loading condition that produces local deformation around an arbitrary point P. Let a small region in a cutting plane that passes through P with surface area ΔS

and normal vector $\boldsymbol{n}$, be subject to internal resultant force $\Delta \boldsymbol{f}$, as shown in Figure 3.2.

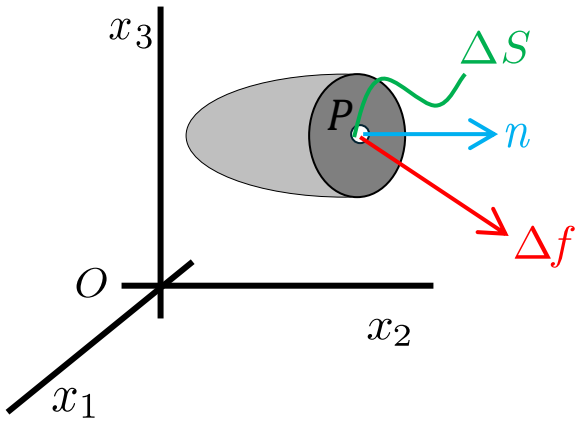

Figure 3.2: Section of body $\mathcal{B}$ from a cutting plane passing through point P.

The *Cauchy stress principle* establishes that we can represent the forces exerted on this region with normal vector $\boldsymbol{n}$ can be represented by a set of traction (or stress) vectors that take the form

$$\boldsymbol{t}^{(n)} = \lim_{\Delta S \to 0} \frac{\Delta \boldsymbol{f}}{\Delta S} = \frac{\mathrm{d}\boldsymbol{f}}{\mathrm{d}S}. \tag{3-13}$$

A complete description of the local forces takes the second-order Cauchy stress tensor $\boldsymbol{\sigma}$, such that the traction vector in one direction can be computed from the Cauchy stress formula:

$$\boldsymbol{t}^{(n)} = \boldsymbol{n} \cdot \boldsymbol{\sigma}. \tag{3-14}$$

If we assume that there are no concentrated moments, the conservation of angular momentum can be used to show that the Cauchy stress tensor is symmetric. In other words, it can be stored in matrix form as

$$\boldsymbol{\sigma} = \begin{bmatrix} \sigma_{11} & \sigma_{12} & \sigma_{13} \\ \sigma_{12} & \sigma_{22} & \sigma_{23} \\ \sigma_{13} & \sigma_{23} & \sigma_{33} \end{bmatrix} = \begin{bmatrix} \boldsymbol{t}^{(e_1)} & \boldsymbol{t}^{(e_2)} & \boldsymbol{t}^{(e_3)} \end{bmatrix}. \tag{3-15}$$

Applying the conservation of linear momentum, we can find the global form of the equations of motion as

$$\int_\Gamma \boldsymbol{t}^{(n)} \mathrm{d}\Gamma + \int_\Omega \rho\, \boldsymbol{b}\, \mathrm{d}\Omega = \frac{d}{dt} \int_\Omega \rho\, \boldsymbol{v}\, \mathrm{d}\Omega, \tag{3-16}$$

where Ω and $\Gamma = \partial\Omega$ are the domain and boundary of $\mathcal{B}$, respectively, and $\boldsymbol{b}$ is the body force per unit mass acting on $\mathcal{B}$. On the left-hand side of Equation (3-16) we have the summation of forces (surface traction and body forces) acting on the body, and on the right-hand side we have the time rate of change of its linear momentum.

It can be shown using the continuity equation and Euler's theorem that Equation (3-16) can be rewritten as

$$\int_{\Omega} (\boldsymbol{\nabla} \cdot \boldsymbol{\sigma} + \rho \boldsymbol{b} - \rho \dot{\boldsymbol{v}}) \, \mathrm{d}\Omega = \mathbf{0}, \tag{3-17}$$

where $\boldsymbol{\nabla} \cdot \boldsymbol{\sigma}$ is the divergent of the Cauchy stress with components $\sigma_{ij,j}$.

Since Equation Equation (3-17) is valid for any arbitrary volume in the body, the integrand must vanish, yielding the local form of the equations of motion:

$$\boldsymbol{\nabla} \cdot \boldsymbol{\sigma} + \rho \boldsymbol{b} = \rho \dot{\boldsymbol{v}}. \tag{3-18}$$

3.1.3 Constitutive Equation

A well-posed boundary value problem (BPV) in continuum mechanics requires the following elements: governing, constitutive and kinematic equations, and boundary conditions. The governing and kinematics equations used in this context are Equations (3-12) and (3-18). Here, we adopt a linear elastic constitutive equation between stress and strains in the form

$$\boldsymbol{\sigma} = \boldsymbol{\mathcal{C}} : \boldsymbol{\varepsilon}, \tag{3-19}$$

where $\boldsymbol{\mathcal{C}}$ is the elastic constitutive tensor, or simply elasticity tensor.

For computational implementation purposes, we store these tensors as vectors and matrices, denoted by square brackets, respectively, following the so-called Voigt convention. We rewrite Equation (3-19) in matrix form as

$$\underbrace{\begin{bmatrix} \sigma_{11} \\ \sigma_{22} \\ \sigma_{33} \\ \sigma_{12} \\ \sigma_{23} \\ \sigma_{31} \end{bmatrix}}_{\boldsymbol{\sigma}} = \underbrace{\begin{bmatrix} C_{11} & C_{12} & C_{13} & C_{14} & C_{15} & C_{16} \\ C_{12} & C_{22} & C_{23} & C_{24} & C_{25} & C_{26} \\ C_{13} & C_{32} & C_{33} & C_{34} & C_{35} & C_{36} \\ C_{14} & C_{42} & C_{43} & C_{44} & C_{45} & C_{46} \\ C_{15} & C_{52} & C_{53} & C_{54} & C_{55} & C_{56} \\ C_{16} & C_{62} & C_{63} & C_{64} & C_{65} & C_{66} \end{bmatrix}}_{\mathbf{C}} \underbrace{\begin{bmatrix} \varepsilon_{11} \\ \varepsilon_{22} \\ \varepsilon_{33} \\ \gamma_{12} \\ \gamma_{23} \\ \gamma_{31} \end{bmatrix}}_{\boldsymbol{\varepsilon}}, \tag{3-20}$$

where $\gamma_{ij} = 2\varepsilon ij$ (with $i \neq j$) are the shear strain components.

In this work, we consider thin two-dimensional plate-like structures, whose out-of-plane stresses (associated with direction 3) are negligible, that is, $\sigma_{13} = \sigma_{23} = \sigma_{33} = 0$. The constitutive equation for the plane stress condition takes the form

$$\underbrace{\begin{bmatrix} \sigma_{11} \\ \sigma_{22} \\ \sigma_{12} \end{bmatrix}}_{\boldsymbol{\sigma}} = \underbrace{\frac{E}{1-\nu^2} \begin{bmatrix} 1 & \nu & 0 \\ \nu & 1 & 0 \\ 0 & 0 & (1-\nu)/2 \end{bmatrix}}_{\mathbf{C}} \underbrace{\begin{bmatrix} \varepsilon_{11} \\ \varepsilon_{22} \\ \gamma_{12} \end{bmatrix}}_{\boldsymbol{\varepsilon}}, \tag{3-21}$$

where E is the Young modulus and ν is the Poisson's ratio

3.2 Finite Element Analysis

A continuum-based quasi-static structural analysis problem is typically cast as a boundary value problem whose analytical solution is often difficult or even impossible to obtain. Alternatively, we use the finite element method to find an approximate solution to the boundary value problem at discrete points of the domain, called nodes. This solution can then be interpolated to find the displacement field (and secondary variables like strain and stress) at any point of the domain.

While the finite element method was initially developed to analyze structural problems, is has been "employed extensively in the analysis of solids and structures and of heats and fluids" (Bathe, 2014). Nevertheless, in this section, we focus on the linear elastostatic application, whereas details of the homogenization-based implementation are discussed later in this chapter. For a more complete presentation of this topic, the reader is referred to the well-known literature, e.g. Hughes (2003); Zienkiewicz and Taylor (2005), among others.

3.2.1 Strong and Weak Forms of the Equilibrium Equations

Let us first clearly state the complete boundary-value problem for a deformable solid. Consider linear elastic structure subjected to quasi-static loads, which means that loads increase slowly enough to neglect the influence of transient effects, i.e., $\ddot{\boldsymbol{u}} = \dot{\boldsymbol{v}} = 0$. This domain Ω of the structure is enclosed by a boundary Γ partitioned into Γ_u and Γ_t where the Dirichlet (or essential) and Neumann (or natural) boundary conditions are applied. These partitions are complete ($\Gamma = \Gamma_u \cup \Gamma_t$) and disjoint ($\Gamma_u \cup \Gamma_t = \emptyset$) subsets of Γ.

The quasi-static equilibrium version of Equation 3-18 is cast as boundary value problem

$$\nabla \cdot \boldsymbol{\sigma} + \rho \boldsymbol{b} = \boldsymbol{0}, \quad \boldsymbol{x} \in \Omega \tag{3-22a}$$

$$\boldsymbol{u} = \overline{\boldsymbol{u}}, \quad \boldsymbol{x} \in \Gamma_u \tag{3-22b}$$

$$\boldsymbol{n} \cdot \boldsymbol{\sigma} = \overline{\boldsymbol{t}}, \quad \boldsymbol{x} \in \Gamma_t, \tag{3-22c}$$

where $\overline{\boldsymbol{u}}$ and $\overline{\boldsymbol{t}}$ are the imposed displacement and traction boundary conditions, respectively, and $\boldsymbol{n}$ is the outward unit vector normal to the boundary. This is known as the strong form because a solution must satisfy the differential

equation at every point of the domain. Additionally, the solution of this strong form must be sufficiently smooth, i.e., $u_i \in [C^2(\Omega)]$ (i.e., u and up to its second-order derivatives are continuous), such that all the derivatives are continuous.

We apply the principle of virtual work to derive the so-called weak form of this equation. The principle of virtual work states that the virtual work $\delta\Pi$ of external forces over virtual displacements $\delta\boldsymbol{u}_i$ is zero. The term virtual here refers to a small hypothetical variation of these quantities, denoted by the symbol δ.

The virtual work exerted on the entire body is computed by first multiplying Equation (3-22a) by $\delta\boldsymbol{u}_i$, and then integrating over the entire domain, which gives in component form

$$\delta\Pi = \int_\Omega \delta u_i \left(\sigma_{ji,j} + \rho b_i\right) \mathrm{d}\Omega = 0. \tag{3-23}$$

Next, we recall the symmetry of the Cauchy stress tensor, apply Gauss' divergence theorem and rearrange Equation (3-23) to reduce the differentiability requirements on the displacement field. It can be shown (Kim, 2014) that this process arrives at:

$$\int_\Omega \delta\varepsilon_{ij}\sigma_{ij}\mathrm{d}\Omega = \int_\Omega \delta u_i \rho b_i \mathrm{d}\Omega + \int_{\Gamma_u \cup \Gamma_t} \delta u_i \underbrace{\sigma_{ij} n_j}_{t_i} \mathrm{d}\Gamma, \tag{3-24}$$

where $\delta\boldsymbol{\varepsilon} = \varepsilon(\boldsymbol{\delta} u)$

Lastly, we substitute Equation (3-19) into Equation (3-24), and impose the requirement that $\delta\boldsymbol{u}$ vanishes on Γ_u to simplify the last integral. The weak form associated with Equation (3-22) is posed as follows:

Find $u \in \mathcal{V}$ and $v \in \mathcal{V}_0$ such that

$$\int_\Omega \boldsymbol{\varepsilon}(\delta\boldsymbol{u}) : \boldsymbol{\mathcal{C}} : \boldsymbol{\varepsilon}(\boldsymbol{u})\mathrm{d}\Omega = \int_\Omega \delta\boldsymbol{u} \cdot (\rho\boldsymbol{b})\, \mathrm{d}\Omega + \int_{\Gamma_t} \delta\boldsymbol{u} \cdot \boldsymbol{t}\, \mathrm{d}\Gamma, \tag{3-25}$$

where

$$\mathcal{V} = \left\{ \boldsymbol{u} \in \left[H^1(\Omega)\right]^3 \;\middle|\; \boldsymbol{u} = \overline{\boldsymbol{u}} \text{ on } \Gamma_u \right\}, \tag{3-26a}$$

$$\mathcal{V}_0 = \left\{ \delta\boldsymbol{u} \in \left[H^1(\Omega)\right]^3 \;\middle|\; \delta\boldsymbol{u} = \boldsymbol{0} \text{ on } \Gamma_u \right\}. \tag{3-26b}$$

The space of kinematically admissible displacements $\mathcal{V}$ enforces the essential boundary condition, and $\mathcal{V}_0$ is its virtual counterpart, both in three dimensions (denoted by the superscript 3 in the equations for the most general case, though we apply it for 2-dimensional problems later) . These form the trial and test spaces, respectively, in the context of the finite element method. Furthermore, the Sobolev space H^m contains functions whose weak derivatives up to order m are square-integrable. For $m = 1$, it guarantees that all integrals

in Equation (3-25) exist.

Equation (3-25) is referred to as the weak form since a solution does not need to satisfy the PDE at every point, but rather, it does so in an average or integral sense. There are two advantages to setting up the weak form: it lowers the differentiability requirement from second to first-order, and it sets the problem for numerical solutions via the finite element method. For a complete and rigorous derivation of these equations, the reader is referred to the aforementioned textbooks and references therein, e.g. (Oden, 2006).

3.2.2 Finite element discretization and isoparametric mapping

The finite element method approximates the solution of the weak form by first discretizing the original domain Ω into a suitable mesh of finite elements, as illustrated in Figures 3.3 and 3.3a. The discretized domain $\hat{\Omega}$ and its boundary approximate the original ones and are partitioned into complete, disjoint subsets $\Omega^{(e)}0$ (see Figure 3.3c for a typical triangular element), such that:

$$\Omega \approx \hat{\Omega} = \Omega^{(1)} \cup \Omega^{(2)} \cup \cdots \cup \Omega^{(N_e)}, \tag{3-27}$$

where N_e is the total number of elements in the mesh.

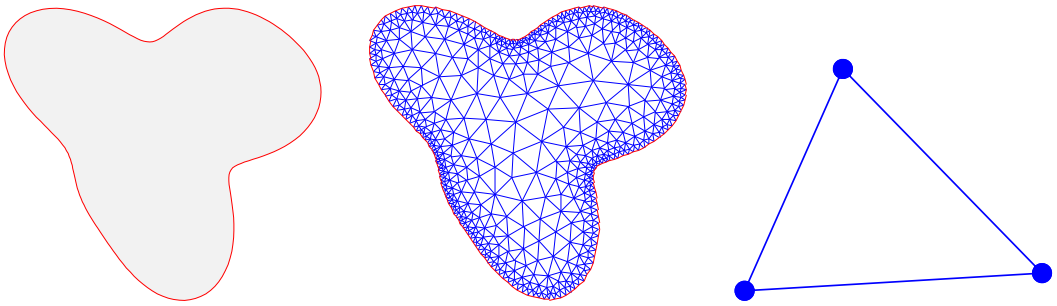

(a) Original domain: Ω. (b) Discretized domain: $\hat{\Omega}$ (c) Element domain: $\Omega^{(e)}$

Figure 3.3: Finite element discretization into trigular elements.

Let $\boldsymbol{x}_n^{(e)}$ be the initial position n-th node of the e-th element in the mesh, and $\boldsymbol{u}_n^{(e)}$ be its displacement at the end of a quasi-static loading. We define the former in the mesh generation, whereas the latter is computed in the finite element analysis. We employ an isoparametric formulation to interpolate the position and displacement at any point within $\Omega^{(e)}$:

$$\mathbf{x}(\boldsymbol{\xi}) = \sum_k N_k^{(e)}(\boldsymbol{\xi}) \mathbf{x}_k^{(e)}, \tag{3-28a}$$

$$\mathbf{u}(\boldsymbol{\xi}) = \sum_k N_k^{(e)}(\boldsymbol{\xi}) \mathbf{u}_k^{(e)}, \tag{3-28b}$$

where the summation is over all of the nodes of the element, and N_k are the shape function that depend on the coordinates $\boldsymbol{\xi}$. Additionally, we use upright (non-italic) bold symbols to denote tensors in their matrix form.

In this work, we use 4-node quadrilaterals (Q4) elements for which $\boldsymbol{\xi} = \begin{Bmatrix} \xi & \eta \end{Bmatrix}^T$ and $-1 \leq \xi, \eta \leq +1$. The shape functions N_1 to N_4 uniquely map each point from a natural (or parent) coordinate system with coordinates $\boldsymbol{\xi}$ onto the global system with cartesian coordinates $\mathbf{x} = \begin{Bmatrix} x & y \end{Bmatrix}^T$ as shown in Figure 3.4. By convention, we number the corners of the element (called nodes in this context) in counter-clockwise order.

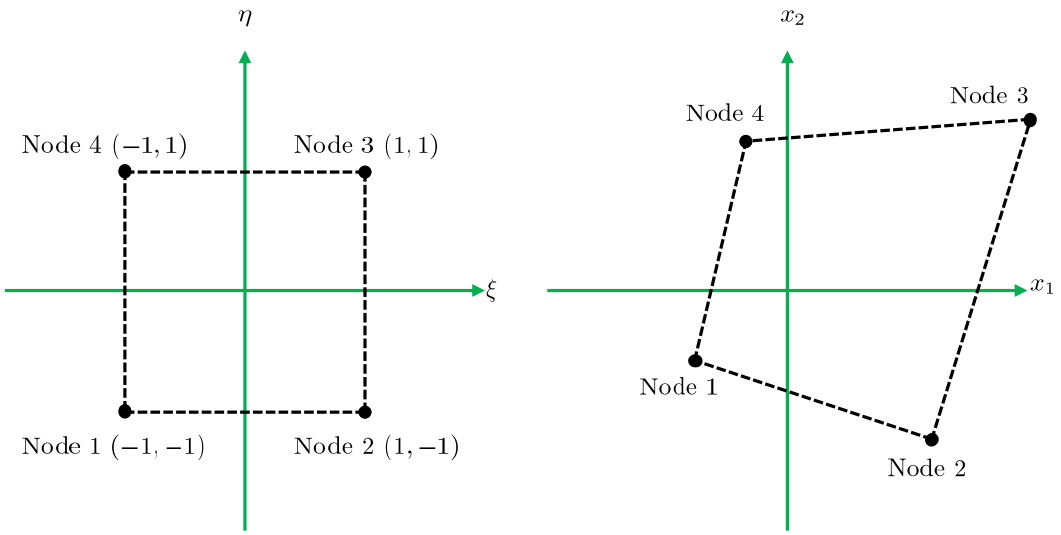

(a) Reference element in the natural system. (b) Physical element in the global system

Figure 3.4: Quadrilateral element in the natural and global system.

The shape functions must satisfy conditions such as partition of unity and completeness that are not discussed in depth in this text, for brevity. For the Q4 element, we store the functions in the following matrix form:

$$\mathbf{N}^{(e)}(\xi,\eta) = \begin{Bmatrix} N_1^{(e)}(\xi,\eta) \\ N_2^{(e)}(\xi,\eta) \\ N_3^{(e)}(\xi,\eta) \\ N_4^{(e)}(\xi,\eta) \end{Bmatrix} = \begin{Bmatrix} \frac{1}{4}(1-\xi)(1-\eta) \\ \frac{1}{4}(1+\xi)(1-\eta) \\ \frac{1}{4}(1+\xi)(1+\eta) \\ \frac{1}{4}(1-\xi)(1+\eta) \end{Bmatrix}. \tag{3-29}$$

3.2.3 Strain-displacement equations

The first-order derivatives of the displacement required in the weak form come by deriving Equation (3-28b) with respect to x_i, which gives

$$\frac{\partial \mathbf{u}}{\partial x_i} = \sum_k \frac{\partial N_k^{(e)}}{\partial x_i} \mathbf{u}_k^{(e)}. \tag{3-30}$$

The derivatives of the shape function are computed with the chain rule. For implementation purposes, we compute the derivatives of the shape function by solving the following linear system that comes from the chain rule:

$$\underbrace{\begin{Bmatrix} \dfrac{\partial N_k^{(e)}}{\partial \xi} \\ \dfrac{\partial N_k^{(e)}}{\partial \eta} \end{Bmatrix}}_{\dfrac{\partial N_k^{(e)}}{\partial \boldsymbol{\xi}}} = \underbrace{\begin{bmatrix} \dfrac{\partial x_1}{\partial \xi} & \dfrac{\partial x_2}{\partial \xi} \\ \dfrac{\partial x_1}{\partial \eta} & \dfrac{\partial x_2}{\partial \eta} \end{bmatrix}}_{\mathbf{J}} \underbrace{\begin{Bmatrix} \dfrac{\partial N_k^{(e)}}{\partial x_1} \\ \dfrac{\partial N_k^{(e)}}{\partial y_2} \end{Bmatrix}}_{\dfrac{\partial N_k^{(e)}}{\partial \mathbf{x}}}, \tag{3-31}$$

where $\mathbf{J}$ is the Jacobian of the transformation from $\boldsymbol{\xi}$ to $\boldsymbol{x}$, whose components are computed by taking the derivatives of Equation (3-29) with respect to the natural coordinates. Once all terms $\partial N_k^{(e)}/\partial \boldsymbol{x}$ are computed, we can substitute them back into Equation (3-30).

Substituting Equation (3-30) into the gradients of Equation (3-12) provides an expression where the strain at any point is obtained from the the nodal displacements and derivatives of the shape functions, which can be represented in matrix form as

$$\boldsymbol{\varepsilon}(\boldsymbol{u}) = \begin{Bmatrix} \varepsilon_{11} \\ \varepsilon_{22} \\ \gamma_{12} \end{Bmatrix} = \sum_k \underbrace{\begin{bmatrix} \dfrac{\partial N_k^{(e)}}{\partial x_1} & 0 \\ 0 & \dfrac{\partial N_k^{(e)}}{\partial x_1} \\ \dfrac{\partial N_k^{(e)}}{\partial x_2} & \dfrac{\partial N_k^{(e)}}{\partial x_1} \end{bmatrix}}_{\mathbf{B}_k^{(e)}} \underbrace{\begin{Bmatrix} u_1 \\ u_2 \end{Bmatrix}_k}_{\mathbf{u}_k}, \tag{3-32}$$

where $\mathbf{B}_k$ is the strain-displacement matrix, and the strain is computed at a point within the domain of element e.

3.2.4 Galerkin Method

The derivation of finite element method equations consist in assuming a trial and test solutions, which are the finite-element counterparts to $\boldsymbol{u}$ and $\delta\boldsymbol{u}$ in Equation (3-25), respectively. In Galerkin-based formulation, we adopt the same approximation for the trial and test, which can be written from Equation (3-28b) in matrix form as

$$\mathbf{u} = \mathbf{N}\mathbf{u}, \tag{3-33a}$$

$$\delta\mathbf{u} = \mathbf{N}\,\delta\mathbf{u}, \tag{3-33b}$$

where $\mathbf{N}$ is a matrix whose columns contain vectors of shape functions like as in Equation (3-29), and $\mathbf{u}$ is a column vector containing all nodal displacements in an order consistent with $\mathbf{N}$. The derivation in this subsection considers the global matrices (e.g. $\mathbf{N}$), as opposed to their element-level counterparts (e.g. $\mathbf{N}^{(e)}$).

Likewise, for the strain and virtual strain, we have

$$\boldsymbol{\varepsilon} = \mathbf{B}\mathbf{u}, \tag{3-34a}$$

$$\delta\boldsymbol{\varepsilon} = \mathbf{B}\,\delta\mathbf{u}, \tag{3-34b}$$

where $\mathbf{B}$ is the strain-displacement counterpart of $\mathbf{N}$.

Substituting Equations (3-33) and (3-34) into Equation (3-25) in matrix form gives

$$\int_\Omega (\mathbf{B}\,\delta\mathbf{u})^T \mathbf{C}\,(\mathbf{B}\mathbf{u})\,\mathrm{d}\Omega = \int_\Omega (\mathbf{N}\delta\mathbf{u})^T \mathbf{b}\,\mathrm{d}\Omega + \int_{\Gamma_t} (\mathbf{N}\delta\mathbf{u})^T \mathbf{t}\,\mathrm{d}\Gamma. \tag{3-35}$$

where the left-hand side is known as the energy bilinear form and the right-hand side is the load form.

We manipulate Equation (3-33) by removing the constant nodal displacement vector $\mathbf{u}$ from the integral, and factorizing the virtual displacement, yielding

$$\delta\mathbf{u}^T \left[\left(\int_\Omega \mathbf{B}^T \mathbf{C}\,\mathbf{B}\,\mathrm{d}\Omega \right) \mathbf{u} - \int_\Omega \mathbf{N}^T \mathbf{b}\,\mathrm{d}\Omega - \int_{\Gamma_t} \mathbf{N}^T \mathbf{t}\,\mathrm{d}\Gamma \right] = 0. \tag{3-36}$$

Notice that Equation (3-36) must hold for any nonempty subset of Ω and admissible test function $\delta\mathbf{u}$. Therefore, the content of the square bracket must vanish, that is:

$$\underbrace{\left(\int_\Omega \mathbf{B}^T \mathbf{C}\,\mathbf{B}\,\mathrm{d}\Omega \right)}_{\mathbf{K}} \mathbf{u} - \underbrace{\int_\Omega \mathbf{N}^T \mathbf{b}\,\mathrm{d}\Omega}_{\mathbf{f}^b} - \underbrace{\int_{\Gamma_t} \mathbf{N}^T \mathbf{t}\,\mathrm{d}\Gamma}_{\mathbf{f}^s} = \mathbf{0}, \tag{3-37}$$

where $\mathbf{K}$ is the stiffness matrix, and $\mathbf{f}^b$ and $\mathbf{f}^s$ are the body force and surface traction vectors, respectively, in the global scope.

3.2.5 Computational Implementational

We cast Equation (3-37) as a linear system in the form

$$\mathbf{f} = \mathbf{K}\mathbf{u}, \tag{3-38}$$

where $\mathbf{f} = \mathbf{f}^b + \mathbf{f}^s$ is the force vector. In this work, we neglect body forces, so $\mathbf{f} = \mathbf{f}^s$.

While the system in Equation (3-38) involves global quantities — those

defined over the entire domain — in practice, each matrix is computed at the element (or local) level and then assembled into the global system. Introducing the partition from Equation (3-27) into the finite element matrices defined in Equation (3-37), allows us to write the contribution of each element as:

$$\mathbf{f}^{(e)} = \int_{\Omega^{(e)}} \left(\mathbf{N}^{(e)}\right)^T \mathbf{b}\, \mathrm{d}\Omega + \int_{\Gamma_t^{(e)}} \left(\mathbf{N}^{(e)}\right)^T \mathbf{t}\, \mathrm{d}\Gamma, \tag{3-39a}$$

$$\mathbf{K}^{(e)} = \int_{\Omega^{(e)}} \left(\mathbf{B}^{(e)}\right)^T \mathbf{C}^{(e)}\, \mathbf{B}^{(e)}\, \mathrm{d}\Omega, \tag{3-39b}$$

where $\Gamma_t^{(e)}$ is the element boundary subject to traction exerted on Γ_t. For the plane stress condition, the tensors are stored in Voigt notation, as defined in Equation (3-21). Additionally, the differential elements become $\mathrm{d}\Omega = t\mathrm{d}A$ and $\mathrm{d}\Gamma = t\mathrm{d}S$, where t is the thickness of, and $\mathrm{d}A$ and $\mathrm{d}S$ denote the area element of the mid-plane and the corresponding boundary line element, respectively, reflecting the reduction of the problem to two dimensions.

The integrals in Equations (3-39a) and (3-39b) are often computed with numerical integration methods such as Guass-Legendre quadrature. For details on this numerical method, the reader is referred to Zienkiewicz et al. (2005) and references therein. Additionally, we neglect the influences of body forces in this work, so the first term of the right-hand side of Equation (3-39a) vanishes.

By means of a Boolean scatter matrix $\mathbf{L}^{(e)}$ that maps the local degrees of freedom (DOFs) onto the global system, we write the assembly process as the following linear combination:

$$\mathbf{f} = \sum_e \mathbf{L}^{(e)} \mathbf{f}^{(e)}. \tag{3-40a}$$

$$\mathbf{K} = \sum_e \left(\mathbf{L}^{(e)}\right)^T \mathbf{K}^{(e)} \mathbf{L}^{(e)}, \tag{3-40b}$$

The boundary conditions are imposed by modifying the matrices $\mathbf{K}$ and $\mathbf{f}$ in Equation (3-38) as follows:

Essential boundary conditions take the form $u_i = \overline{u}_i$, where $\overline{u}_i$ is a prescribed displacement. They are enforced by setting all components in the i-th row of $\mathbf{K}$ to zero, except for the diagonal entry K_{ii} [1] , which is set to one. Additionally, the right-hand side component f_i is set to $\overline{u}_i$, ensuring that the condition is satisfied upon solving the system.

Natural boundary conditions arising from surface tractions are already accounted for in Equation (3-39a). Point loads, on the other hand, can

[1] Here, repetition does not imply summation.

be applied directly by setting $f_i = \overline{f}_i$, where i is the degree of freedom at which the load is applied.

We leverage the symmetry and sparsity of the stiffness matrix by partitioning the modified system into fixed and free DOFs in the form:

$$\begin{Bmatrix} \mathbf{f}_{\text{free}} \\ \mathbf{f}_{\text{fixed}} \end{Bmatrix} = \begin{bmatrix} \mathbf{K}_{\text{free,free}} & \mathbf{K}_{\text{free,fixed}} \\ \mathbf{K}_{\text{fixed,free}} & \mathbf{K}_{\text{fixed,fixed}} \end{bmatrix} \begin{Bmatrix} \mathbf{u}_{\text{free}} \\ \mathbf{u}_{\text{fixed}} \end{Bmatrix} \tag{3-41}$$

Solving the first line of Equation (3-41) for the known term yields

$$\mathbf{K}_{\text{free,free}}\mathbf{u}_{\text{free}} = \mathbf{f}_{\text{free}} - \mathbf{K}_{\text{free,fixed}}\overline{\mathbf{u}}_{\text{fixed}}. \tag{3-42}$$

Equation (3-41) is ill-posed since $\mathbf{K}$ is singular prior to applying the essential boundary conditions, which we do by manipulating Equation (3-41) into:

$$\begin{bmatrix} \mathbf{K}_{\text{free,free}} & \mathbf{0} \\ \mathbf{0} & \mathbf{I} \end{bmatrix} \begin{Bmatrix} \mathbf{u}_{\text{free}} \\ \mathbf{u}_{\text{fixed}} \end{Bmatrix} = \begin{Bmatrix} \mathbf{f}_{\text{free}} - \mathbf{K}_{\text{free,fixed}}\mathbf{u}_{\text{fixed}} \\ \overline{\mathbf{u}} \end{Bmatrix}, \tag{3-43}$$

wehere $\mathbf{I}$ is the identity matrix, and $\overline{\mathbf{u}}$ is the vector with the prescribed degrees of freedom. Since the system in Equation (3-43) is well-posed and symmetric, we solve it with efficient algorithms like the Cholesky decomposition.

3.3 Homogenization Theory for Multiscale Modeling

Homogenization is a concept typically associated with the study of composites within the well-established field of micromechanics. Composites are materials composed of two or more constituents, whose individual properties and geometries influence affect the behavior of the whole structure. Multiscale composites are materials whose constituents can be at different length scales. Table 3.1 presents a common, though not exhaustive, list of these scales, their typical features, and typical size ranges.

Table 3.1: Hierarchy of material scales in composites, adapted from Bednarcyk and Arnold (2012).

Scale	**Typical Features**	**Size Range**
Microscale	Fiber, interphase, and matrix	From hundreds of nanometers up to a few micrometers
Mesoscale	Tow, ply, and laminate	From micrometers to millimeters
Macroscale	Parts formed by assembly of many mesoscale elements	Millimeters and larger

In order to perform structural analysis of structures with composites, one traverses to lower-level scales via localization techniques, and to higher-level

scales with homogenization. In this sense, homogenization can be defined as a technique that provides the physical response of a structure at given scale based on the response at a lower scale. Localization is the opposite, traversing from higher to lower scale.

Multiscale modeling methods can be categorized into hierarchical, synergistic, or concurrent (Sullivan and Arnold, 2011). While the synergistic and concurrent methods consider coupled scales via homogenization and localization techniques, hierarchical methods consider a one-way coupling of the scales (homogenization or localization) in the form of boundary conditions or effective properties.

While homogenization was originally intended to estimate effective properties of composites with microscopic (and lower) geometric features, as discussed in Chapter 2, though the range of length scales of parts produced by additive manufacturing may not fall within the limits of homogenization theory, many authors still use it as an efficient method for multiscale analysis.

In this work, we focus on a hierarchical approach based on the homogenization of effective properties, namely, the elasticity tensor, which is a common practice in multiscale topology optimization (Wu et al., 2021). Aboudi et al. (2012) among other textbooks presents several multiscale modeling methods in greater detail for the interested reader.

3.3.1 Effective Elasticity Tensor

We present in what follows an expression to compute the effective (or homogenized) elasticity tensor of a material with constituents with different properties. Let

$$\overline{\sigma}_{ij} = \frac{1}{V}\int_V \sigma_{ij}\,\mathrm{d}V, \quad \text{and} \tag{3-44a}$$

$$\overline{\varepsilon}_{ij} = \frac{1}{V}\int_V \varepsilon_{ij}\,\mathrm{d}V \tag{3-44b}$$

be the components of stress and strains of the material averaged over its volume V. While the quantities in the microscopic (or near) field may vary across the domain, the average macroscopic values denoted by the bar ($\overline{\sigma}_{ij}$ and $\overline{\varepsilon}_{ij}$) are considered constant for a given point in the macroscopic (or far) field. Notice that this definition requires the assumption of *scale separation*, that is, physical fields at a macroscopic material point are function of the microscopic response at a theoretically infinitely smaller level that when averaged yields the macroscopic counterpart.

While the elastic modulus may vary across the domain of the microstruc-

ture, one can define an effective or homogenized elasticity tensor $\boldsymbol{\mathcal{C}}^H$ that correlates the volume-averaged stresses and strains, that is,

$$\overline{\sigma}_{ij} = \mathcal{C}^H_{ijkl}\,\overline{\varepsilon}_{kl}. \tag{3-45}$$

If we apply a homogeneous periodic displacement boundary condition to the infinitely periodic microstructure, we can use the average strain theorem to show that

$$\mathcal{C}^H_{ijkl} = \int_V \mathcal{C}_{ijpq}\,\varepsilon^{(kl)}_{pq}\,\mathrm{d}V. \tag{3-46}$$

where the index (kl) denotes when the case when a unit strain $\varepsilon^{(kl)} = 1$ is induced. Again, we explicitly adopt the assumption of *infinite periodicity* by assuming periodic boundary conditions. Further information on derivation of Equation (3-46) is available in the literature (Aboudi et al., 2012; Torquato and Haslach Jr, 2002), and is outside the scope of this work.

3.3.2 Numerical Homogenization

In this work, we utilize the numerical implementation of a 2D homogenization code provided by Andreassen and Andreasen (2014). In what follows, we briefly introduce practical implementation details relevant to our work, so the interested reader is referred to the original paper and references therein for additional information.

Our purpose is to determine the homogenized stiffness tensor of a microstructure with different constituents. We define each constituent's material properties in the form

$$\lambda = \frac{\nu E}{(1+\nu)(1-2\nu)} \tag{3-47a}$$

$$\mu = \frac{E}{2(1+\nu)}, \tag{3-47b}$$

where λ and μ are the first and second Lamé parameters, respectively. The original implementation was developed for the plane strain condition, so we modify the first Lamé parameter into

$$\hat{\lambda} = \frac{2\mu\lambda}{\lambda + 2\mu}, \tag{3-48}$$

which is its plane stress counterpart, as detailed by Andreassen and Andreasen (2014).

Next, we define a microstructure with well-defined geometric features formed by a isotropic homogeneous constituent shown in black in Figure 3.5a for a truss-like microstructure. The microstructure is then discretized into a

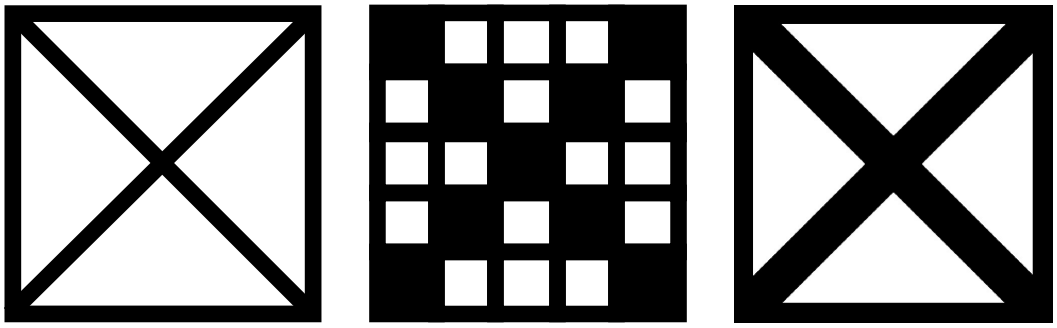

(a) Microstructure geometry. (b) Coarse discretization. (c) Fine discretization ($\rho = 0.3$).

Figure 3.5: Geometry of a truss-like microstructure and its coarse finite element discretization.

finite element mesh, which is analyzed several times with periodic boundary condition for each unit strain case used in Equation (3-46), where the homogenized elasticity tensor is computed. The microstructure is discretized into a Q4 mesh, where the empty regions formed by void (white) elements have their Young modulus set to a small value in the finite element analysis. Notice that a coarse discretization like the one in Figure 3.5b cannot fully realize the geometric details, illustrating the importance of a sufficiently refined mesh in this process.

In this work, we discretize the original 1-mm-square domain into 400×400 unit-thickness Q4 elements, under plane stress. An arbitrary material with $E = 1$ GPa and $\nu = 0.3$ yields the following homogenized elasticity tensor in matrix form:

$$\mathbf{C}^H = \begin{bmatrix} 1.0989 & 0.3297 & 0.0000 \\ 0.3297 & 1.0989 & 0.0000 \\ 0.0000 & 0.0000 & 0.3846 \end{bmatrix} \text{GPa}, \tag{3-49}$$

when the density (ratio of solid elements in the microstructure) is $\rho = 0.3$ as shown in Figure 3.5c. To determine the effective homogenized properties associated with the elasticity tensor in Equation (3-49), we first compute the matrix of the compliance tensor as

$$\mathbf{S}^H = (\mathbf{C}^H)^{-1} = \begin{bmatrix} S_{11} & S_{12} & S_{13} \\ S_{21} & S_{22} & S_{23} \\ S_{31} & S_{32} & S_{33} \end{bmatrix}. \tag{3-50}$$

Then, the equivalent elastic engineering properties for the homogenized tensor can be determined from the expressions (Aboudi et al., 2021): $E = 1/S_{11} = 0.1007$ GPa and $\nu = -E\,S_{12} = 0.4267$. This illustrates how an architected material can yield widely different properties from its homogeneous constituents, which greatly enhances the design space in topology optimization,

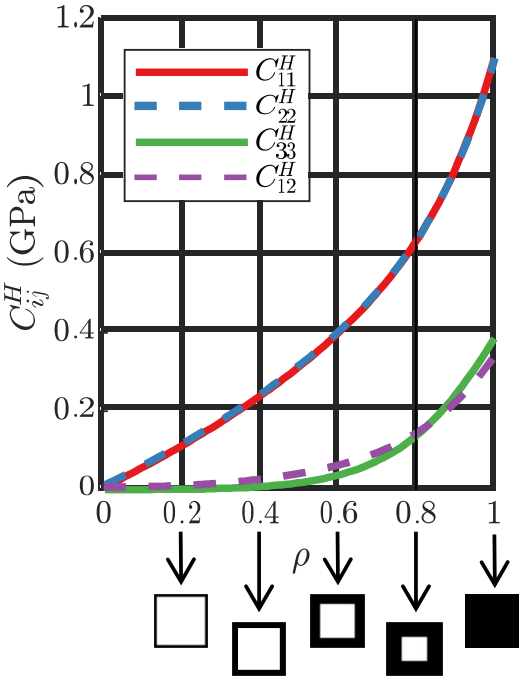

Figure 3.6: Elasticity tensor components as a function of the density of square-holed unit cells.

which is a desirable feature specially in the context of mechanical cloaking.

3.3.3 Property Interpolation of Families of Microstructures

We implement the homogenized stiffness tensor into our finite element framework by introducing it into the computation of the stiffness matrix in Equation (3-39b). The original homogenization-based TO approach that inspired this work requires "a functional relationship between the density of material in the composite (i.e. sizes of holes) and the effective material properties" (Bendsøe and Kikuchi, 1988). This "functional relationship" is derived from a set (or family) of microstructures uniquely associated with a density parameter $\rho \in [0, 1]$ that the topology (and therefore the homogenized material parameters) is a monotonic and continuously varying function of ρ. In this work, we refer to a given microstructure as a repeating unit cell, which, if it is periodically distributed in the domain.

To illustrate this concept, consider the family of unit cells with centered square holes. Figure 3.6 shows the variation of the components of the homogenized plane stresselasticity tensor in matrix form, C_{ij}^H. Notice that, despite the relatively simple design, none of the curves are linear. It is important, therefore, to design suitable families of microstructures whose properties vary smoothly with ρ. Furthermore, enforcing these functions to be monotonic is desirable from the point of view of the optimization process, as non-monotonic

functions may lead to sub-optimal local minima While not a strict requirement, we required functions $C_{ij}^H(\rho)$ to be strictly monotonic for the design space adopted in the examples shown in this work.

In order to create an analytical functional relationship between the material parameters and the density, we selected a high-order polynomial interpolation to derive the functions $C_{ij}^H(\rho)$. The polynomial curve with order N_{fit} for the elasticity tensor takes the form:

$$C_{ij}^H(\rho) = \sum_{n=0}^{N_{\text{fit}}} c_{ij,n}\rho^n, \tag{3-51}$$

where c_n is the n-th fitted coefficient.

In our tests, we chose 9th-order polynomials were accurate and accrued no significant overhead to the finite element analysis algorithm during optimization compared to lower-order interpolations. While lower-order polynomials can fit most $C_{ij}^H(\rho)$ curves, some required higher-order to ensure both high accuracy and monotonic behavior. The interpolated function and its derivatives are shown in Figure 3.7, where it can be seen that the the functions are monotonic since $\mathrm{d}C_{ij}^H(\rho)/\mathrm{d}\rho > 0$ for the ρ intervals used in the optimization framework.

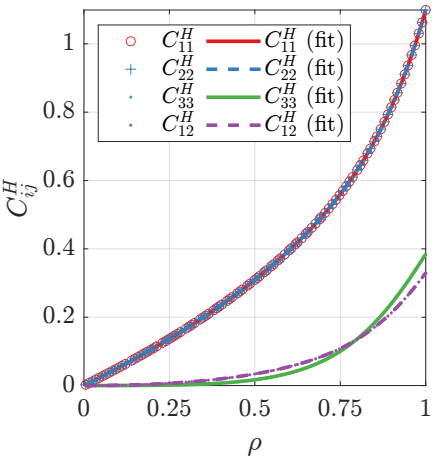

(a) Interpolated function $C_{ij}^H(\rho)$.

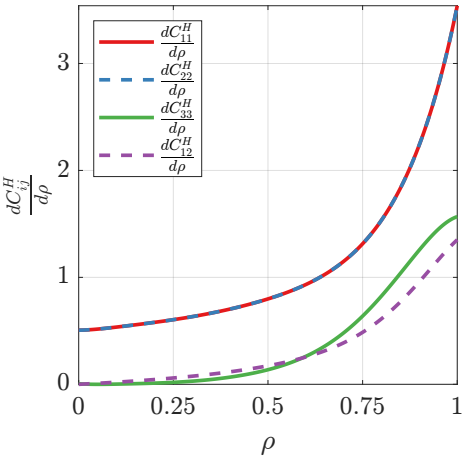

(b) Derivative of the interpolation $\mathrm{d}C_{ij}^H(\rho)/\mathrm{d}\rho$.

Figure 3.7: Interpolation of the elasticity tensor with a 9th-order polynomials for the family of square-holed unit cells.

We expedite the computation of the element stiffness matrix during FEA by splitting Equation (3-39b) into four terms as follows (adapting the

integration for the two-dimensional case in plane stress):

$$
\begin{aligned}
\mathbf{K}^{(e)} &= \int_{A^{(e)}} \left(\mathbf{B}^{(e)}\right)^T \mathbf{C}^{(e)}\, \mathbf{B}^{(e)}\, t \mathrm{d}\Omega \\
&= \int_{A^{(e)}} \left(\mathbf{B}^{(e)}\right)^T \begin{bmatrix} C_{11}^{(e)} & C_{12}^{(e)} & 0 \\ C_{12}^{(e)} & C_{22}^{(e)} & 0 \\ 0 & 0 & C_{33}^{(e)} \end{bmatrix} \mathbf{B}^{(e)}\, t \mathrm{d}\Omega \\
&= C_{11}^{(e)} \underbrace{\int_{A^{(e)}} \left(\mathbf{B}^{(e)}\right)^T \begin{bmatrix} 1 & 0 & 0 \\ 0 & 0 & 0 \\ 0 & 0 & 0 \end{bmatrix} \mathbf{B}^{(e)}\, t \mathrm{d}\Omega}_{\mathbf{K}_{11}^{(e)}} + C_{22}^{(e)} \underbrace{\int_{A^{(e)}} \left(\mathbf{B}^{(e)}\right)^T \begin{bmatrix} 0 & 0 & 0 \\ 0 & 1 & 0 \\ 0 & 0 & 0 \end{bmatrix} \mathbf{B}^{(e)}\, t \mathrm{d}\Omega}_{\mathbf{K}_{22}^{(e)}} \\
&+ C_{33}^{(e)} \underbrace{\int_{A^{(e)}} \left(\mathbf{B}^{(e)}\right)^T \begin{bmatrix} 0 & 0 & 0 \\ 0 & 0 & 0 \\ 0 & 0 & 1 \end{bmatrix} \mathbf{B}^{(e)}\, t \mathrm{d}\Omega}_{\mathbf{K}_{33}^{(e)}} + C_{12}^{(e)} \underbrace{\int_{A^{(e)}} \left(\mathbf{B}^{(e)}\right)^T \begin{bmatrix} 0 & 1 & 0 \\ 1 & 0 & 0 \\ 0 & 0 & 0 \end{bmatrix} \mathbf{B}^{(e)}\, t \mathrm{d}\Omega}_{\mathbf{K}_{12}^{(e)}} \\
&= C_{11}^{(e)} \mathbf{K}_{11}^{(e)} + C_{22}^{(e)} \mathbf{K}_{22}^{(e)} + C_{33}^{(e)} \mathbf{K}_{33}^{(e)} + C_{12}^{(e)} \mathbf{K}_{12}^{(e)}. \qquad \text{(3-52)}
\end{aligned}
$$

In our code, we precompute and store the constant matrices $\mathbf{K}_{ij}^{(e)}$ $(ij = 11, 22, 33, 12)$, such that any update to $\mathbf{K}^{(e)}$ requires an efficient linear combination. Additionally, for regular meshes, these constant matrices $\mathbf{K}_{ij}^{(e)}$ are identical for all elements, so their memory cost is negligible. This entire process is valid only for a given Poisson's ratio (in this case: $\nu = 0.3$), and must be repeated for other values, as the relationship between C_{ij} and ν is nonlinear.

3.3.4 Limitations of Homogenization-Based Multiscale Analysis

It seems suitable to end this chapter with a brief overview of the limitations of the hierarchichal approach to homogenization-based analysis and optimization. In what follows, we list some of the main challenges that pertain to homogenization-based multiscale analysis and optimization, and its realization with addictive manufacturing, which is one of the main technologies utilized to build multiscale structures.

Adopted assumptions: As described in Section 3.3.1, homogenization theory assumes that the microstructures are infinitely periodic and at a much smaller length scale of the macroscopic structure. None of these are perfectly satisfied in the fabricated structure, with the main limitation being the fidelity that a 3D printer can fabricate its smallest feature.

Material properties: Material parameters like E and ν used in structural analysis are just approximations of the real values. Though some research has been done to reduce the performance mismatch between numerical analysis and experimental test on as-built parts (Xian et al., 2025), this is still a challenge in addictive manufacturing.

Microstructure compatibility: Without a compatibility formulation, neighboring unit cells of a multiscale structure may be disconnected. Some solutions to this problem from analytical to data-driven approaches were reviewed in Chapter 2.

While research has been done to address these points, in this work we focus on the numerical aspects of the topology optimization process.

3.4 Aspects of Numerical Optimization in Elastostatic Cloaking

Optimization in one of the main areas of engineering, and consists in finding the best design according to some suitable metric while satisfying a set of constraints. Mathematically, we seek some vector of design variables $\boldsymbol{z}$ that minimizes such metric posed as an objective or cost function $\mathcal{F}$. Mathematically, one can pose a minimization problem in the general form

$$\min_{\boldsymbol{z}} \quad \mathcal{F}(\boldsymbol{z}) \tag{3-53a}$$

$$\text{s.t.} \quad g_i \leq 0, \quad i = 1, \ldots, \mathrm{N}_i \tag{3-53b}$$

where g_i denotes the i-th inequality constraints of the problem. While equality constraints may also be introduced to this formulation, they are not relevant for the problems considered in our work.

It can be shown (Rao, 2019) that the Karush-Kuhn-Tucker conditions are necessary conditions at critical points (like relative minima) of $\mathcal{F}(\boldsymbol{z})$, and take the form

$$\mathcal{L}(\boldsymbol{z}, \boldsymbol{\lambda}) = 0 \qquad \text{(stationarity)} \tag{3-54a}$$

$$g_i(\boldsymbol{z}) \leq 0, \quad i = 1, \ldots, N_i \qquad \text{(primal feasibility)} \tag{3-54b}$$

$$\lambda_i \geq 0, \quad i = 1, \ldots, N_i \qquad \text{(dual feasibility)} \tag{3-54c}$$

$$\lambda_i g_i(\boldsymbol{z}) = 0, \quad i = 1, \ldots, N_i \qquad \text{(complementary slackness)}, \tag{3-54d}$$

where $\boldsymbol{\lambda}$ is the vector of Lagrange multipliers associated with the constraints, and the Lagrangian function is defined as

$$\mathcal{L}(\boldsymbol{z}, \boldsymbol{\lambda}) = \mathcal{F}(\boldsymbol{z}) + \sum_{i=1}^{\mathrm{N}_i} \lambda_i g_i(\boldsymbol{z}). \tag{3-55}$$

Since determining a global or even local minimum for practical engineering problems may be difficult or impossible, many optimization algorithms have been developed to search for a minimum given an initial guess and a search direction. The method of moving asymptotes (MMA) proposed by (Svanberg, 1987) consists of solving a similar optimization problem to that of Equation (3-53), and approximating the solution by iteratively solving subproblems that replace the original objective functions with convex approximations. This method has been widely applied to the context of structural optimization and is also utilized here based on the modified version presented by (Giraldo-Londoño and Paulino, 2021), which is more efficient for problems without constraints functions (except for box constraints on the design variables).

In our work, the MMA method is used to optimize the material (or metamaterial) distribution over the domain of a finite element discretized structure. Additional information on how the optimization problem is set up is provided in the following chapters.

4
Mechanical Cloaking via Static Condensation

Static condensation techniques were developed to reduce the computational cost intrinsic to the solution of linear systems. While some authors have used static condensation or the related super element method in the solution of topology optimization (Qiu et al., 2009), they typically apply it to reduce the computational cost, whereas we propose its application to decouple the design of the cloaking device from the surrounding strucutre.

Designing the cloaking device apart from its surroundings significantly reduces computational cost in both optimization and analysis, expediting the entire design process. This idea was first presented by Cheng et al. (2023), who posed it from a physical perspective, while we do so from a mathematical one. The advantage to our approach, is that it can be extended to other cases different from elastostatic settings.

In this chapter, we lay the foundation of our MOR-based approach to the solution of FEM-based mechanical cloaking problems. First, we briefly review the static condensation technique, followed by its application to elastostatic cloaking. Finally, we discuss future extensions to this work, in the form of unbiased and modal cloaking.

4.1
Review of Static Condensation

The first works that proposed condensing degrees of freedom in structural analyses are nowadays classified as static condensation because dynamic effects are ignored. Guyan (1965) proposed partitioning the linear system in Equation (3-38) into degrees of freedom that would be kept and those that would be removed. Irons (1965) instead derived the condensed equations from energy equations applied to structural eigenvalue problems, and also introduced the terms “masters” and “slaves” in this context to refer to which DOFs would be kept or removed, respectively. When the stiffness and mass matrices are reduced to their condensed form (i.e., without slaves), dynamic effects are ignored, so this method only yields exact solution to static problems, hence it is called static (or Guyan) condensation (Qu, 2004).

We review the main steps of the derivation of static condesations equations by first considering a well-posed linear system describing the quasi-static structural behavior, in which we are interested to determine the displacement field of some master DOFs. Equation (3-38) is partitioned as

$$\begin{bmatrix} \mathbf{K}_{\mathrm{mm}} & \mathbf{K}_{\mathrm{ms}} \\ \mathbf{K}_{\mathrm{sm}} & \mathbf{K}_{\mathrm{ss}} \end{bmatrix} \begin{Bmatrix} \mathbf{u}_{\mathrm{m}} \\ \mathbf{u}_{\mathrm{s}} \end{Bmatrix} = \begin{Bmatrix} \mathbf{f}_{\mathrm{m}} \\ \mathbf{f}_{\mathrm{s}} \end{Bmatrix}, \tag{4-1}$$

where m and s denote the master and slave DOFs, respectively. Solving Equation (4-1) for the $\mathbf{u}_{\mathrm{s}}$ yields

$$\mathbf{u}_{\mathrm{s}} = \mathbf{K}_{\mathrm{ss}}^{-1} \left(\mathbf{f}_{\mathrm{s}} - \mathbf{K}_{\mathrm{sm}} \mathbf{u}_{\mathrm{m}} \right), \tag{4-2}$$

which can then be substituted back into the first line of Equation (3-41) to arrive at the reduced system

$$\mathbf{K}_{\mathrm{R}} \mathbf{u}_m = \mathbf{F}_{\mathrm{R}}, \tag{4-3}$$

where

$$\mathbf{F}_{\mathrm{R}} = \mathbf{F}_{\mathrm{m}} - \mathbf{K}_{\mathrm{ms}} \mathbf{K}_{\mathrm{ss}}^{-1} \mathbf{F}_{\mathrm{s}}, \tag{4-4a}$$

$$\mathbf{K}_{\mathrm{R}} = \mathbf{K}_{\mathrm{mm}} - \mathbf{K}_{\mathrm{ms}} \mathbf{K}_{\mathrm{ss}}^{-1} \mathbf{K}_{\mathrm{sm}}. \tag{4-4b}$$

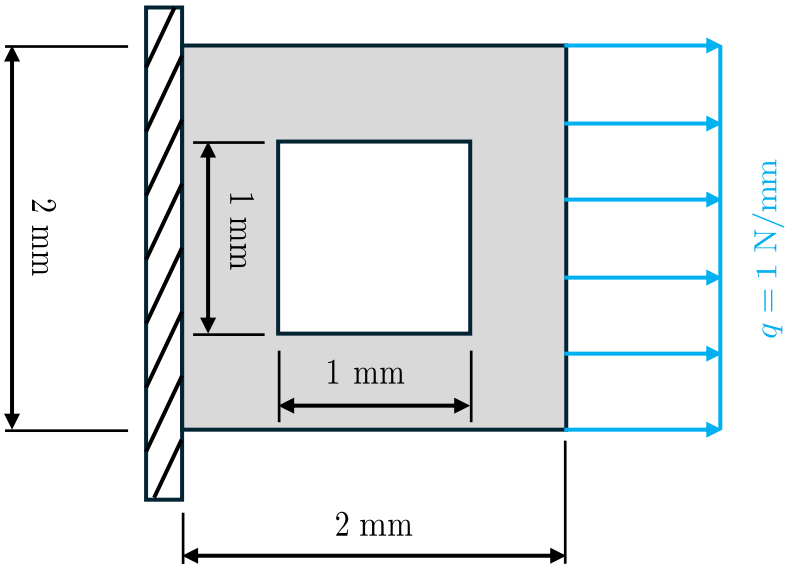

Figure 4.1: Square-holed unit cell domain discretized subject to a uniform distributed load on the right edge.

We will now illustrate this method by analyzing the structural response of a singular unit cell with a full and a condensed system. Additionally, we contrast these solutions with that obtained with a single element with homogenized properties as described in Section 3.3. For this purpose, consider the unit cell with dimensions shown in Figure 4.1 and thickness 0.4 mm fixed on the left side and under a uniform distributed tensile load with magnitude $q = 1$ N/mm on the right side. The material properties of the constituent are $E = 200$ GPa and $\nu = 0.3$.

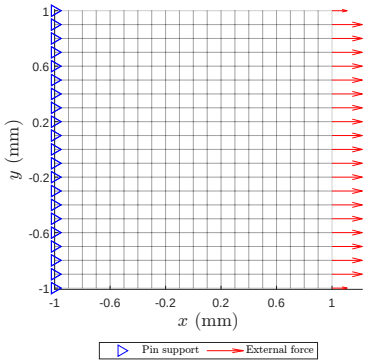

(a) Solid UC: FS domain.

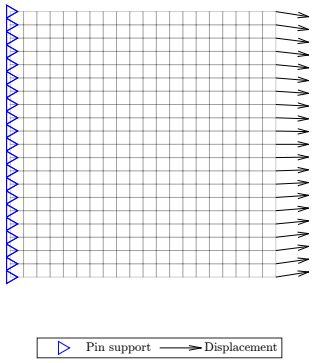

(b) Solid UC: FS displacement.

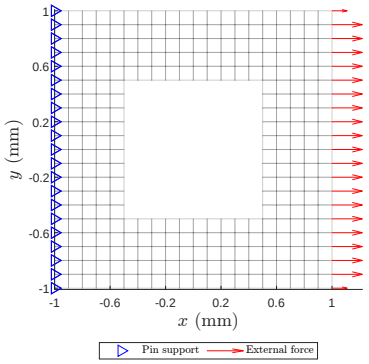

(c) Holed UC: FS domain.

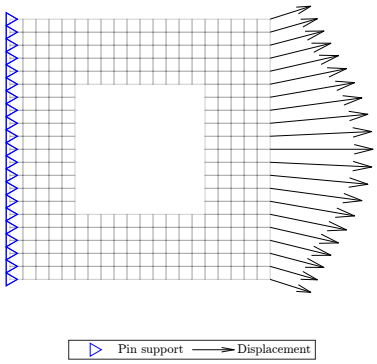

(d) Holed UC: FS displacement.

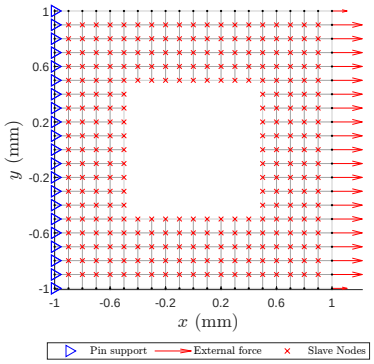

(e) Holed UC: ROM domain.

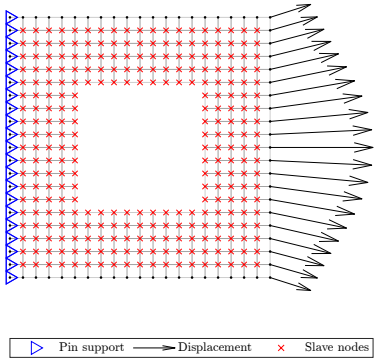

(f) Holed UC: ROM displacement.

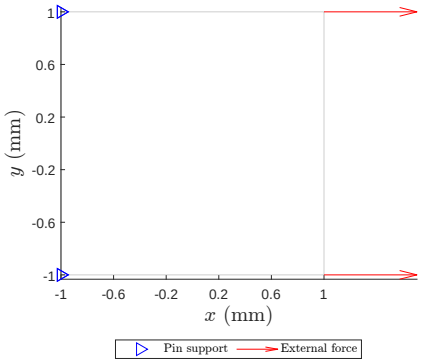

(g) Holed UC: HOM domain.

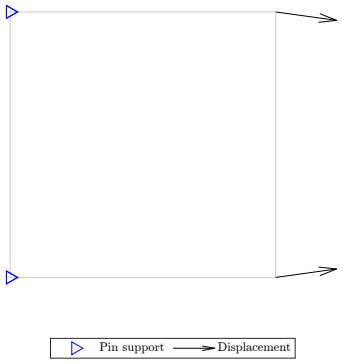

(h) Holed UC: HOM displacement.

Figure 4.2: Structural response of solid and holed ($\rho = 0.75$) unit cells subject to uniform distributed load. Comparison between full-scale (FS), reduced-order model (ROM), and homogenized (HOM) results. Displacement vectors scale factor: 10 times.

First, we investigate the influence of introducing a hole into the unit cell, which is originally meshed into 20×20 Q4 elements, as shown in Figure 4.2a. This coarse mesh was chosen to clearly display the difference from each approach. Figure 4.2b shows that the solid unit cell presents an almost homogeneous horizontal displacement field on the right edge, except for a small variation of the nodes close to the corners due to the Poisson effect. When the square hole is introduced, both the magnitude and the direction of the nodal displacements are significantly affected, as shown in Figure 4.2d.

By means of static condensation, we can reduce this system via a master-slave partition, keeping only the nodes on the boundary, as shown in Figure 4.2e. We solved the system Equation (4-3) for the masters and substituted the solution in Equation (4-2) for the slaves. Figure 4.2f shows that this method yields the same displacement field at the boundary as its full-scale counterpart. In fact, the entire solution for both master and slaves matches the full-scale displacement field within machine precision.

Next, we compare the results with a single unit cell with interpolated homogenized elastic properties using the approach presented in Section 3.3.3, as done in most hierarchical multiscale topology optimization approaches. Although homogenization allows us to drastically reduce the number of DOFs (see Figure 4.2g), it comes at the cost of not considering significant variations at the microscale level. It is worthy no mention thatusing higher-order elements in the finite element formulation *does not solve this problem*, since microstructural features are completely disregarded.

This simple illustrative example shows the trade off between efficiency and accuracy that comes from using a homogenization-based approach to multiscale analysis. However, this effect reduces as scale separation and periodicity of the unit cells are better approximated. Still, 3D-printed multiscale parts may not approach this well enough for structural analysis and optimization. Therefore, approaches like static condensation can deliver high accuracy at a reasonably low computational cost.

4.2 Static condensation and the CBC paradigm

In this section we present the mathematical argument to our elastostatic cloaking approach, starting with a mathematical definition of the problem. Here, we use static condensation to prove the CBC paradigm in a discretized setting suitable for finite element analysis, which can be implemented for virtually any type of displacement-based target behavior problem (i.e., both mechanical cloaking and shape matching). However, static condensation is not explicitly executed during the optimization process, only for the derivation presented in this section. Moreover, while we could separate the cloak and surrounding regions into substructures using superelements, this is not needed here, as we focus on one region at a time, namely Ω_{sur} in the derivation, and Ω_{hole} in the implementation. We suggest a more advanced superelement-based solution in Section 7.1.2 for microstructure design, which is outside of the scope of this work.

Consider an virtual reference domain Ω_{ref} surrounded by a boundary $\Gamma_{\text{BC}} = \partial\Omega_{\text{ref}}$ where natural and boundary conditions are applied. The mechanical cloaking problem consists in designing a structure in Ω_{cloak} to neglect the influence of a topological feature like the hole Ω_{hole} on the mechanical reponse of the structure compared to that of Ω_{ref} when subjected to the same boundary conditions. Our current study limits to the linear elastic quasi-static case, and the mechanical behavior to be compared is the displacement field in the surrounding region, Ω_{sur}. Figure 4.3 shows the reference domain and its partitions, including the inner and outer boundaries of the cloaking device, namely Γ_{in} and Γ_{out}, respectively.

The traditional approach to optimization-based elastostatic cloaking is to define an optimization problem where the design variables are related to the material (or metamaterial) distribution in the cloaking device, and the objective function is a displacement-based error metric. Table 4.1 presents some of these metrics, where $\Delta\mathbf{u} = \mathbf{u} - \mathbf{u}^0$ is the difference between the displacement of the physical and virtual domains, $\mathbf{u}$ and $\mathbf{u}^0$, respectively. Additionally, the index i spans over all of the N_{check} DOFs in the surrounding region, which means that it is only required to recover the displacement field in the surrounding region.

Mathematically, the objective function for the traditional elastostatic cloaking paradigm can be written in the form

$$\mathcal{F} = (\Delta\mathbf{u}^*)^T \mathbf{W} \Delta\mathbf{u}^*, \tag{4-5}$$

where $\mathbf{W}$ is a weight matrix. The star superscript denotes that only some

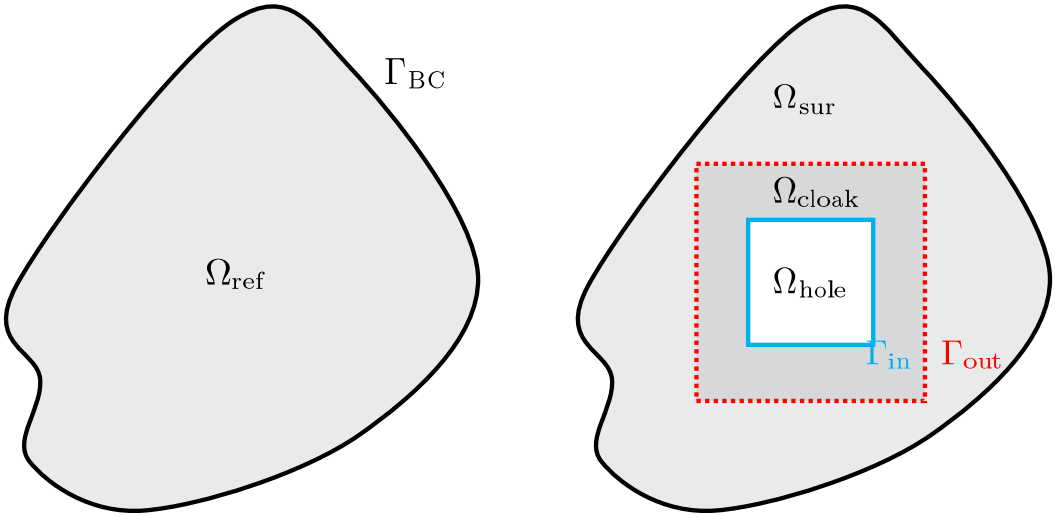

(a) Virtual domain. (b) Physical domain.

Figure 4.3: Domain and partitions used in mechanical cloaking problems (Sozio et al., 2023, adapted).

Table 4.1: Error metrics used in mechanical cloaking analysis

Error Metric	**Equation**[†]
Normalized Norm of Error (Bückmann et al., 2015)	$\Delta = \frac{\sqrt{\sum_i (\Delta u_i)^2}}{\sqrt{\sum_i (u_i^0)^2}}$
Root Mean Square Error (RMSE) (Fachinotti et al., 2018)	$\sqrt{\frac{1}{N_{\text{check}}} \sum_i \lVert \Delta u_i \rVert_2^2}$
Weighted Least Squares (Sanders et al., 2021a)	$(\Delta \mathbf{u})^T \mathbf{K}\, \Delta \mathbf{u}$
2-norm of error[‡] (Sozio et al., 2023)	$\int_{\Omega_{\text{sur}}} \lVert \Delta u \rVert_2^2 \, dV$

[†] Adapted from reference for consistent notation and single-load cases.
[‡] Authors used a continuous formulation of the problem.

chosen DOFs are selected for the displacement error function, and they are mathematically obtained by multiplying $\Delta\mathbf{u}$ by a boolean gather matrix $\boldsymbol{L}^*$. Since the displacement field must be recovered for the elements in Ω_{sur} at least, $\boldsymbol{L}^*$ gathers the DOFs associated with them. Further information on this traditional paradigm including the sensitivity analysis is provided in Appendix A.3.

Although these displacement-based error metrics directly address the cloaking problem, i.e., reducing the error $\Delta\mathbf{u}$ in Ω_{sur}, they do not scale well with the size and discretization of the surrounding region. Cheng et al. (2023) proposed instead to approximate the mechanical behavior alongside the interface Γ_{out} of the physical domain compatible to its virtual counterpart, i.e., the compatible boundary condition paradigm to mechanical cloaking.

To illustrate this concept, consider an 150-mm side square plate made of Nylon ($E = 3$GPa, $\nu = 0.4$) subjected to a uniform distributed compressive load of magnitude 100 N/mm, as proposed by Fachinotti et al. (2018). Figure 4.4 shows that the displacement field of the virtual domain (i.e., that without the hole) changes with the introduction of the hole. However, if we apply boundary conditions Γ_{out} compatible to the mechanical response from the virtual domain, the original displacement field is recovered. Figures 4.4c and 4.4d show that either compatible displacement or forces can be used to achieve this goal. Our purpose is to design a cloaking device that responds with the compatible boundary condition on Γ_{out}, which we explain using static condensation.

We start by rewriting the first line of Equation (4-1) as follows:

$$\mathbf{f}_m = \left(\mathbf{K}_{\text{mm}}^{\text{sur}} + \mathbf{K}_{\text{mm}}^{\text{cloak}}\right)\mathbf{u}_{\text{m}} + \left(\mathbf{K}_{\text{ms}}^{\text{sur}} + \mathbf{K}_{\text{ms}}^{\text{cloak}}\right)\mathbf{u}_{\text{s}}, \tag{4-6}$$

where the stiffness matrix was partitioned into the $\mathbf{K}^{\text{sur}}$ and $\mathbf{K}^{\text{cloak}}$ (see Figure 4.3b) that contain only elements from the surrounding and cloak regions, respectively.

Let us define the nodes and DOFs that belong Γ_{out} as pertaining to the master partition, and not the slaves. Therefore, terms like $\mathbf{K}_{\text{ms}}^{\text{sur}} = \mathbf{0}$, since the master elements in Ω_{sur} contain no slaves DOFs by our partition. Therefore, we can rewrite Equation (4-6) as

$$\mathbf{f}_m = \mathbf{K}_{\text{mm}}^{\text{sur}}\mathbf{u}_{\text{m}} + \mathbf{K}_{\text{mm}}^{\text{cloak}}\mathbf{u}_{\text{m}} + \mathbf{K}_{\text{ms}}^{\text{cloak}}\mathbf{u}_{\text{s}}, \tag{4-7}$$

Notice that the external force on the master is that applied on Γ_{BC}, which we denote as $\mathbf{f}_{\text{BC}}^{\text{sur}}$ (read as "force exerted on Ω_{sur} at Γ_{BC}"). Additionally, due to Newton's 3rd Law of Motion, the external force exerted on the cloak at the intereface is the opposite of that exerted on the surrounding region, that is

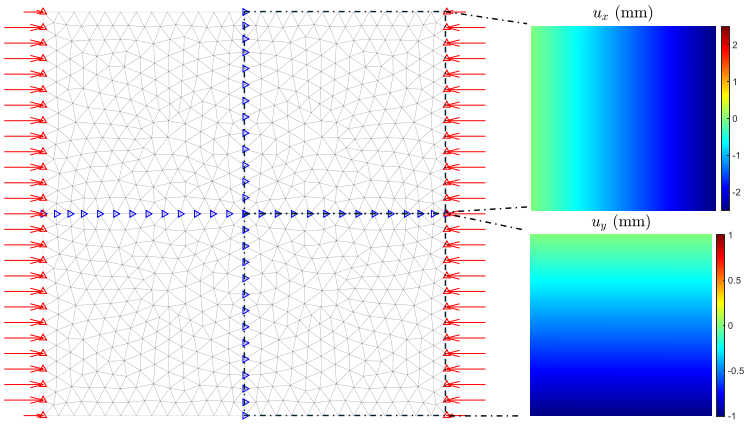

(a) Virtual domain (Ω_{ref}).

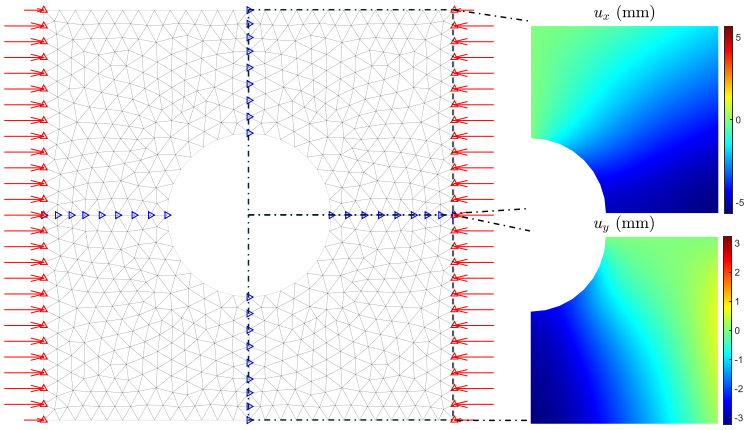

(b) Physical region: uncloaked.

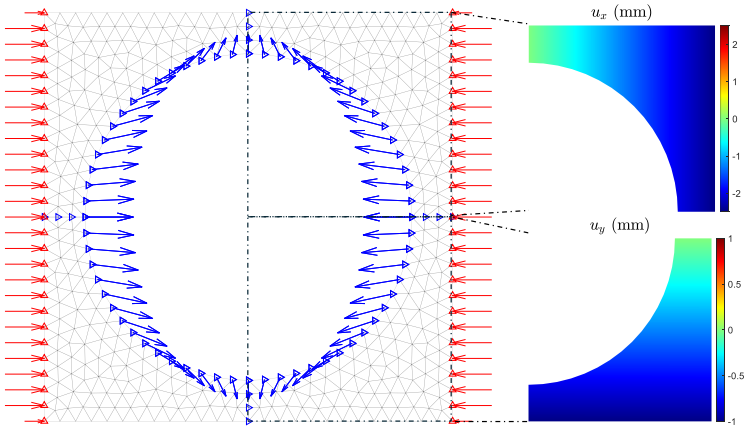

(c) Surrounding domain (Ω_{sur}): compatible displacement.

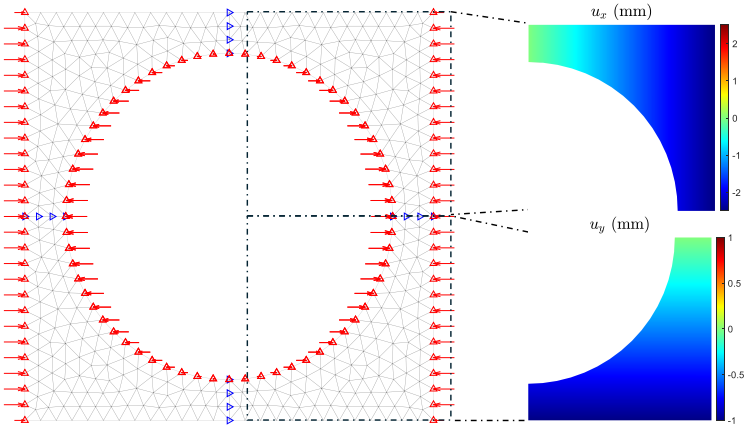

(d) Surrounding domain (Ω_{sur}): compatible forces.

Figure 4.4: Domain and partitions used in mechanical cloaking problems. The cloak region Ω_{cloak} was removed from (c) and (d) for visual clarity.

$$\mathbf{f}_{\text{out}}^{\text{cloak}} = \mathbf{K}_{\text{mm}}^{\text{cloak}}\mathbf{u}_{\text{m}} + \mathbf{K}_{\text{ms}}^{\text{cloak}}\mathbf{u}_{\text{s}} = -\mathbf{f}_{\text{out}}^{\text{sur}}. \tag{4-8}$$

Finally, we can rewrite Equation (4-7) in its final form as:

$$\underbrace{\mathbf{f}_{\text{m}}}_{\mathbf{f}_{\text{BC}}^{\text{sur}}} = \mathbf{K}_{\text{mm}}^{\text{sur}}\mathbf{u}_{\text{m}} + \underbrace{\mathbf{K}_{\text{mm}}^{\text{cloak}}\mathbf{u}_{\text{m}} + \mathbf{K}_{\text{ms}}^{\text{cloak}}\mathbf{u}_{\text{s}}}_{-\mathbf{f}_{\text{out}}^{\text{sur}}} \tag{4-9}$$

$$\underbrace{\mathbf{f}_{\text{BC}}^{\text{sur}} + \mathbf{f}_{\text{out}}^{\text{sur}}}_{\mathbf{f}^{\text{sur}}} = \mathbf{K}_{\text{mm}}^{\text{sur}}\mathbf{u}_{\text{m}}$$

$$\mathbf{f}^{\text{sur}} = \mathbf{K}_{\text{mm}}^{\text{sur}}\mathbf{u}_{\text{m}}, \tag{4-10}$$

where $\mathbf{f}_{\text{m}}$ is the total external force exerted on the master degrees of freedom, which is composed of those from the external boundary ($\mathbf{f}_{\text{BC}}^{\text{sur}}$) and the interface with the cloaking device ($\mathbf{f}_{\text{out}}^{\text{sur}}$).

If the linear system in Equation (4-10) is well posed (i.e., nonsingular $\mathbf{K}_{\text{mm}}^{\text{sur}}$ once appropriate boundary conditions are applied), it will always yield the same solution $\mathbf{u}_{\text{m}}$ as long as $\mathbf{f}_{\text{m}}$ is the same. $\mathbf{f}_{\text{m}}$ depends on external boundary conditions (considered here to be constant) and the force at the cloak-surrounding interface (depends on the cloak design). Therefore, we conclude our proof by asserting that a compatible nodal force at Γ_{out} will yield exactly the reference displacement at Γ_{sur}, as illustrated in Figure 4.4d.

In the elastostatic setting, the proof to our approach is a discretized version of the CBC paradigm (Cheng et al., 2023), with the advantage that it can be extended to other settings, as discussed in the next section. On the other hand, the physical-based argument proposed by Cheng et al. (2023) is more generic and can theoretically be extended to applications that do not rely on FEM discretization.

Since either type of boundary condition (essential or natural) can be imposed on the cloak-surrounding interface to produce a cloaking effect as shown in Figure 4.4, one can define two categories of cloaking, depending on which type of boundary condition is prescribed, and which is approximated using an optimization algorithm. In this simple example, we discretized the domain with circular hole using linear triangular elements to easily represent the circular boundaries Γ_{in} and Γ_{out}. Figure 4.4 shows that if either displacements (in blue) or nodal forces (in red) are imposed on the cloak-surrounding interface, the original displacement in the surrounding region is recovered. Table 4.2 presents both categories of CBC-based elastostatic cloaking.

To implement the CBC-paradigm, we recast the generic topology opti-

Table 4.2: Categories of MOR-based mechanical cloaking in the context of elastostatic cloaking.

Cloaking type	**Prescribe on Γ_{out}**	**Approximate on Γ_{out}**
Natural	Forces ($\mathbf{f}_{\text{out}}^{\text{cloak}} = \overline{\mathbf{f}}_{\text{out}}^{\text{cloak}}$)	Displacements
Essential	Displacements ($\mathbf{u}_{\text{out}} = \overline{\mathbf{u}}_{\text{out}}$)	Forces

mization problem from Equation (2-1) in its FEM-discretized form as

$$\min_{\boldsymbol{\rho}} \quad \mathcal{F}(\mathbf{u}(\boldsymbol{\rho}), \boldsymbol{\rho}) = (\Delta \mathbf{f}_{\text{out}})^T \Delta \mathbf{f}_{\text{out}} \tag{4-11a}$$

$$\text{s.t.} \quad \rho_{\min}^{(e)} \leq \rho^{(e)} \leq \rho_{\max}^{(e)}, \quad e = 1, \ldots, \mathrm{N}_e \tag{4-11b}$$

$$\text{with} \quad \mathbf{f} = \mathbf{K}(\boldsymbol{\rho})\, \mathbf{u} \tag{4-11c}$$

where $\mathbf{u}$ is the displacement solution to Equation (4-11c) that depends on the vector of design variable $\boldsymbol{\rho}$, which contains one (or more) parameter associated to each one of the N_e elements in the finite element mesh. In multiscale topology optimization, the design variable often takes the form of the density of the unit cell (repeating or not), which in turn determines the physical properties of the microstructure, as shown in Figure 3.6 and consequently the stiffness matrix. The objective in Equation (4-11a) is basically the nodal force error at Γ_{out}, where

$$\Delta \mathbf{f}_{\text{out}} = \mathbf{f}_{\text{out}} - \overline{\mathbf{f}}_{\text{out}}. \tag{4-12}$$

Notice that we chose a nested optimization approach, where the structural equilibrium is satisfied at each iteration of the process. While the objective function is computed from the loads at the cloaking-surrounding interface, a suitable measure of cloaking performance is still taken to compare our final results.

The sensitivity analysis of Equation (4-11a) is presented in Appendix A.1 in detail, but its full derivation depends on the material parameterization introduced in the next chapters.

5
Multi-metamaterial Topology Optimization

We present in this chapter our homogenization-based multi-material framework applied to the CBC-based elastostatic cloaking approach described in Section 4.2. We designed a simple family of lattice microstructures which we introduced to a deterministic algorithm that simultaneously selects the optimal microstructure and density. Once a crisp "black-and-white" design is achieved (i.e., when the microstructure of each finite element is clearly defined), an efficient optimization algorithm is run to fine tune the element densities. In what follows, we introduce the implementation details of the microstructure family and the proposed optimization framework, and finish the chapter with a simple numerical example to validate the sensitivity analysis.

5.1
Family of Mechanical Metamaterials

In this work, we generated four families of 2-dimensional truss-like microstructures that can be represented in a homogenization-based multiscale FEA using Q4 elements. For simplicity, we assume that unit cells are perfectly square, with side length L and smallest feature (or truss thickness) t, as shown for the crossed truss-like pattern in Figure 5.1.

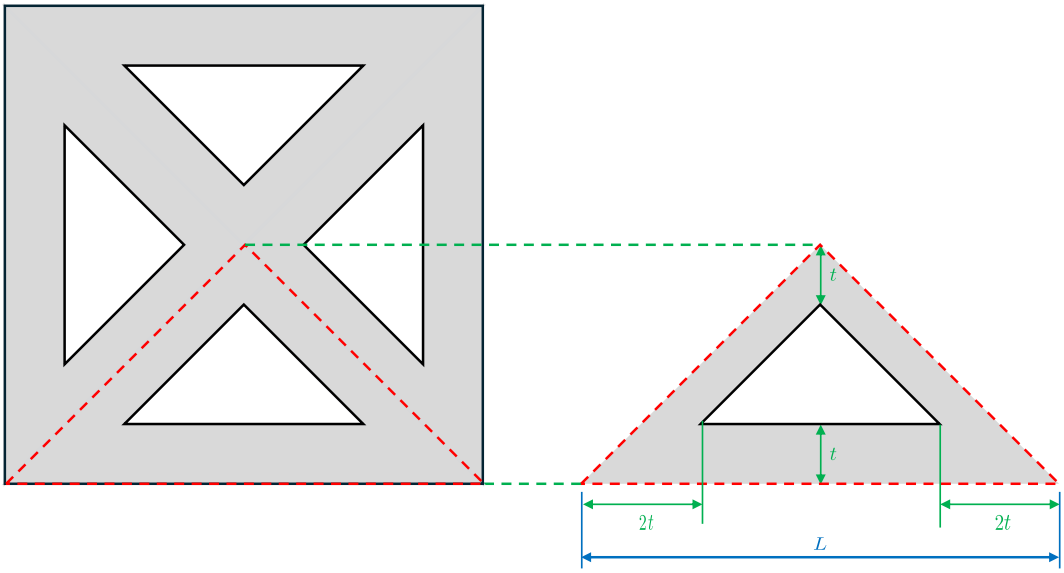

Figure 5.1: Crossed trusses unit cell ($\rho = 0.75$) and geometric dimensions of the repeating pattern.

By removing parts of the edges of the crossed trusses unit cell, we develop horizontal and vertical versions of this microstructures, introducing some level

of anisotropy to their effective properties. These are shown in Table 5.1 alongside the square-holed unit cell, and are numbered as materials 1 through 4, which are candidate materials (or metamaterials) in the optimization framework presented in this chapter. Notice that materials 2 and 3 are not completely self-compatible, i.e., they may be partially disconnected depending on how they are placed. This may introduce some discrepancy when validating results in a full-scale analysis, as discussed in Section 3.3.4.

Table 5.1: Metamaterial families breakdown.

Mat. #	**Unit Cell**	**Geometric Relationships**
1	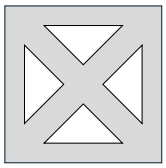	$\rho(t) = \dfrac{8t(L-2t)}{L^2}$ $t(\rho) = \dfrac{L}{4}\left(1-\sqrt{1-\rho}\right)$
2	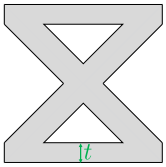	$\rho(t) = \dfrac{2t(3L-5t)}{L^2}$ $t(\rho) = \dfrac{3L}{10}\left(1-\sqrt{1-\frac{10}{9}\rho}\right)$
3	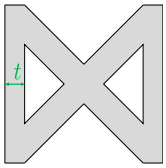	$\rho(t) = \dfrac{2t(3L-5t)}{L^2}$ $t(\rho) = \dfrac{3L}{10}\left(1-\sqrt{1-\frac{10}{9}\rho}\right)$
4	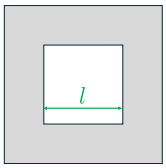	$\rho(l) = \dfrac{L^2-l^2}{L^2}$ $l(\rho) = L\sqrt{1-\rho}$

The geometric relationships between the density ρ and t shown in Table 5.1 allows us to determine box constraints on the density ($\rho_{\min}$ and $\rho_{\max}$) according to manufacturing limitations. For example, consider the metamaterial family 1 with $L = 50.0$ mm and a smallest feature size that we can reliably print using additive manufacturing set to $t = 1.0$ mm. The minimum density for this material can be estimated as

$$\rho_{\min}(t_{\min}) = \frac{8(1.0\text{ mm})\left[(50.0\text{ mm}) - 2(1.0\text{ mm})\right]}{(50.0\text{ mm})^2} \approx 0.15. \tag{5-1}$$

This value is just used here to illustrate how to obtain an initial estimate for the limits of the design space using families of microstructures. Practical applications must consider several other parameters outside of the scope of this

work, so we select the following values for the box constraint on the densities: $\rho_{\min} = 0.1$ and $\rho_{\max} = 0.9$.

Finally, we homogenize the elasticity tensor components and fit it to a continuous function of ρ, as discussed in Sections 3.3.2 and 3.3.3. Figure 5.2 shows the fitted functions for each material, where it is clear that no singular metamaterial family is stiffer in all cases. For instance, material 4 (square-holed unit cell) displays the highest in-plane normal components (C_{11} and C_{22}), but the lowest in the other two directions. Likewise, materials 2 and 3 differ by a rotation of 90 degrees, so they posses inverted in-plane components (see Figures 5.2a and 5.2b), but behave the same in shear and out-of-plane, as shown in Figures 5.2c and 5.2d.

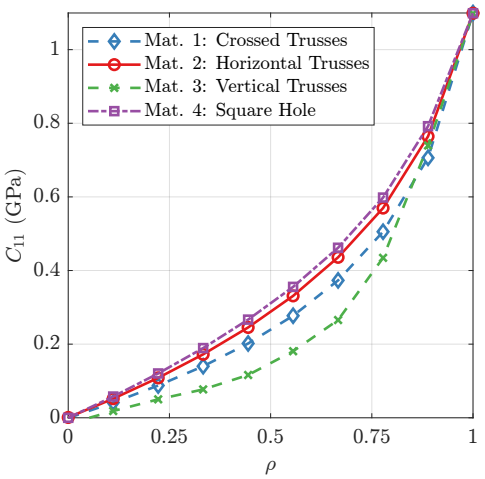

(a) C_{11}.

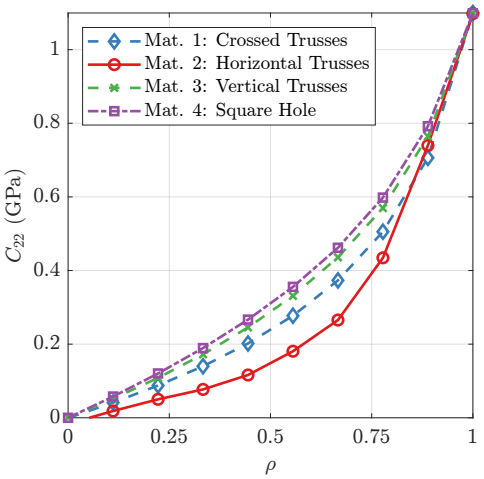

(b) C_{22}.

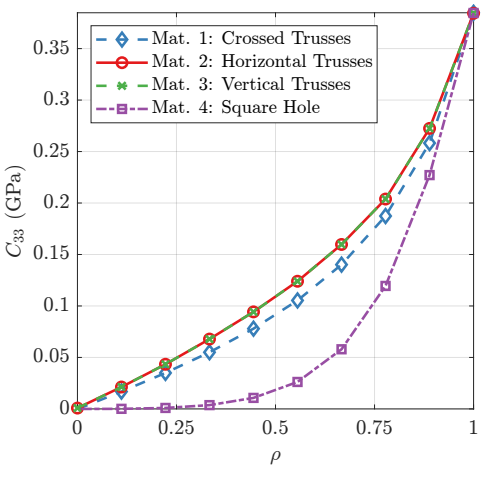

(c) C_{33}.

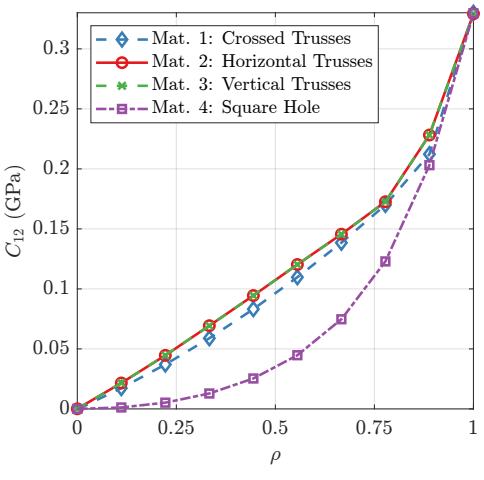

(d) C_{12}.

Figure 5.2: Homogenized elasticity tensor components fitted to 9$^{\text{th}}$-order polynomials for all candidate materials. Material properties of the solid material: Young modulus $E = 1.0$ GPa and Poisson's ratio $\nu = 0.3$.

In this example, we adopted a 9th-order polynomial function for the curve-fitting algorithm. Though lower-order polynomials could fit the data

well, only 9th-order polynomial presented no local minima in the region of ρ used in our numerical examples. While this is not a strict requirement, this condition may improve convergence of the optimization algorithm, and it comes at a negligible additional cost compared to lower-order polynomials.

The continuous distribution of material properties is the main advantage of using functionally-graded microstructures in multiscale TO, since there is a wide array of properties to choose from instead of simply choosing whether an element exists or not as typically done in mono-scale TO.

5.2 Material Selection Algorithm

Among several methods presented in the literature for selecting candidate materials in topology optimization, the Discrete Material Optimization (DMO) stands out as a straightfoward and efficient approach. The DMO was originally applied by Stegmann and Lund (2005) to find optimal fiber angle orientation and material distribution of composite structures, and it has been applied to multiscale TO in two (Sanders et al., 2018) and three (Sanders et al., 2021b) dimensions, typically in the context of compliance minimization.

However, while DMO allows for the discrete selection of a single candidate material per finite element in a mesh, it cannot easily account for a simultaneous continuous variable, say, the density of that candidate metamaterial. In the context of homogenization-based multiscale TO, it is easier to optimize either the density distribution or select the material, but not both simultaneously without a data-driven approach. To address this problem, we adapt the discrete-continuous parameterization (DCP) technique perform both tasks. DCP was originally developed by Luo et al. (2020) to avoid local optima in the optimization of continuous orientation of orthotropic materials, but to the best of this author's knowledge, it has not yet been adapted to the context of homogenization-based multiscale TO.

To explain our proposed technique, we recast the optimization problem in Equation (4-11) as

$$\min_{\mathbf{z}} \quad \mathcal{F}(\mathbf{u}(\mathbf{z}), \mathbf{z}) = (\Delta\mathbf{f}_{\text{out}})^T \Delta\mathbf{f}_{\text{out}} \tag{5-2a}$$

$$\text{s.t.} \quad \mathbf{z}_{\min}^{(e)} \leq \mathbf{z} \leq \mathbf{z}_{\max}, \quad e = 1, \ldots, \mathrm{N}^{(e)} \tag{5-2b}$$

$$\text{with} \quad \mathbf{f} = \mathbf{K}(\mathbf{z})\,\mathbf{u}, \tag{5-2c}$$

where $\mathbf{z}$ is the global design variable containing the element contributions that are typically stored as

$$\mathbf{z}^{(e)} = \begin{bmatrix} \boldsymbol{\rho}^{(e)} & \boldsymbol{\xi}^{(e)} \end{bmatrix}. \tag{5-3}$$

In Equation (5-3), the vector $\boldsymbol{\rho}^{(e)}$ represents *how much* of each material is used (i.e., the density) in element e, while $\boldsymbol{\xi}^{(e)}$ determines which candidate material is selected. These variables are defined as:

$$\boldsymbol{\rho}^{(e)} = \left\{ \rho_1^{(e)} \quad \cdots \quad \rho_M^{(e)} \right\} \qquad \text{and} \tag{5-4a}$$

$$\boldsymbol{\xi}^{(e)} = \left\{ \xi_1^{(e)} \quad \cdots \quad \xi_M^{(e)} \right\}, \tag{5-4b}$$

where M is the number of candidate metamaterial families.

Each component $\xi_m^{(e)} \in [0, 1]$ is a *material fraction* that indicates whether material m is active in element e ($\xi_m^{(e)} = 1$) or not ($\xi_m^{(e)} = 0$). Since $\xi_m^{(e)}$ is a continuous variable, we select a single candidate material by means of the DMO formula:

$$w_i^{(e)} = \left(\xi_i^{(e)}\right)^p \prod_{k=1, k\neq i}^{M} \left[1 - \gamma \left(\xi_i^{(e)}\right)^p\right], \tag{5-5}$$

where p is a penalization parameter that steers the weight to 0 or 1 as it increases from 1 to a high enough value. The factor γ introduced Sanders et al. (2018) may also be subject to continuation by running a simpler problem without DMO ($\gamma = 0$), then gradually approximating the result with DMO ($\gamma = 1$).

We follow the suggestion by Stegmann and Lund (2005) to normalize the weights from Equation (5-5) as follows:

$$\overline{w}_i^{(e)} = \frac{w_i^{(e)}}{W^{(e)}}, \tag{5-6}$$

$$W^{(e)} = \sum_{m=1}^{M} w_m^{(e)}, \tag{5-7}$$

which ensures that the normalized weights $\overline{w}_i^{(e)}$ add to the unity.

It is convenient to store the normalized weights and the components of the elasticity tensor as column vectors, as shown in:

$$\overline{\mathbf{w}}^{(e)}(\boldsymbol{\xi}^{(e)}) = \left\{ \overline{w}_1^{(e)}(\boldsymbol{\xi}^{(e)}) \quad \cdots \quad \overline{w}_M^{(e)}(\boldsymbol{\xi}^{(e)}) \right\}^T \qquad \text{and} \tag{5-8a}$$

$$\mathbf{C}_{ij}^{(e)}(\boldsymbol{\rho}^{(e)}) = \left\{ C_{ij,m}(\rho_1^{(e)}) \quad \cdots \quad C_{ij,m}(\rho_M^{(e)}) \right\}^T, \tag{5-8b}$$

where $\overline{\mathbf{w}}^{(e)}$ contains the normalized weights computed from the material fraction $\boldsymbol{\xi}^{(e)}$. Additionally, $\mathbf{C}_{ij,m}^{(e)}$ contains the elasticity tensor's (ij)-component of candidate material m, that is computed from its respective density $\rho_m^{(e)}$ for element e.

The element stiffness matrix can be computed efficiently with Equa-

tions (5-8a) and (5-8b) by rewriting Equation (3-52) as

$$\begin{aligned}\mathbf{K}^{(e)} = &\left[\left(\overline{\mathbf{w}}^{(e)}\right)^T \mathbf{C}_{11}^{(e)}\right] \mathbf{K}_{11}^{(e)} + \left[\left(\overline{\mathbf{w}}^{(e)}\right)^T \mathbf{C}_{22}^{(e)}\right] \mathbf{K}_{22}^{(e)} \\ &+ \left[\left(\overline{\mathbf{w}}^{(e)}\right)^T \mathbf{C}_{33}^{(e)}\right] \mathbf{K}_{33}^{(e)} + \left[\left(\overline{\mathbf{w}}^{(e)}\right)^T \mathbf{C}_{12}^{(e)}\right] \mathbf{K}_{12}^{(e)}. \end{aligned} \tag{5-9}$$

With the final expression of the stiffness matrix defined, we solve the mechanical cloaking problem in Equation (5-2) with the sequential quadratic programming optimization algorithm from MATLAB's `fmincon` function. Once the optimization process reaches a threshold for the normalized weights $\overline{\mathbf{w}}^{(e)}$, indicating that an optimal material distribution was chosen, we run the simplified problem from Equation (4-11) with only the densities as design variables, which allows us to fine tune the density distribution for a given material selection. We will distinguish these methods as single and multi-material optimization frameworks for when the design variable is $\boldsymbol{\rho}$ (as in Equation (4-11a)) or $\mathbf{z}$ (as in Equation (5-2a)), respectively.

5.3 Sensitivity Analysis Validation

We finish this chapter with a detailed presentation of the sensitivity analysis of our single and multi-material framework. For this purpose, we compute the relative error between numerical and analytical sensitivities of the objective function with the relative error in the form:

$$\text{Relative Error} = \frac{\left\| \left(\dfrac{\partial \mathcal{F}}{\partial \boldsymbol{z}}\right)_{\text{N}} - \left(\dfrac{\partial \mathcal{F}}{\partial \boldsymbol{z}}\right)_{\text{A}} \right\|_2}{\left\| \left(\dfrac{\partial \mathcal{F}}{\partial \boldsymbol{z}}\right)_{\text{A}} \right\|_2}, \tag{5-10}$$

where $(\partial \mathcal{F}/\partial \boldsymbol{z})_{\text{A}}$ is the analytical gradient derived in Appendix A.2, and $(\partial \mathcal{F}/\partial \boldsymbol{z})_{\text{N}}$ is the numerical gradient of the design variables. We compute the i-th component of the numerical gradients about a reference value $\boldsymbol{z} = \boldsymbol{z}_0$ with the following methods:

$$\text{Forward Finite Diff. (FFD)} : \left(\frac{\partial \mathcal{F}}{\partial z_i}\right)_{\text{N}} = \frac{\mathcal{F}(z_i + h) - \mathcal{F}(z_i)}{h}, \tag{5-11a}$$

$$\text{Central Finite Diff. (CFD)} : \left(\frac{\partial \mathcal{F}}{\partial z_i}\right)_{\text{N}} = \frac{\mathcal{F}(z_i + h) - \mathcal{F}(z_i - h)}{2h}, \tag{5-11b}$$

$$\text{Complex Step Method (CSM)} : \left(\frac{\partial \mathcal{F}}{\partial z_i}\right)_{\text{N}} = \frac{\text{Im}(\mathcal{F}(z_i + ih))}{h}, \tag{5-11c}$$

where h is the step size and i is the imaginary unit. The expressions in Equation (5-11) tend to approach the exact value of the derivative as $h \to 0$

in theory, but in computational implementation, the truncation error reduces while the round-off error increases for sufficiently small step sizes. However, since there is not subtraction in the numerator of Equation (5-11c), the complex step method has no truncation error associated with its definition, allowing as to use as small step size as possible.

Pérez-Foguet et al. (2000) present a review of these numerical methods and optimal step size applied to the context of plasticity, including a discussion on error analysis, which is outside the scope of this work. In what follows, we compare the analytical sensitivities with the numerical values for both the single and multi-material frameworks.

5.3.1 Validation: Single-Material Framework

The sensitivity of the single-material framework requires only the derivatives with respect with the element densities ρ presented in Appendix A.2. To validate them, consider the 2×2 grid shown in Figure 5.3a with a random density distribution, where we place a single unit cell per finite element. The magnitude of the nonzero boundary conditions has magnitude 1 mm on nodes 7 and 8, and the force boundary condition on node 9 has magnitude 1 N.

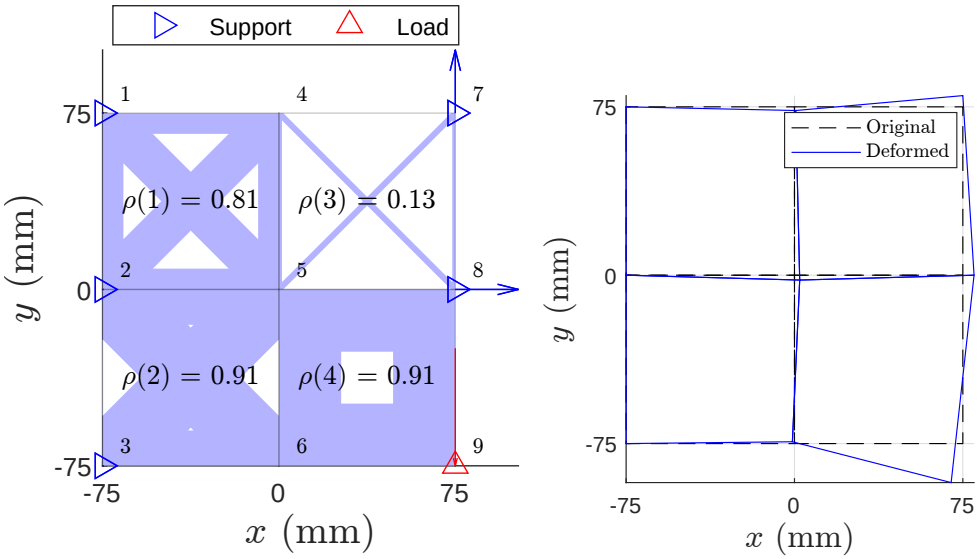

(a) Finite element mesh.

(b) Deformed structure (displacement scaling factor: 5x).

Figure 5.3: Problem domain used to validate the sensitivity analysis of the multi-material framework.

We selected the all degrees of nodes 7 and 8 (see Figure 5.3a) to compute $\mathbf{f}_{\text{out}}$, and set the target force $\bar{\mathbf{f}}_{\text{out}}$ as 1.1 times the value obtained by solving the original problem. For a relatively large step size of $h = \Delta\rho = 0.01$, the analytical sensitivity closely matches the values obtained via numerical

methods, as shown in Table 5.2, using the relative error metric defined in Equation (5-10). Figure 5.4 illustrates how the relative error decreases as the step size is reduced, until it reaches a limit for the FFD and CFD methods due to round-off error accumulation. In contrast, the CSM error plateaus near machine precision, avoiding truncation error by design.

Table 5.2: Comparison of analytical and numerical $\partial \mathcal{F}/\partial \boldsymbol{\rho}$ for $h = 0.01$.

Element	**Analytical**	**FFD**	**CFD**	**CSM**
1	0.0155	0.0157	0.0155	0.0154
2	-0.0091	-0.0087	-0.0091	-0.0091
3	0.0317	0.0318	0.0317	0.0317
4	-0.0807	0.0762	-0.0806	-0.0808

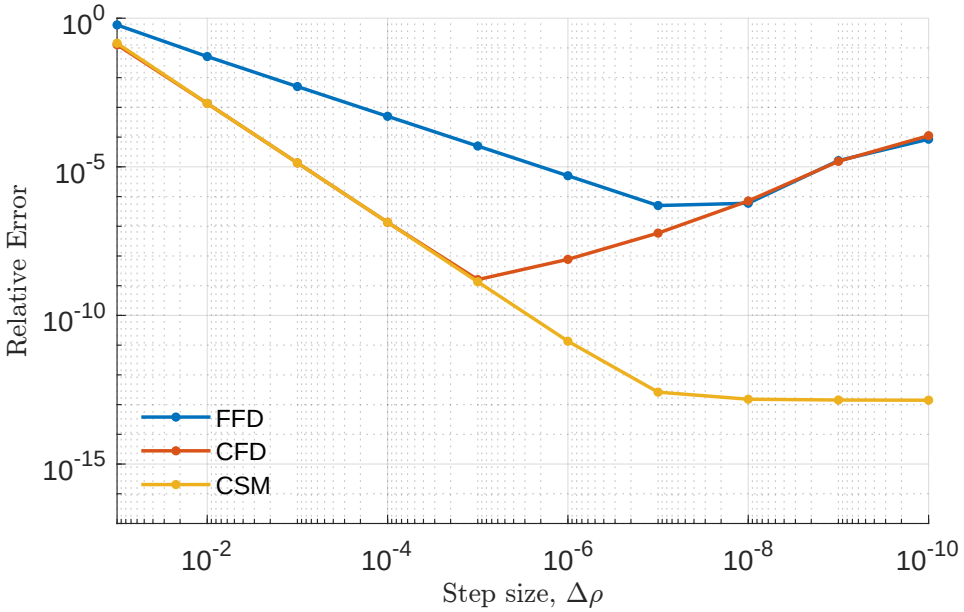

Figure 5.4: Relative error convergence of the objective function gradient with respect to the material densities in the single-material framework.

When considering the first five data points, FFD exhibits a lower convergence rate, consistent with its first-order accuracy, whereas CFD and CSM show nearly identical steeper slopes reflecting their second-order convergence behavior. The agreement between analytical and numerical sensitivities validates the sensitivity analysis.

5.3.2 Validation: Multi-Material Framework

The validation of the sensitivity analysis from Section 5.3.1 is repeated for the multi-material framework, with the difference that each element may

contain more than a single candidate material. We illustrate this by using the colormap shown in Figure 5.5, adapted from `PolyMat` by Sanders et al. (2018).

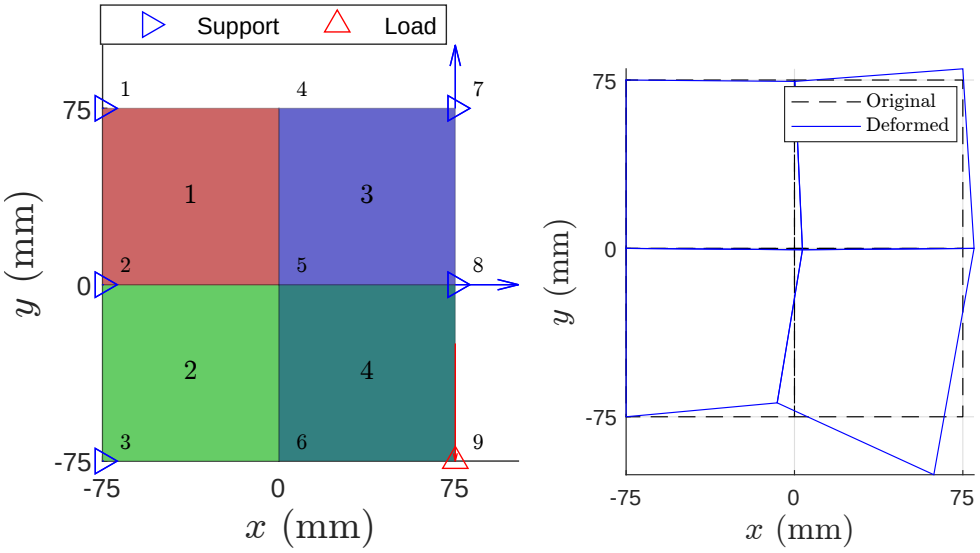

(a) Finite element mesh.

(b) Deformed structure (displacement scaling factor: 5x).

Figure 5.5: Problem domain used to validate the sensitivity analysis of the multi-material framework. Candidate materials are color-coded: (1) red, (2) green, and (3) blue.

Table 5.3: Material densities (ρ_i) and fractions (ξ_i) for the finite element mesh in Figure 5.5a.

Element	**Densities**			**Fractions**		
	ρ_1	ρ_2	ρ_3	ξ_1	ξ_2	ξ_3
1	0.8147	0.6324	0.9575	0.5000	0.1000	0.1000
2	0.9058	0.0975	0.9649	0.1000	0.5000	0.1000
3	0.1270	0.2785	0.1576	0.1000	0.1000	0.5000
4	0.9134	0.5469	0.9706	0.1000	0.4000	0.4000

Arbitrary values for the material densities and fractions were selected, as shown in Table 5.3, where indices 1–3 correspond to the candidate materials listed in Table 5.1. The sensitivity analysis derived in Appendix A.2 was implemented, where the relative error defined in Equation (5-10) was computed using the 2-norm of the column vectors containing all components of $\partial\mathcal{F}/\partial\rho_i$ and $\partial\mathcal{F}/\partial\xi_i$, treated separately. The numerical gradients of the objective function with respect to both ρ and ξ closely matched the analytical expressions, thereby validating the derivations.

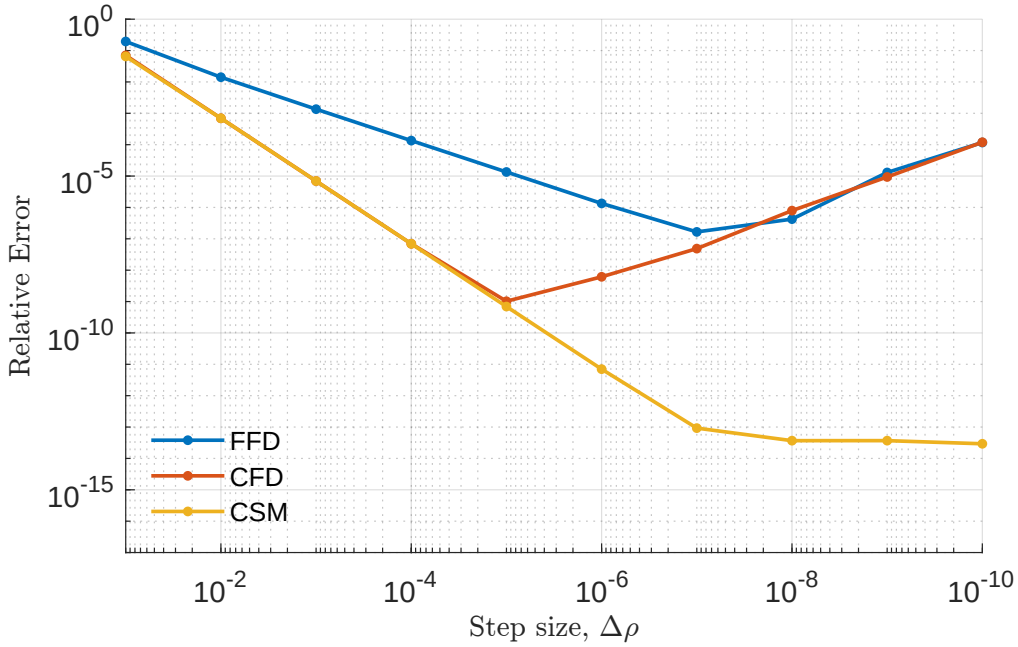

(a) Relative error in $\partial\mathcal{F}/\partial\boldsymbol{\rho}$.

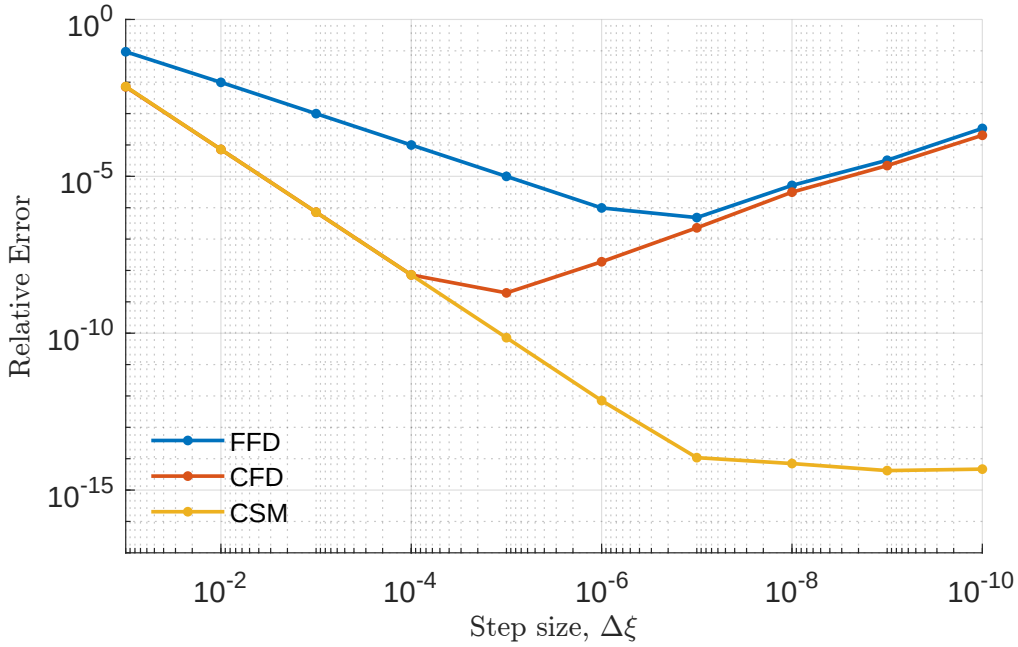

(b) Relative error in $\partial\mathcal{F}/\partial\boldsymbol{\xi}$.

Figure 5.6: Relative error convergence of the objective function gradient with respect to the material densities and fractions in the multi-material framework.

6
Results and Discussion

In this chapter, we present several results to both elastostatic cloaking and shape matching benchmark problems. Each problem was solved with a different strategy to display the different frameworks developed in our work. Unless otherwise stated, we utilized the modified version of the MMA algorithm detailed in Section 3.4 with the default parameters from Giraldo-Londoño and Paulino (2021), as it quickly converges to the solution of optimization problems without constraints (other than box constraints on the design variables), which are commonly found in target behavior problems.

The remainder of this chapter contains the results and discussion for the following problems:

- Elastostatic cloaking problems: We solve two cloaking benchmarks problems from the literature with the CBC paradigm.
- Shape matching of a beam under compression: In this example, we adapt our multiple metamaterial framework to the solution of a shape matching problem using the traditional (non-CBC) paradigm.

Elastostatic cloaking problems are solved with a multiple homogeneous candidate materials (using DMO), our multiple metamaterial framework (DCP), and our CBC-based microstructure design framework. A discussion is made in all sections evidencing the advantages and limitations of each method.

6.1
Example 1: Plate Under Horizontal Compression (DMO)

In this first example, we compare the traditional and CBC cloaking paradigms using the example of the plate under compression from Fachinotti et al. (2018). The reference and holed domain partitions, loads, and dimensions are shown in Figure 6.1.

Table 6.1: Base and candidate materials from Fachinotti et al. (2018).

Material	Young modulus, E (GPa)	Poisson's ratio, ν	Region
Nylon	6.0	0.40	Ω_{ref} and Ω_{sur}
Aluminum	69.0	0.32	Ω_{cloak}
PTFE	0.5	0.40	Ω_{cloak}

The original material of the plate is nylon, and the candidate materials for the cloaking device are aluminum and PTFE, with the properties shown

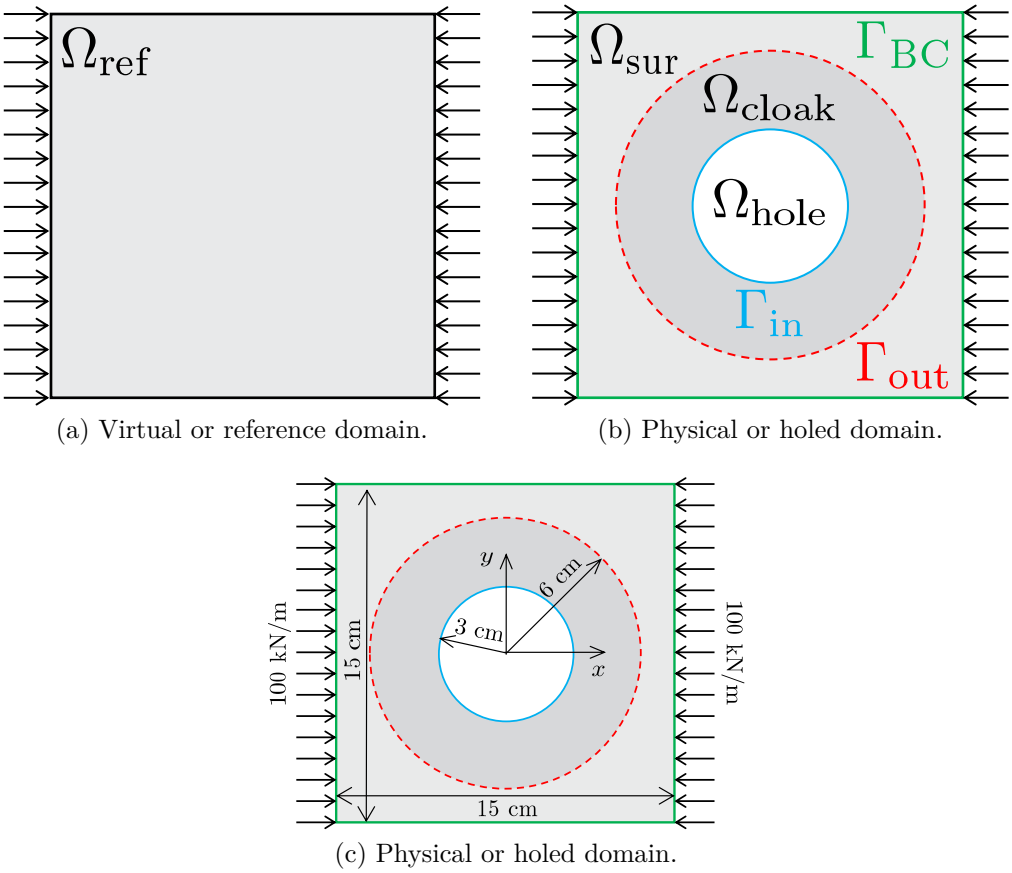

(a) Virtual or reference domain.

(b) Physical or holed domain.

(c) Physical or holed domain.

Figure 6.1: Plate under horizontal compression .

in Table 6.1. The candidate materials were selected using the DMO method, which follows exactly the same idea detailed in Section 5.2 when only the material fraction $\xi_m^{(e)}$ is associated with each candidate material. In other words, there is no density design variable $\rho_m^{(e)}$ when the candidate material is homogeneous, which we considered in this first example to enable comparison with the reference.

We will identify the different domains and boundary conditions related to this example according to Table 6.2. The finite element mesh and boundary conditions for each case are shown in Figure 6.2.

For this example, we utilize a set of techniques to avoid well-known problems in density-based topology optimization. First, we adopt the filtering technique inspired by Bruns and Tortorelli (2001) to remove checkerboard patterns in the optimized design. The filtered variable of an element is given by

$$y_m^{(e)} = \frac{\sum_{i=1}^{N} w_{e,i} z_m^{(e)}}{\sum_{i=1}^{N} w_{e,i}}, \tag{6-1}$$

where

$$w_{e,i} = \max\left(1 - \frac{d_{e,i}}{r_{\text{filter}}}, 0\right)^q \tag{6-2}$$

can be interpreted as a weight function that averages each element's design

Table 6.2: Finite element analysis domains used in the plate with elastostatic cloaking.

Case	Domain	Boundary Conditions	Domain type
1	Ω_{ref}	150 kN/m distributed load	Reference domain
2	$\Omega_{\text{cloak}} \cup \Omega_{\text{sur}}$	Same as Case 1; $\mathbf{f}_{\text{in}} = \mathbf{0}$ at Γ_{in}	Uncloaked holed domain
3	Ω_{cloak}	$\mathbf{u}_{\text{out}} = \overline{\mathbf{u}}_{\text{out}}$; $\mathbf{f}_{\text{in}} = \mathbf{0}$ at Γ_{in}	Optimization domain
4a	$\Omega_{\text{cloak}} \cup \Omega_{\text{sur}}$	Same as Case 2	Optimized domain (w/ gray zones)
4b	$\Omega_{\text{cloak}} \cup \Omega_{\text{sur}}$	Same as Case 2	Optimized domain (w/o gray zones)

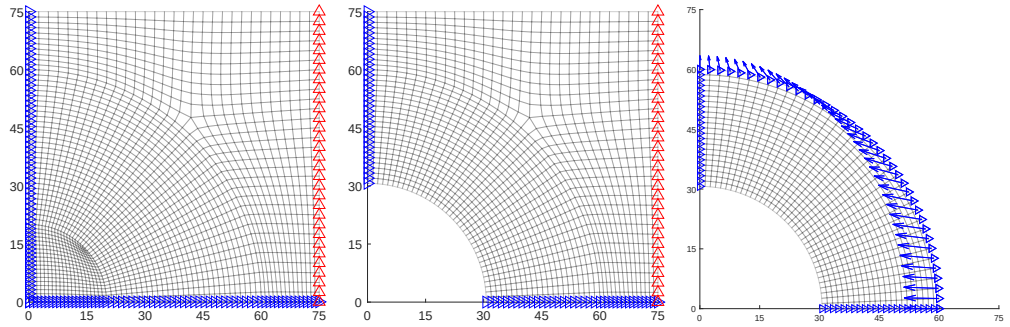

(a) Case 1: 8344 Q4 elements. (b) Case 2, 4a, and 4b: 5644 Q4 elements. (c) Case 3: 3256 Q4 elements.

Figure 6.2: Unstructured finite element mesh (top-right quadrant) and boundary conditions for each case. Blue and red triangles on nodes represent prescribed displacement and load boundary conditions, respectively.

variable with those within radius r_{filter}, weighted by the variable $w_{e,i}$ which is a function of the Euclidean norm $d_{e,i}$ between the centroids of elements e and i. The exponent q can be set to one, yielding a linear hat kernel when interpreting the filter as a convolution of the design variables.

Next, we reduce the gray zones introduced in the filtering step by introducing a smooth-Heaviside threshold projection (Wang et al., 2011) in the form

$$\xi_m^{(e)} = \frac{\tanh(\beta\eta) + \tanh\left(\beta\left(y_m^{(e)} - \eta\right)\right)}{\tanh(\beta\eta) + \tanh(\beta(1-\eta))}, \tag{6-3}$$

with sharpness parameter β and threshold parameter η. The material fraction variable $\xi_m^{(e)}$ is used in the DMO formulation in Equation (5-5). The derivatives of Equations (6-2) and (6-3) required for the sensitivity analysis are straightforward and take the form

$$\frac{\partial y_m^{(i)}}{\partial z_m^{(e)}} = \frac{w_{e,i}}{\sum_{e=1}^{N_e} w_{e,i}}, \tag{6-4a}$$

$$\frac{\partial \xi_m^{(i)}}{\partial y_m^{(i)}} = \frac{\beta[1 - \tanh\left(\beta\left(y_m^{(i)} - \eta\right)\right)]^2}{\tanh(\beta\eta) + \tanh(\beta(1-\eta))}. \tag{6-4b}$$

In our implementation, we adopted a continuation scheme to reduce numerical problems, so β starts at an initial value β_{ini} and increases by 1 every β_{frq} iterations of the optimization algorithm up to a maximum value $\beta_{\max}$. The optimization parameters are shown in Table 6.3. We averaged the values of the design variables $z_m^{(e)}$ over all four symmetric elements at the end of each optimization iteration to ensure a symmetric design. Loss of symmetry occurs when small numerical differences accumulated throughout early iterations are exacerbated at the end of the optimization process. Additionally, we avoid setting high values of β and p, as they can yield voids ($\phi_m \approx 0$ for all candidates simultaneously) due to the excessive penalization.

Table 6.3: Optimization parameters for the plate with hole example.

Parameter	**Value**	**Notes**
Initial guess, $\boldsymbol{z}^{(e)}$	$\begin{bmatrix}0.1 & 0.1\end{bmatrix}$	Same initial value for all elements
Maximum MMA interations	1000	Stopping criterion
Filter radius, r_{filter}	12 mm	-
Filter exponent, q	1.0	Linear hat kernel
Sharpness parameter, β_{ini}	1	Initial value
Sharpness parameter, $\beta_{\max}$	15	Maximum value
Sharpness parameter, β_{frq}	10	Update frequency
Threshold parameter, η	0.5	This parameter is not updated
Penalization parameter, p	2.0	This parameter is not updated
DMO parameter, γ	1.0	This parameter is not updated

The current and target nodal force vectors on Γ_{out} are displayed in real time during the optimization process, as shown in Figure 6.3. Together with the normalized objective function graph in Figure 6.4, this provides both a qualitative and quantitative measure of the difference between the current and target physical behavior on the cloak-surrounding interface. It is clear that, while the objective function was minimized by several orders of magnitude, the MMA algorithm presented did not clearly converge to an optimum due to the complexity of this problem, so the optimization was ended using a stopping criterion. The globally-convergent version of the MMA (Svanberg, 2007) could be used in future works to stabilize the convergence process.

The topologies and displacement field for different cases are presented in Table 6.4, where it can be seen that the original displacement field is recovered with the introduction of the cloaking device. To get the design in case 4b, we applied the same a posteriori "black-and-white" filter from Fachinotti et al. (2018) by assigning the stiffer material properties of the aluminum material to all elements with $\phi_1^{(e)} \geq \phi^*$, where the subscript denotes the stiffer candidate

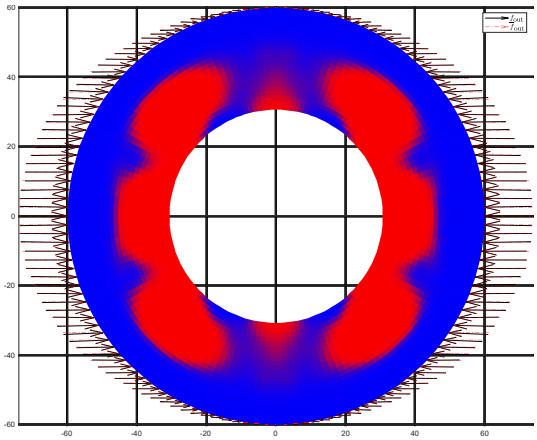

Figure 6.3: Optimized cloak design with current (black arrows) and target (red arrows) nodal force vectors.

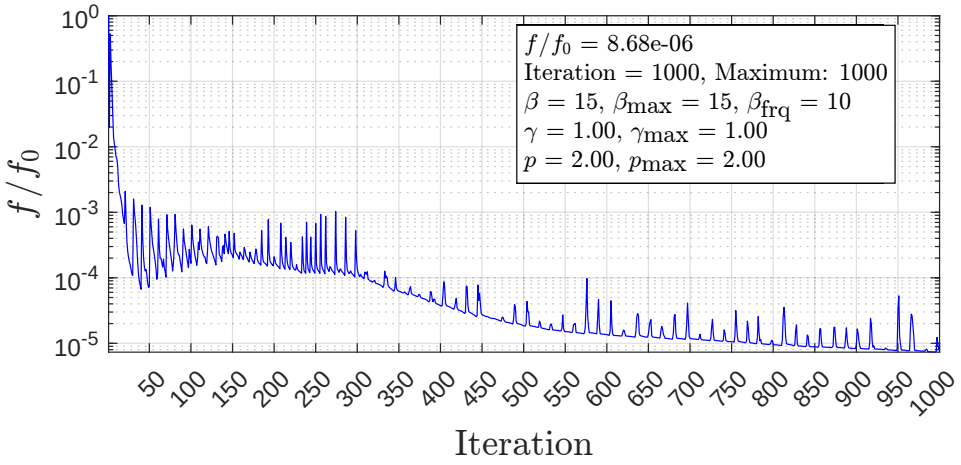

Figure 6.4: Normalized objective function evolution graph for the plate with hole example with unstructured mesh.

material (aluminum). Hereafter, we denote the normalized weight $\overline{w}_m^{(e)}$ with the symbol $\phi_m^{(e)}$ as done by the reference (Fachinotti et al., 2018) for clarity. We chose $\phi^* = 0.013$ which yielded the best cloaking performance and a concentric design with the stiffer material surrounding most of the hole, and the softer material interfacing the surrounding region. This specific value was the lowest obtained for the RMSE and Δ metrics as shown in Figure 6.5. The displacement fields of the optimized design in case 4a closely matches the reference's (case 1), but after applying the black-and-white filter some of the cloaking perfomance is lost, though its cloaking performance is still far superior to the uncloacked plate in case 2.

To show how this approach gives insight in the root cause of the mechanical cloaking problem, see the nodal forces distribution along the outer boundary in Figure 6.6. Their horizontal pattern is lost upon the introduction of the hole, and recovered with the cloaking device. Though some of the

Table 6.4: Plate topology, and horizontal (u_x) and vertical (u_y) displacement fields for the unstructured mesh. Materials are nylon (gray), aluminum (red), and PTFE (blue).

Case	Design	u_x (mm)	u_y (mm)
1		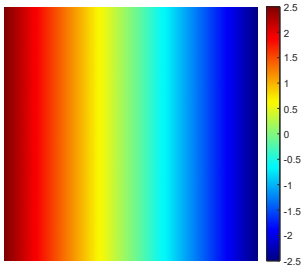	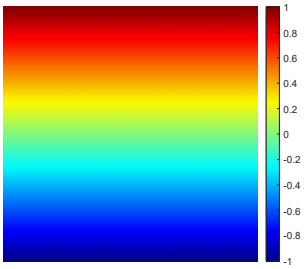
2		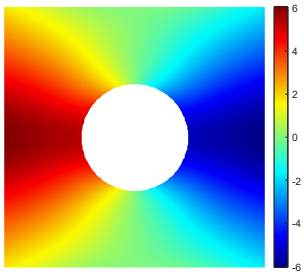	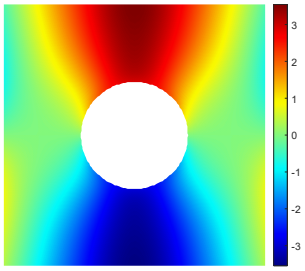
4a	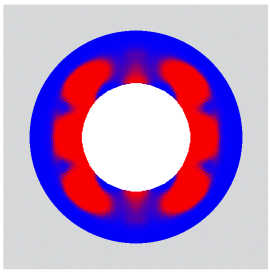	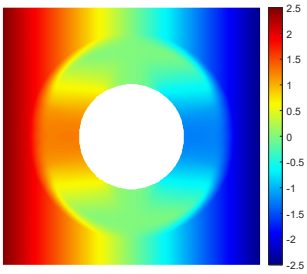	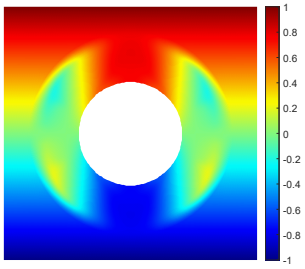
4b	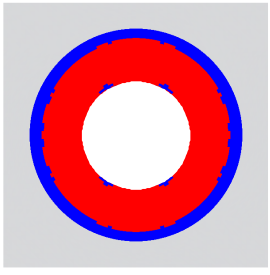	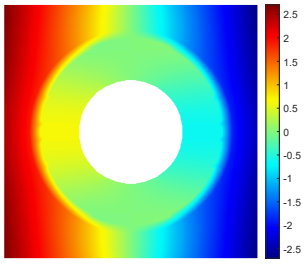	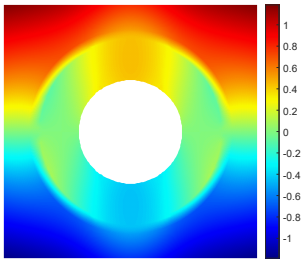

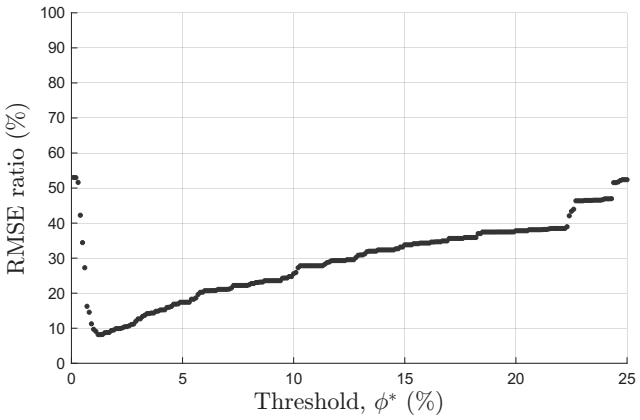

(a) RMSE

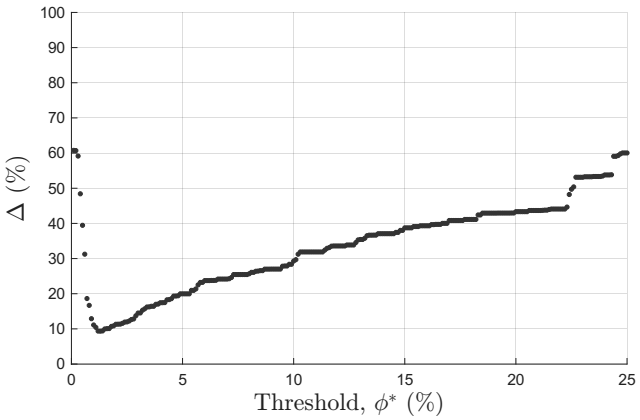

(b) Δ

Figure 6.5: Influence of the pseudo-density threshold on displacement error metrics.

horizontal pattern is lost after the "black-and-white" filter in Figure 6.6d, even roughly approximating the reference's nodal forces on the boundary significantly improves cloaking performance. For this reason, enforcing a compatible boundary condition leads to the cloaking effect, as proposed by Cheng et al. (2023).

Although the perimeter of the circular boundaries Γ_{in} and Γ_{out} cannot be perfectly approximated by a structured square grid, we repeat the mechanical cloaking with the structured mesh shown in Figure 6.7 to compare with Fachinotti et al. (2018).

For the structured mesh optimization, we used the same optimization parameters from Table 6.3, except for the following: $r_{\text{filter}} = 6$ mm, $\beta_{\max} = 10$, and $p = 3$. The optimized designs and displacement fields for the structured mesh are shown in Table 6.5.

Since the objective function in Equation (4-11a) does not directly measure the cloaking performance, we choose suitable metrics from Table 4.1 to quantify the cloaking performance. We adopt the root mean square error of

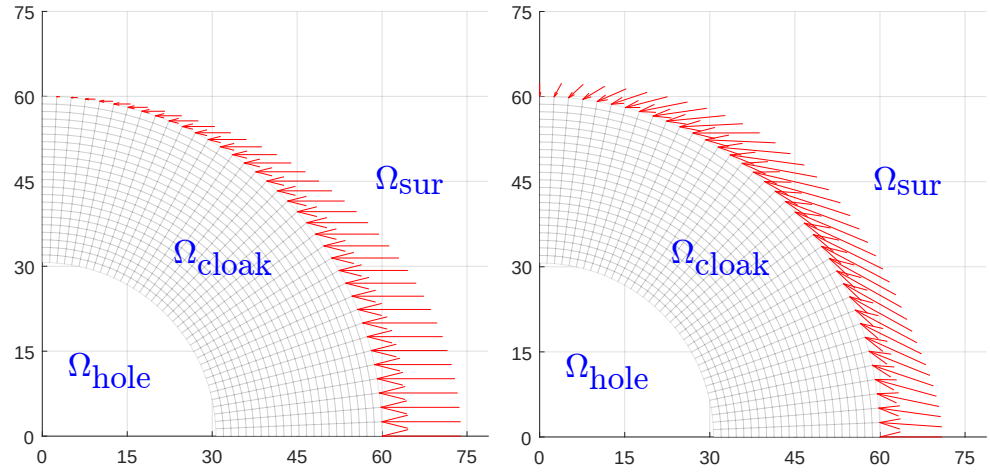

(a) Case 1: Original domain.

(b) Case 2: Uncloaked domain.

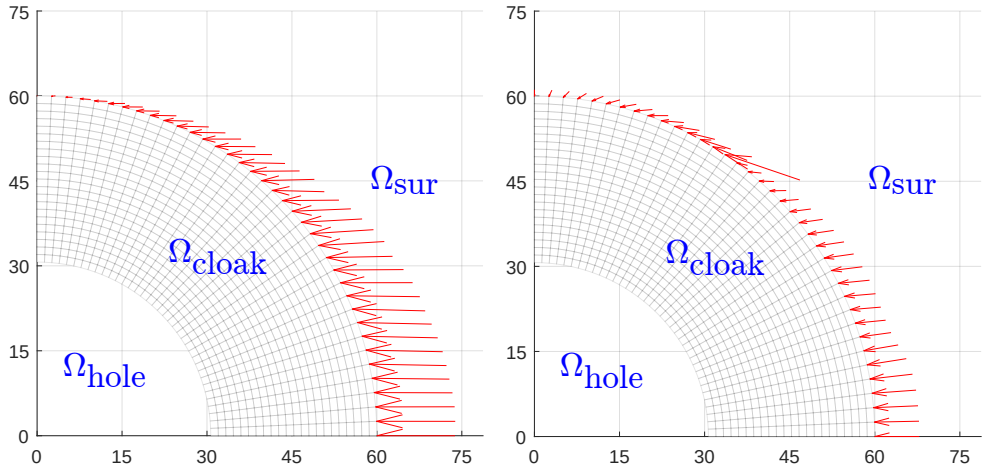

(c) Case 4a: Cloaked domain (with gray zones).

(d) Case 4b: Cloaked domain (without gray zones).

Figure 6.6: Nodal forces $\mathbf{f}_{out}$ on the outer boundary for each case. Dimensions in milimeters.

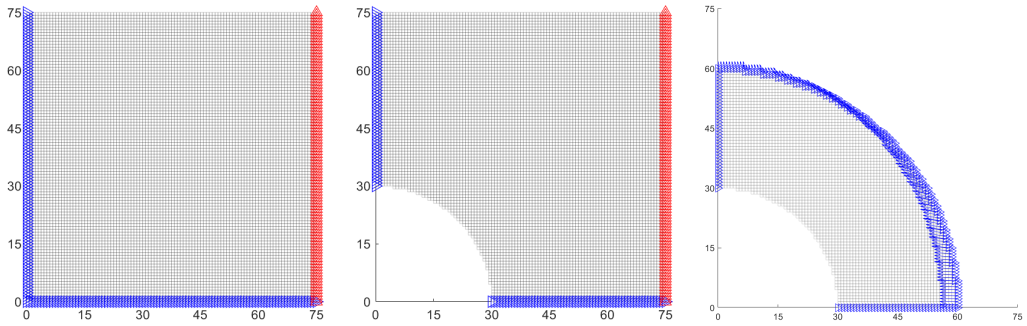

(a) Case 1: 40000 Q4 elements.

(b) Case 2, 4a, and 4b: 34976 Q4 elements.

(c) Case 3: 15084 Q4 elements.

Figure 6.7: Structured finite element mesh (top-right quadrant) and boundary conditions for each case. Blue and red triangles on nodes represent prescribed displacement and load boundary conditions, respectively.

Table 6.5: Plate topology, and horizontal (u_x) and vertical (u_y) displacement fields for the structured mesh. Materials are nylon (gray), aluminum (red), and PTFE (blue).

Case	Design	u_x (mm)	u_y (mm)
1		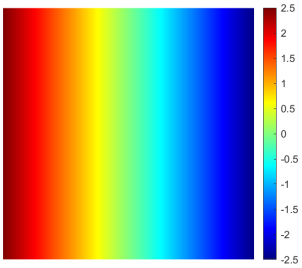	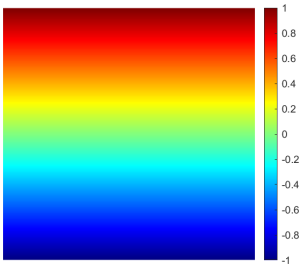
2		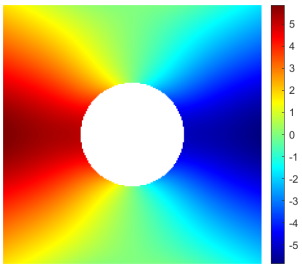	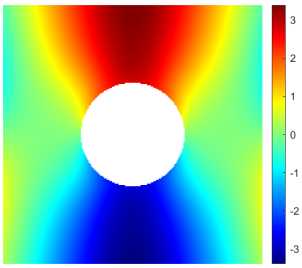
4a	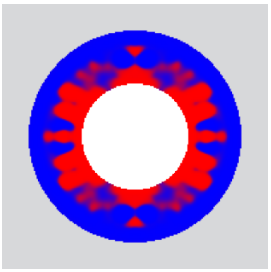	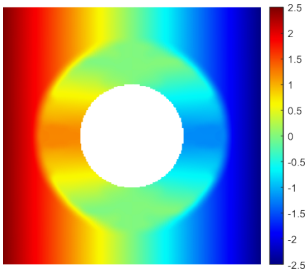	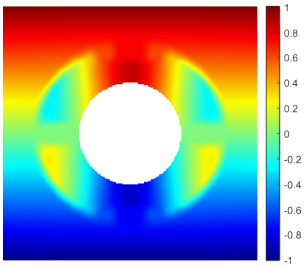
4b	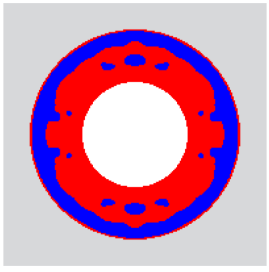	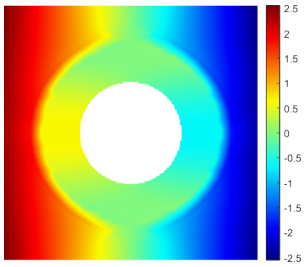	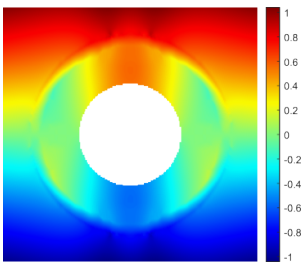

the nodal displacements over the N_{check} degrees of freedom in Ω_{sur}, and the normalized metric Δ (Bückmann et al., 2015). These metrics measured for Ω_{sur} take the form

$$\text{RMSE} = \sqrt{\frac{1}{N_{\text{check}}} \sum_{i=1}^{N_{\text{check}}} \|\mathbf{u} - \mathbf{u}_0\|^2}, \tag{6-5}$$

$$\Delta = \frac{\sqrt{\sum_{i=1}^{N_{\text{check}}} \|\mathbf{u} - \mathbf{u}_0\|^2}}{\sqrt{\sum_{i=1}^{N_{\text{check}}} \|\mathbf{u}_0\|^2}}, \tag{6-6}$$

where $\mathbf{u}$ and $\mathbf{u}_0$ are the nodal displacement of the optimized and reference structures, respectively.

We compare several analysis and optimization metrics in Table 6.6, where it is shown that our results yield similar or better performance compared to the reference at a much lower computational cost both in the finite element analysis (FEA) and during the optimization. We remark that while the theoretical cloaking performance with gray zones is impressive, the error metrics significantly increase when they are removed, most notably for the unstructured mesh. Further drop in performance is expected for the fabricated structure, depending on the manufacturing process.

Table 6.6: Analysis and optimization metrics for the elastostatic cloaking of a plate with hole example. Comparison between this work and the reference (Fachinotti et al., 2018).

Parameter	**This work**		**Reference**
	Unstructured	**Structured**	**Structured**
Elements in the original domain	8344	40000	40000
Elements in the uncloaked domain	5644	34976	34976
DOFs in FEA during optimization	6808	31128	71072
DOFs in objective function, N_{check}	148	640	19972
Design variables in optimization, N_{var}	6512	30168	30168
Norm of $\|\boldsymbol{u}_0\|$(original domain)	2.693 mm	2.693 mm	2.693 mm
RMSE/ $\|\boldsymbol{u}_0\|$ (uncloaked)	82.6 %	68.5 %	-
Optimal material fraction threshold, ϕ^*	0.013	0.018	0.015
$\text{RMSE}_{\text{cloaked}}/\text{RMSE}_{\text{uncloaked}}$ (w/ gray zones)	0.053 %	0.303 %	0.417 %
$\text{RMSE}_{\text{cloaked}}/\text{RMSE}_{\text{uncloaked}}$ (w/o gray zones)	8.165 %	2.963 %	6.10 %
Δ (with gray zones)	0.06 %	0.29 %	0.40 %
Δ (without gray zones)	9.36 %	2.83 %	8.56 % *

* Value for a simplified version of the cloaking device reported by the authors.

Lastly, we notice that adjusting the optimization parameters can yield potentially better results, but it may also introduce undesirable geometric artifacts that are difficult to manufacture. For instance, setting $p = 3$ and $\phi^* = 0.012$ while keeping the other parameters the same as in Table 6.3 yields the cloak design in Figure 6.8. Though it has better theoretical cloaking performance after removing the gray zones ($\text{RMSE}_{\text{cloaked}}/\text{RMSE}_{\text{uncloaked}} =$

7.31% and $\Delta = 8.38\%$) compared to that in Table 6.4, it is also more complex to fabricate than the one in Table 6.4.

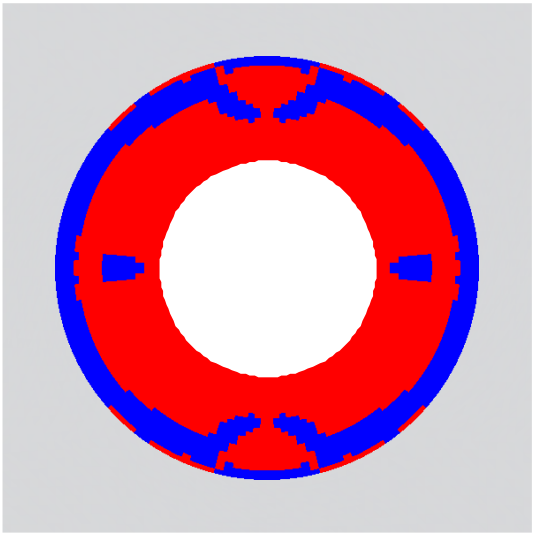

Figure 6.8: Filtered optimized design of the unstructured mesh for $p = 3$ and $\phi^* = 0.012$. Materials are nylon (gray), aluminum (red), and PTFE (blue).

6.2 Example 2: Plate Under Displacement-Free BC (Multi-Material Framework)

The next example analyzed in this chapter is that of a plate under uniform horizontal displacement boundary condition along its edges, proposed by Wang et al. (2022). The domain also consists of a 150 mm × 150 mm plate subjected to horizontal compression by imposing a uniform displacement boundary condition alongside the edges with magnitude $u_{bc} = 0.5$ mm. Figure 6.9a shows the problem domain including the additional roller supports added to the horizontal and vertical axes, to ensure a symmetric response and avoid numerical problems (as no vertical degree of freedom had yet been prescribed). The plate was discretized into 30 × 30 Q4 elements each representing a single four-rod cubic lattice unit cells, as shown in Figure 6.9b.

Table 6.7 presents the problem parameters adopted in this example, where we use the homogenized properties of the unit cell discretized into 50×50 Q4 elements. We remark that this discretization may be considered rather coarse to realize all details of the unit cell, but we adopt the same values as the reference (Wang et al., 2022) to enable comparison.

The reference domain shown in Figure 6.9a is partitioned into the hole, cloak and surrounding regions. Several examples in the literature adopt a 2/1 ratio between the outer and inner radius of the cloaking device (Bückmann et al., 2015; Fachinotti et al., 2018). The N_{check} nodes in the surrounding re-

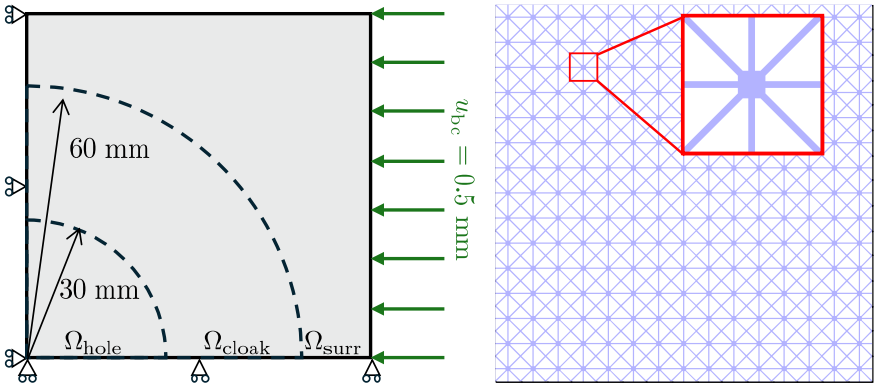

(a) Problem domain. (b) Problem domain.

Figure 6.9: Plate under displacement-free boundary condition (top-right quadrant only) meshed into 30×30 four-rod cubic lattice unit cells. Adapted from Wang et al. (2022).

Table 6.7: Problem parameters for the cloaking of a plate under displacement-free boundary condition.

Parameter	**Value**
Mesh size	30×30 unit cells
Unit cell size	5 mm $\times$ 5 mm
Young's modulus	$E = 1.20$ GPa
Poisson's ratio	$\nu = 0.35$
Homogenized properties (four-rod cubic lattice)	$\mathbf{C}^H = \begin{bmatrix} 171.55 & 69.68 & 0 \\ 69.68 & 171.5 & 0 \\ 0 & 0 & 62.07 \end{bmatrix}$ MPa
Unit cell mesh	50×50
Element type	Plane stress Q4 element
Imposed displacement	$u_x = 0.5$ mm

gion are checked for the cloaking performance metrics. Once elements whose centroid fall withing Ω_{hole} are removed, the error in displacement field yields and error $\Delta = 16.985\%$ and RMSE/ $\|\mathbf{u}_0\|_2$=12.112, where $\|\mathbf{u}_0\|_2 = 0.5397$ mm is the Euclidian norm of the displacement vector of the original structure. While we use nodal forces in our objective function, the displacement-based error metrics from Table 4.1 allows us to effectively measure cloaking performance and compare our results with the literature.

Our objective in this section is to design the cloaking device using the multi-material frameworks presented in Chapter 5. The optimization domain consists of the elements whose centroid fall in Ω_{cloak} with the displacement of the reference domain along the outer boundary Γ_{out} imposed as a natural boundary condition, as shown in Figure 6.10a. The material 1 from Table 5.1 is initially adopted as the single candidate material to present the optimization

framework, where we chose $\rho_{\min} = 0.1$ and $\rho_{\max} = 0.9$ as arbitrary bounds for the design variable, representing manufacturing limitations. The solid constituent material used in the cloaking device has the same properties as the base unit cell, except for the Poisson modulus that is set to $\nu = 0.3$

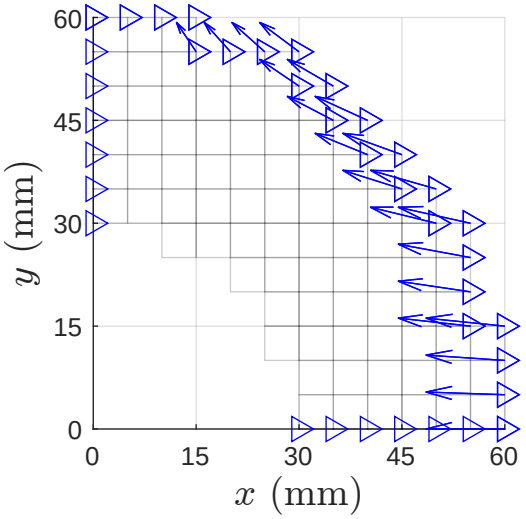

(a) Displacement boundary conditions.

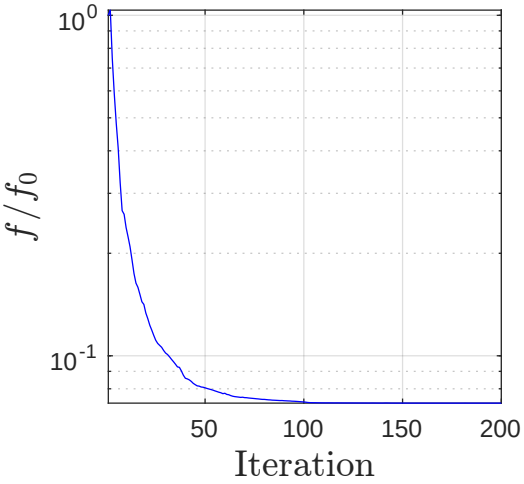

(b) Normalized objective function.

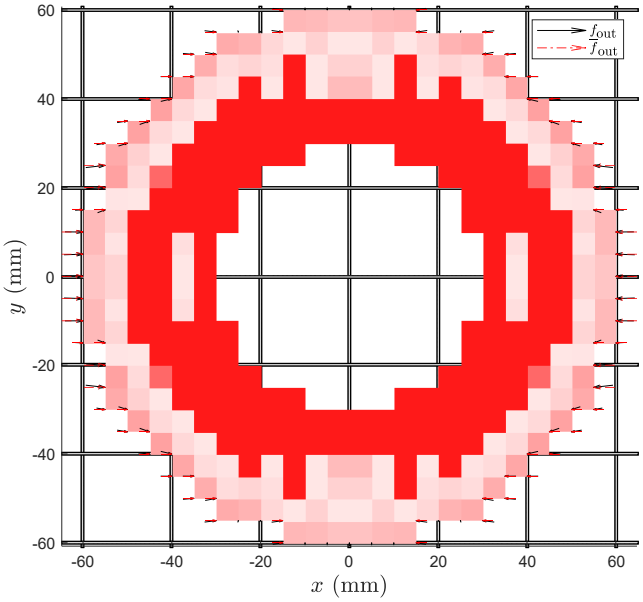

(c) Density distribution.

Figure 6.10: Single-material topology optimization of the plate under displacement-free boundary conditions and using material 1.

The optimization algorithm is run for 200 iterations (the stopping criterion) with the normalized objective function quickly dropping within the first 100, as shown in Figure 6.10b. We averaged the densities of symmetric elements at the end of each MMA iteration to enforce a symmetric design, which is shown in Figure 6.10c, where we notice that the densities shown in a color scale are higher around the hole, but softer near the interface with

the surrounding region. Even though the nodal forces $\mathbf{f}_{\text{out}}$ do not approach the target $\overline{\mathbf{f}}_{\text{out}}$ perfectly, the RMSE reduces to 34.9 % of its uncloaked counterpart, and Δ drops to 5.92. This clearly shows how addressing the root cause of the cloaking problem (i.e., the interactions at the cloak-surrounding interface) is an effective tool to solve the mechanical cloaking problem.

The topology optimization was executed with the truss-like materials 1-3 from Table 5.1 using the same optimization parameters. Figure 6.11 shows that the reference displacement field is mostly recovered in the surrounding region for the cloaked structures.

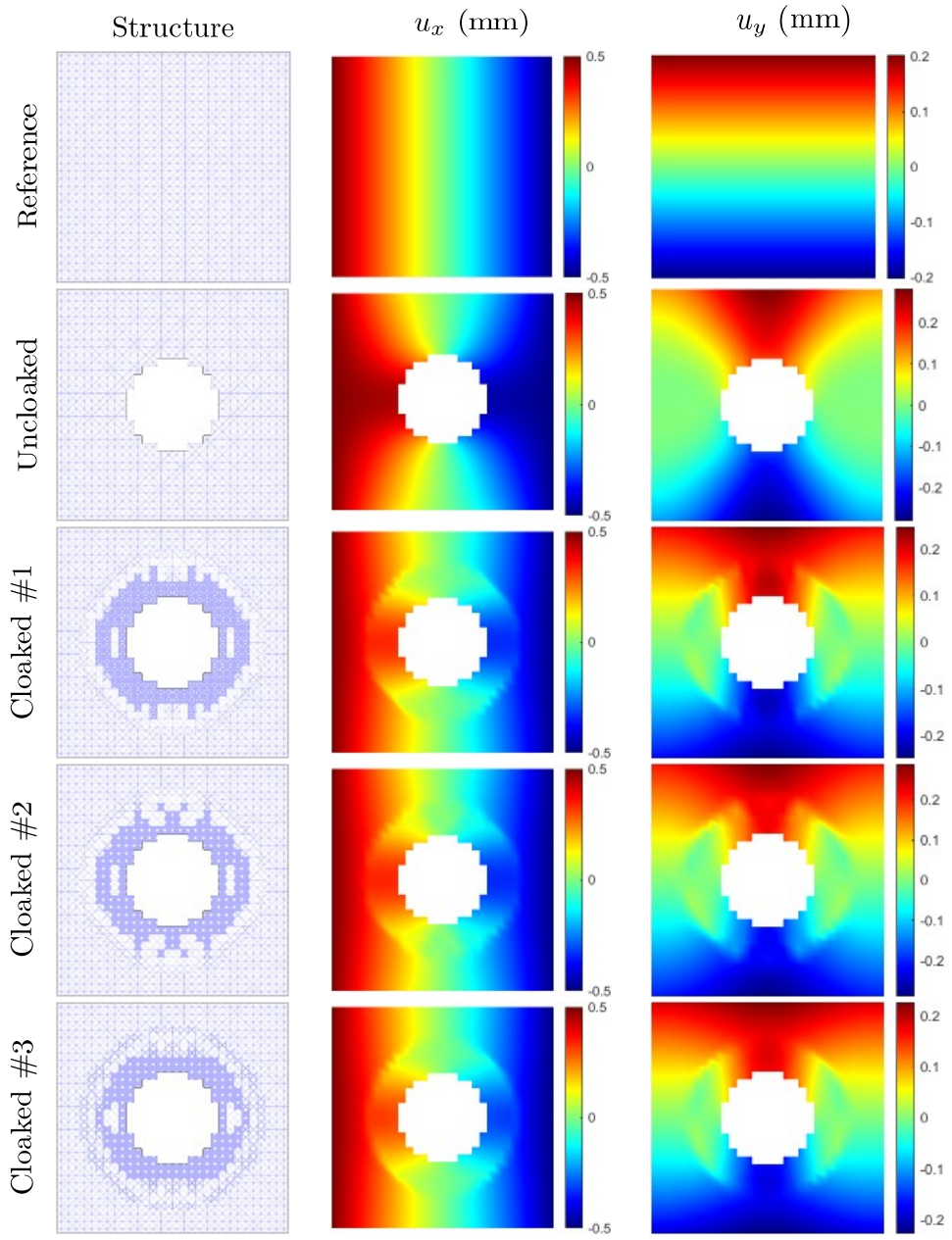

Figure 6.11: Structure and displacement fields of the reference, uncloaked and cloaked structures using candidate materials 1-3, one at a time.

The same problem is now solved using the multi-material selection framework with materials 1, 2 and 3 as candidates. The same optimization algorithm and parameters are repeated here, with the bound of the design variables set to $z_{\min} = 0.1$ and $z_{\max} = 0.9$. The initial guess z_{ini} for the material selection process is $\rho_m^{(e)} = \xi_m^{(e)} = 0.2 \; \forall e = 1, \ldots, N_e$ and $m = 1, 2, 3$. After 200 MMA iterations, we eliminate all candidates for each element, except that with the highest $\xi_m^{(e)}$. Finally, we run the single-material TO with optimal material candidate choice and density.

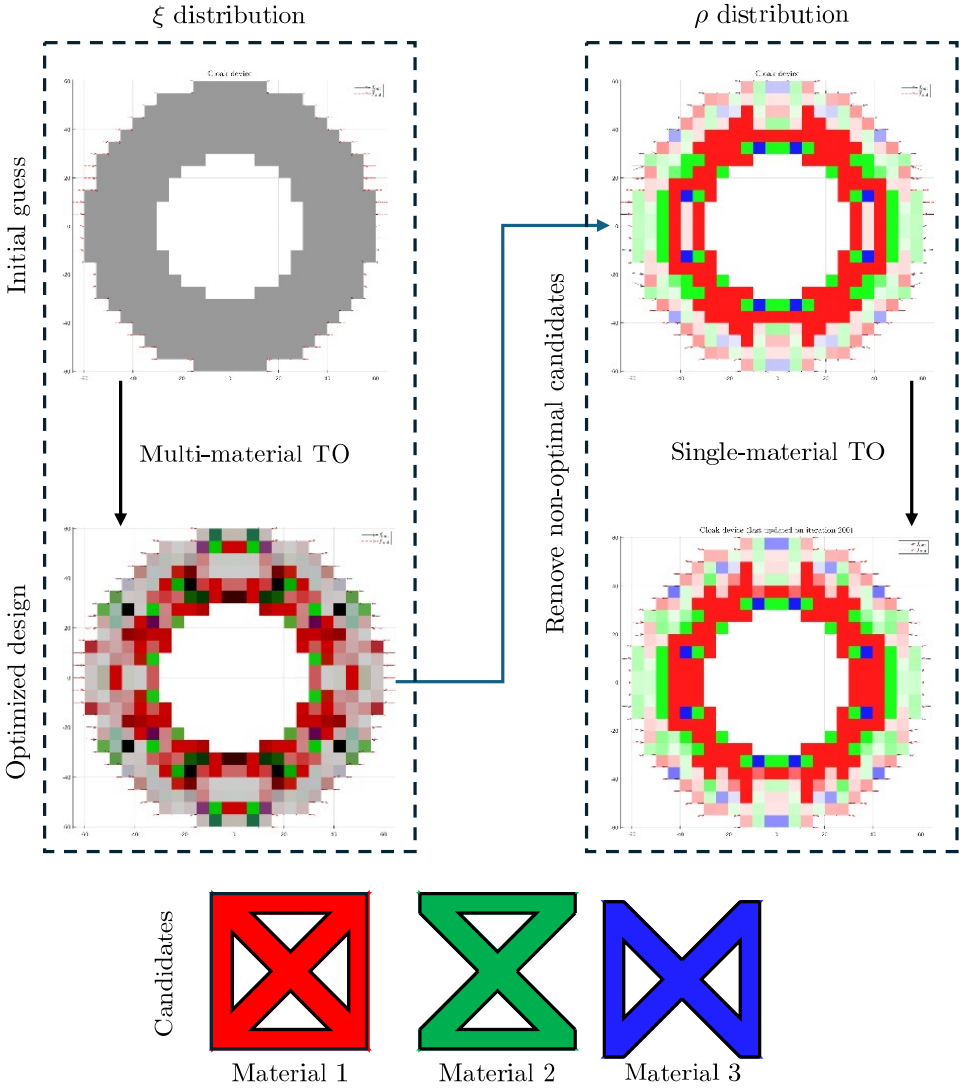

Figure 6.12: Flowchart of the integrated multi and single candidate material TO frameworks. The material fraction $\xi_m^{(e)}$ distritibution is shown on the graphs on the left-hand side, and the density $\rho^{(e)}$ is shown on the right-hand side, with candidates color coded as shown at the bottom of the figure.

Figure 6.12 shows that the material selection algorithm distributes mostly the stiffer material 1 immediately around the hole, in order to reinforce it. The color distribution is adapted from the existing multi-material TO literature (Sanders et al., 2018), displaying a white element when all $\xi_m^{(e)}$ are low and

brown or black when more than one candidate has high enough ξ. It is evident that the elements closer to Γ_{out} have a ligher color indicating that no material is selected. This occurs because the version DCP penalizes the stifness when more than a single candidate is chosen, which does negatively affect the objective in compliance minimization, but not necessarily so in mechanical cloaking. This occurs because it is beneficial to lay out less stiff material around the outer boundary to recover the original displacement field in this benchmark example, the same result shown in Figure 6.11 and found previously in the literature (Fachinotti et al., 2018).

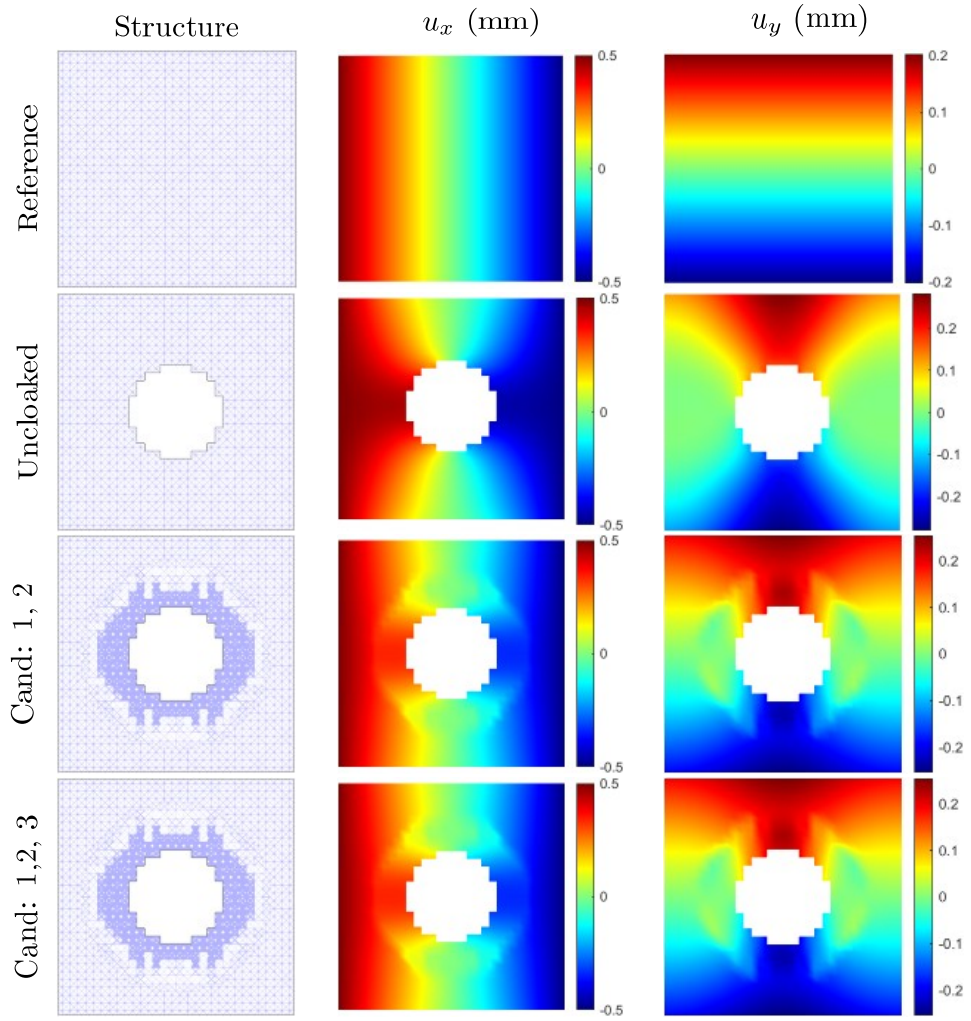

Figure 6.13: Structure and displacement fields of the reference, uncloaked and cloaked structures using candidate materials 1-3 with the DCP material selection algorithm.

The optimized structures in Figure 6.13 shows that, while the original displacement field is partially recovered in the surrounding region, the lattices change sharply from high to low density as one moves from the inner to the outer boundary. We also ran another optimization using only candidate materials 1 and 2, where we found best results using the initial guess $z_{\text{ini}} = 0.9$

instead. This may negatively affect cloaking performance in experimental validations, alongside the fact that no compatibility formulation has been adopted. A filter and compatibility formulation (e.g. connectivity index from Du et al. (2018)) may be introduced in future works to address these issues. Despite these challenges, for a reasonably low number of candidate materials, this method has been shown to efficiently cloak the impact of introducing the hole in the original structure.

Table 6.8: Relative RMSE and Δ for structures uncloaked and cloaked with candidate materials 1, 2 and 3.

Candidates	$\text{RMSE}/\text{RMSE}_{\text{uncloaked}}$ (%)	Δ (%)
Uncloaked	-	16.175
Only 1	34.85	5.920
Only 2	57.04	9.687
Only 3	25.46	4.327
1 and 2	34.20	5.53
1, 2 and 3	29.45	4.76

Lastly, we analyze the error metrics from the previous optimizations in Table 6.8, where it is clear that the vertical trusses of candidate material 3 seem to be the best choice for this problem. Moreover, using two candidates 1 and 2 simultaneously yield a better result than using them individually. However, it was better to use only material 3 than all of the candidates (due to the lower normalized RMSE), which can be explained due to the material selection algorithm being originally designed for compliance minimization problems. Though we have shown that it may be used as is in mechanical cloaking problems, it would be better to adapt it to have the material fractions $\boldsymbol{\xi}$ in the objective function itself or be added to a suitable constraint function instead.

6.3 Example 3: Beam Under Compression Shape Matching (DMO)

Consider a beam meshed into 30×4 elements and subject to a uniform prescribed prescribed displacement of magnitude $u_0 = 0.6$ mm. The amplitude of the target sine wave is 0.2 mm, amplified 50 times in for readability. Only the vertical displacement of the centerline nodes is considered as a target displacement field.

For this target shape problem inspired by Chan et al. (2022), we will adopt a traditional objective function (instead of that from the CBC paradigm) as there are few arbitrarily-chosen nodes whose degree of freedom must approximate a target. The objective function takes the form of a weighted

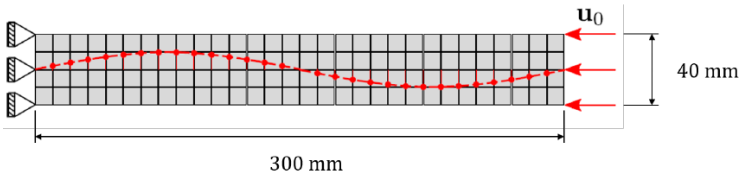

Figure 6.14: Target sine wave problem: domain, mesh, and dimensions (Chan et al., 2022).

norm of the displacement field:

$$\mathcal{F} = (\Delta \mathbf{u}^*)^T \mathbf{W} (\Delta \mathbf{u}^*), \tag{6-7}$$

where $\Delta \mathbf{u}^* = \mathbf{u}^* - \overline{\mathbf{u}}^*$ is the error between the current ($\mathbf{u}^*$) and target ($\overline{\mathbf{u}}^*$) nodal displacements of chosen degrees of freedom denoted by the asterisk, and $\mathbf{W}$. For this example, we set the weight matrix as the identity, so the objective function is the square of the norm of the displacement error. The sensitivity analysis of Equation (6-7) is detailed in Appendix A.3.

We seek to find the best metamaterial and density distribution in the elements, assuming that the solid material has Young modulus $E = 1$ GPa, and Poisson ratio $\nu = 0.3$, under plane stress condition, with thickness equal to 10 mm. Minimum, maximum, and initial density values were arbitrarily set to $\rho_{\text{min}} = 0.2$, $\rho_{\text{max}} = 0.8$, and $\rho_{\text{ini}} = 0.5$, respectively.

For this example, we ran every instance of optimization with MATLAB's built-in `fmincon` function, using the SQP algorithm up to 1000 objective function evaluations, and with default tolerances (10^{-6}), except for the optimality tolerance, which was increased to 10^{-4}.

In the results presented here, we adopted the following color code: red, green, and blue represent candidates 1, 2, and 3 from Table 5.1, respectively. We repeated a similar process to that from Section 6.2, that is, we ran the optimization first using one candidate metamaterial as a single candidate, and compared to the solution with multiple metamaterials. The following parameters were utilized for the multiple-candidate two-step approach:

1. First we optimized with all three candidates, each with initial guess $\xi_m^{(e)} = 1/3$ and $\rho_m^{(e)} = \rho_{\text{ini}}$ for every candidate material of every element. We run up to 200 objective function evaluations for each p starting at 1, increasing by 0.75 up to 4, while $\gamma = 1$. This continuation technique yielded 116 out of 120 elements with the highest weight above 0.9;

2. We then ran the single candidate-per-element optimization with the optimal candidate and densities obtained from the previous step.

The optimized designs for the different candidate metamaterials is shown in Figure 6.15, where we can see that the horizontal truss (material 2) is mostly placed in a curvy shape following the target sine wave.

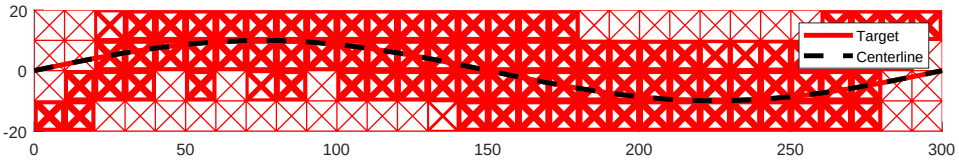

(a) Candidate material 1.

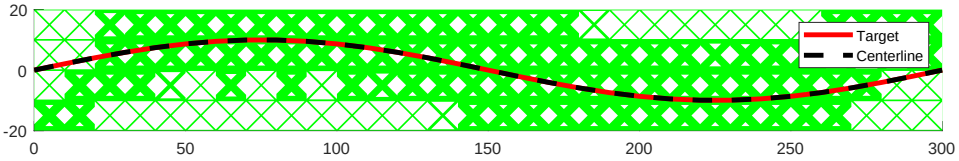

(b) Candidate material 2.

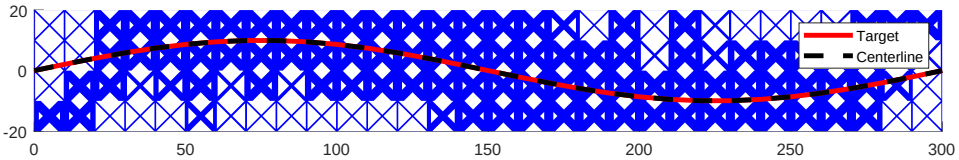

(c) Candidate material 3.

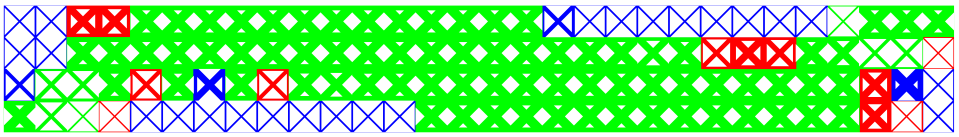

(d) Candidate materials 1, 2 and 3.

Figure 6.15: Optimized beams for different candidate metamaterials (dimensions in mm).

Figure 6.16a shows how the target behavior is approximated in all cases, with a discrepancy close to the borders. The mean square error metric between the current and target nodal displacements is shown in Figure 6.16b, where it can be seen that the use of multiple candidate metamaterials in this problem indeed improved performance. Notice that there is dramatic increase of the error metric at the start of the second stage due to the removal of the non-optimal candidates in each element, but the target shape performance is recovered at the end of the second stage of optimization. This example shows how our multiple metamaterial framework is capable of solving shape matching problems, and it is able to yield superior performance to single candidate metamaterials as expected.

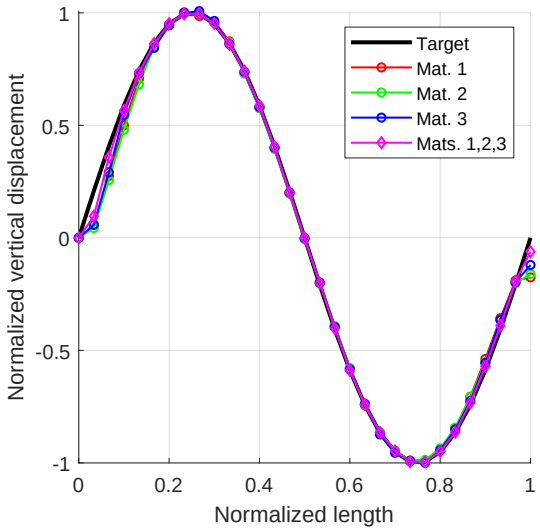

(a) Centerline displacement.

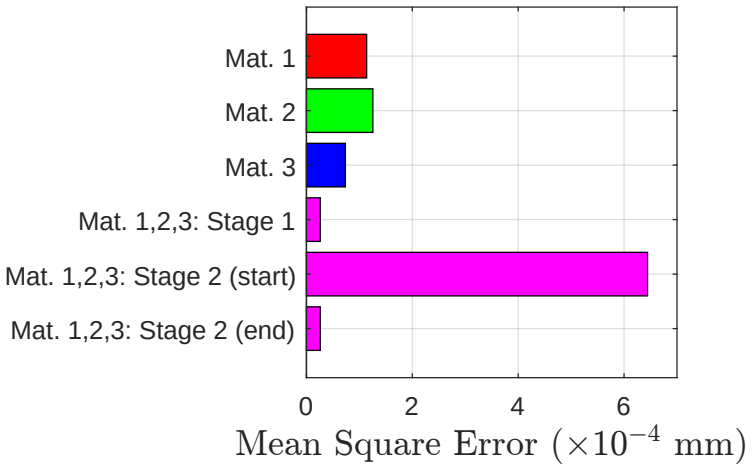

(b) Mean square error.

Figure 6.16: Comparison of the results for the optimized designs with different candidate metamaterials.

7
Final Remarks

Mechanical cloaking is still an open problem, and most if not all optimization-based solutions currently present in the literature are limited to a finite set the linear static loading cases. In our work, we introduced a static-condensation-based to the CBC paradigm, which permits the designer to separate the cloaking device from the surrounding structure throughout the optimization process. Additionally, it gives further insight to the root cause of the cloaking problem, namely the discrepant mechanical behavior along the cloak-surrounding interface. The nodal force vectors shown in the results to benchmark cloaking problems discussed in this manuscript reveal that even if the boundary conditions slightly approach the reference's, the cloaking effect is significantly increased.

A homogenization-based multi-metamaterial selection method based on the DCP technique was developed and tested, yielding a method to select both the family and density of metamaterials simultaneously. However, we did not implement a compatibility formulation to this strategy, and the drawbacks to the hierarchical homogenization-based elastostatic multiscale analysis still apply. Additionally, while DMO and DCP methods were used to select candidate materials, they are not optimal in the context of target behavior problems. This is because the penalization for selecting multiple candidates is introduced by reducing the material stiffness. While this strategy works well for the minimum compliance problems they were initially intended for, the same is not always true for mechanical cloaking, as cloaking devices require both a spectrum of material properties for high cloaking efficiency, and not just placing a stiff material everywhere.

The multi-metamaterial selection method was adapted to solve shape matching problems, but in our tests, we had better results by using a traditional norm-of-displacement objective function rather than with the CBC paradigm. The CBC paradigm can be adapted to the solution of shape matching problems by prescribing the target displacement and setting the target nodal forces to zero (for internal nodes). As expected, better results were obtained when multiple candidate metamaterials are available, but optimized results requires post-processing in the form of a second stage of single-candidate optimization.

Finally, we briefly address the open topic of unbiased cloaks in our suggestion for future work (in the following section), which has not been explored to its full potential yet. The seminal works by Pendry et al. (2006);

Leonhardt (2006) proposed manipulating the governing equations to develop a physical cloak, but optimization-based approaches "brute force" their solution by reducing an error metric. The former approach naturally yields an unbiased cloak, but the latter is limited, at best, to a finite set of loading cases. While the governing differential equations cannot easily be manipulated in the same way as in other physical ways, we showed how static condensation can be leveraged to produce a suitable objective function for the unbiased elastostatic cloaking problem. This idea could not be further explored in our work due to time constraints and is left as a suggestion to future works. This approach may potentially be extended to the dynamic case for low frequencies. For higher frequencies, model order reduction methods may be required, which would produce frequency-dependent cloaks.

7.1 Suggestions for future work

In this final section, we propose how to leverage static condensation in two highly-relevant TO applications that could not be explored in this work, but is left as suggestions for future work.

7.1.1 Unbiased Static Cloaking

An unbiased static cloaking device is one that works for virtually any loading condition. In the elastostatic case, a suitable objective function may be derived by manipulating static condensation expressions, which we detail in what follows From Equation (4-9) we obtain

$$\begin{aligned}\mathbf{f}_{\mathrm{m}} &= \mathbf{K}_{\mathrm{mm}}^{\mathrm{sur}}\mathbf{u}_{\mathrm{m}} + \mathbf{K}_{\mathrm{mm}}^{\mathrm{cloak}}\mathbf{u}_{\mathrm{m}} + \mathbf{K}_{\mathrm{ms}}^{\mathrm{cloak}}\mathbf{u}_{s} \\ &= \mathbf{K}_{\mathrm{mm}}^{\mathrm{sur}}\mathbf{u}_{\mathrm{m}} + \begin{bmatrix}\mathbf{K}_{\mathrm{mm}}^{\mathrm{cloak}} & \mathbf{K}_{\mathrm{ms}}^{\mathrm{cloak}}\end{bmatrix}\begin{bmatrix}\mathbf{u}_{\mathrm{m}} \\ \mathbf{u}_{\mathrm{s}}\end{bmatrix}. \end{aligned} \tag{7-1}$$

Equation (7-1) shows that, even if we designed a cloaking device with compatible stiffness at the boundary (i.e., if $\begin{bmatrix}\mathbf{K}_{\mathrm{mm}}^{\mathrm{cloak}} & \mathbf{K}_{\mathrm{ms}}^{\mathrm{cloak}}\end{bmatrix}$ was exactly the same as that from the reference domain), the displacement vector of the slaves ($\mathbf{u}_s$) is the mathematical reason for the discrepancy between elastostatic behavior of the original and modified structure.

Let us remove $\mathbf{u}_s$ (before partitioning the stiffnes matrix) from the equation by first solving Equation (4-1) for the displacement of the slaves, which yields

$$\mathbf{u}_{\mathrm{s}} = \mathbf{K}_{\mathrm{ss}}^{-1}\left(\mathbf{f}_{\mathrm{s}} - \mathbf{K}_{\mathrm{sm}}\mathbf{u}_{m}\right). \tag{7-2}$$

Substituting Equation (7-2) back into Equation (7-1), leads to the expression

$$\begin{aligned} \mathbf{f}_{\mathrm{m}} &= \mathbf{K}_{\mathrm{mm}}\mathbf{u}_{\mathrm{m}} + \mathbf{K}_{\mathrm{ms}}\left[\mathbf{K}_{\mathrm{ss}}^{-1}\left(\mathbf{f}_{\mathrm{s}} - \mathbf{K}_{\mathrm{sm}}\mathbf{u}_{m}\right)\right] \\ \underbrace{\mathbf{f}_{\mathrm{m}} - \mathbf{K}_{\mathrm{ms}}\mathbf{K}_{\mathrm{ss}}^{-1}\mathbf{f}_{s}}_{\mathbf{f}_R} &= \underbrace{\left(\mathbf{K}_{\mathrm{mm}} - \mathbf{K}_{\mathrm{ms}}\mathbf{K}_{\mathrm{ss}}^{-1}\mathbf{K}_{\mathrm{sm}}\right)}_{\mathbf{K}_R}\mathbf{u}_{\mathrm{m}} \\ \mathbf{f}_{\mathrm{R}} &= \mathbf{K}_{\mathrm{R}}\mathbf{u}_{\mathrm{m}}, \end{aligned} \tag{7-3}$$

where $\mathbf{f}_{\mathrm{R}}$ and $\mathbf{K}_{\mathrm{R}}$ are the reduced force and stiffness vectors, respectively.

In the special case where the external forces of the slaves ($\mathbf{f}_s$) are zero (i.e., no external forces on Γ_{in}), as assumed by Guyan (1965), the reduced linear system from Equation (7-3) becomes

$$\mathbf{f}_m = (\mathbf{K}_{\mathrm{mm}} - \mathbf{K}_{\mathrm{ms}}\mathbf{K}_{\mathrm{ss}}^{-1}\mathbf{K}_{\mathrm{sm}})\mathbf{u}_m. \tag{7-4}$$

The solution to Equation (7-4) is the same as $\mathbf{f}_m = \mathbf{K}_{\mathrm{mm}}\mathbf{u}_m$, i.e., the original response of the surrounding region, if the term $\mathbf{K}^{\mathrm{msm}} = \mathbf{K}_{\mathrm{ms}}\mathbf{K}_{\mathrm{ss}}^{-1}\mathbf{K}_{\mathrm{sm}}$ is the same as that of the virtual domain. Therefore, we can theoretically design an unbiased cloak for the surrounding region (Ω_{sur}) by satisfying the condition

$$\Delta\mathbf{K} = \mathbf{K}_{\mathrm{physical}}^{\mathrm{msm}} - \mathbf{K}_{\mathrm{virtual}}^{\mathrm{msm}} = 0, \tag{7-5}$$

where the superscripts refer to the holed and unholed domains in Figure 4.3, respectively.

Finally, we can pose the unbiased cloak design as an optimization problem in the form

$$\begin{aligned} \min_{\mathbf{z}} \quad & \|\Delta\mathbf{K}(\mathbf{z})\| \\ \text{s.t.} \quad & \mathbf{z} \in \mathcal{Z}, \end{aligned} \tag{7-6}$$

where $\|\bullet\|$ is a suitable norm operator and $\mathcal{Z}$ is some feasible set of the design variables. In contrast to Equation (4-11), this formulation requires no solution to the structural problem, since it must be valid for virtually any load case (without external forces applied to the slaves). Additionally, other objective function, say, based on deformation energy, may be used instead of the more direct approach presented here.

The main challenge in deriving and implementing this is how to define a suitable objective function. This is important to efficiently solve the problem in Equation (7-6), since approaching each component in $\mathbf{K}^{\mathrm{msm}}$ may be difficult or impossible in practice. Notice that, though it has the same dimensions as $\mathbf{K}_{\mathrm{mm}}$, the term $\mathbf{K}^{\mathrm{msm}}$ contains no elements from Ω_{sur}, due to our definition master-slave partition. Still, for finely discretized meshes, some model order reduction technique based on spectral or singular value decompositions may be employed to approximate the most important eigenvalues of $\mathbf{K}^{\mathrm{cloak}}$ to its target. A similar

process may be done for dynamic analysis using Guyan reduction, though it is limited for low frequencies, as the eingenfrequencies are set to zero in the original derivation (Guyan, 1965).

7.1.2 Homogenizationless Microstructure Design

In the context of multiscale optimization, it has been noted that

> Most (if not all) multi-scale approaches make use of homogenization, which assumes separation of scales, i.e., microstructure should be much smaller than the macrostructure. This assumption often becomes invalid when considering the finite resolution of manufacturing processes. (Wu et al., 2021)

A microstructure design framework for mechanical cloaking based on static condensation (and not homogenization) is presented in this section. The core idea is to use a finely discretized domains to simulate the microstructure of each unit cell, but condensing the internal DOFs during full-scale analysis. In this way, we are representing the unit cells by the so-called superelements that explicitly maintain only nodes and DOFs from their boundary.

In the elastostatic case, these superelements yield exactly the same solution (i.e., displacement field) as a full-scale analysis with condensing the slaves, as shown in Figure 4.2. This is basically the superelement method (SEM), i.e., a "group of finite elements in which part of the degrees of freedom is condensed out for computational and modeling purposes" (Qu, 2004).

The main steps in our SEM-based microstructure design framework are detailed below:

1. **Full-scale analysis** : First, we analyze the original domain subjected to the boundary conditions on Γ_{BC}, simulating each microstructure by a superelement.

2. **Microstructure design** : The domain is the partitioned into the surrounding, cloak and hole regions The superelements that fall into the cloaking region are designed sequentially with the previously described CBC-based paradigm. The prescribed displacement field is that found in step 1, and the target nodal forces depends on where each boundary node is:

   - Nodes alongside Γ_{in}: $\overline{\mathbf{f}} = \mathbf{0}$ owing to equilibrium, since we assume that there is no external force applied to the hole.
   - Nodes alongside Γ_{out}: $\overline{\mathbf{f}}$ is that from the full-scale analysis of the reference virtual domain in step 1, satisfying the CBC paradigm.

– Internal nodes: $\overline{\mathbf{f}}$ is the nodal force from the optimization result from the adjacent superelement if already optimized. If the adjacent superelement has not yet been optimized, this node will not be considered in the objective function.

3. Full-scale evaluation : The performance of the multiscale structure is evaluated by replacing the microstructures as superelements in the physical domain mesh.

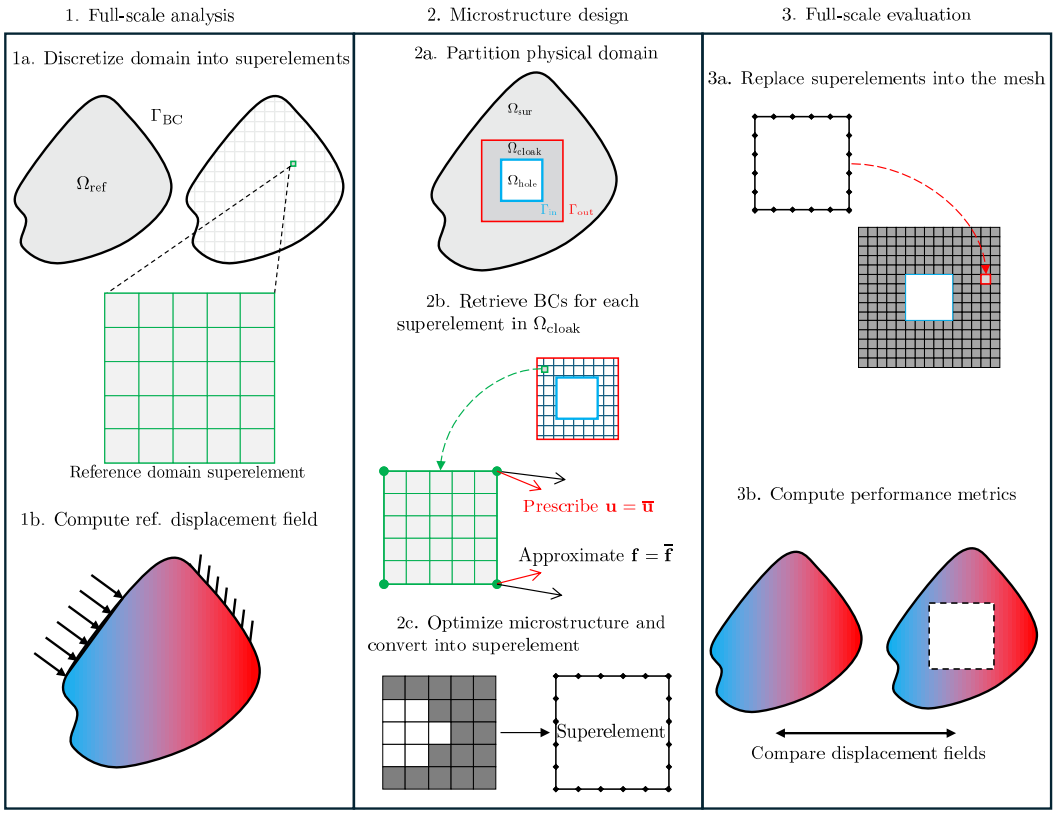

Figure 7.1: Diagram of main steps of our microstructure design framework applied to a single load case elastostatic cloaking problem.

Figure 7.1 shows a diagram with the flow of steps required in our approach, which can be summarized into designing ad-hoc microstructures as superelements and replacing them into the cloaking device. In this sense, the CBC paradigm is applied at both the macro-scale (ensuring cloak-surrounding compatibility) but also at the microscale (ensuring physically compatible microstructure). The trade off consists in executing many smaller optimization processes rather than a single costly one. Since the computational cost of analyses increase nonlinear with the problem size, this may pose as a reasonable solution for mechanical cloaking problems where this trade off is reasonable, such as in quick prototyping of parts fabricated with additive manufacturing processes.

8
Bibliography

Jacob Aboudi, Steven M Arnold, and Brett A Bednarcyk. *Micromechanics of composite materials: a generalized multiscale analysis approach*. Butterworth-Heinemann, 2012. Cited 2 times in pages 54 and 55.

Jacob Aboudi, Steven M Arnold, and Brett A Bednarcyk. *Practical micromechanics of composite materials*. Butterworth-Heinemann, 2021. Cited in page 56.

Joe Alexandersen and Boyan S Lazarov. Topology optimisation of manufacturable microstructural details without length scale separation using a spectral coarse basis preconditioner. *Computer Methods in Applied Mechanics and Engineering*, 290:156–182, 2015. Cited in page 33.

Grégoire Allaire, François Jouve, and Anca-Maria Toader. A level-set method for shape optimization. *Comptes Rendus Mathematique*, 334(12):1125–1130, 2002. Cited in page 27.

Juan C Álvarez Hostos, Víctor D Fachinotti, and Ignacio Peralta. Metamaterial for elastostatic cloaking under thermal gradients. *Scientific reports*, 9(1):1–9, 2019. Cited in page 36.

Erik Andreassen and Casper Schousboe Andreasen. How to determine composite material properties using numerical homogenization. *Computational Materials Science*, 83:488–495, 2014. Cited in page 55.

Jan-Hendrik Bastek, Siddhant Kumar, Bastian Telgen, Raphaël N Glaesener, and Dennis M Kochmann. Inverting the structure–property map of truss metamaterials by deep learning. *Proceedings of the National Academy of Sciences*, 119(1):e2111505119, 2022. Cited in page 30.

KJ Bathe. *Finite element procedures*. Klaus-Jurgen Bathe, Watertown, MA, 2nd edition, 2014. ISBN 978-0-9790049-5-7. Cited in page 46.

Brett A Bednarcyk and Steven M Arnold. A multiscale, nonlinear, modeling framework enabling the design and analysis of composite materials and structures. Technical report, 2012. Cited 2 times in pages 12 and 53.

Reza Behrou, Maroun Abi Ghanem, Brianna C Macnider, Vimarsh Verma, Ryan Alvey, Jinho Hong, Ashley F Emery, Hyunsun Alicia Kim, and

Nicholas Boechler. Topology optimization of nonlinear periodically microstructured materials for tailored homogenized constitutive properties. *Composite Structures*, 266:113729, 2021. Cited in page 34.

Martin Philip Bendsøe. Optimal shape design as a material distribution problem. *Structural optimization*, 1(4):193–202, 1989. Cited in page 27.

Martin Philip Bendsøe and Noboru Kikuchi. Generating optimal topologies in structural design using a homogenization method. *Computer methods in applied mechanics and engineering*, 71(2):197–224, 1988. Cited 6 times in pages 8, 24, 25, 26, 31, and 57.

Martin Philip Bendsøe and Ole Sigmund. *Topology optimization: theory, methods, and applications*. Springer Science & Business Media, Berlin, Brandenburg, 2nd edition, 2002. Cited in page 26.

Franco Bontempi, Konstantinos Gkoumas, and Stefania Arangio. Systemic approach for the maintenance of complex structural systems. *Structure and infrastructure engineering*, 4(2):77–94, 2008. Cited in page 18.

Blaise Bourdin and Antonin Chambolle. Design-dependent loads in topology optimization. *ESAIM: Control, Optimisation and Calculus of Variations*, 9: 19–48, 2003. Cited in page 27.

Matteo Bruggi and Pierre Duysinx. Topology optimization for minimum weight with compliance and stress constraints. *Structural and Multidisciplinary Optimization*, 46(3):369–384, 2012. Cited in page 18.

Michele Brun, Sébastien Guenneau, and Alexander B Movchan. Achieving control of in-plane elastic waves. *Applied physics letters*, 94(6):061903, 2009. Cited in page 35.

Tyler E Bruns and Daniel A Tortorelli. Topology optimization of non-linear elastic structures and compliant mechanisms. *Computer methods in applied mechanics and engineering*, 190(26-27):3443–3459, 2001. Cited in page 83.

Tiemo Bückmann, Michael Thiel, Muamer Kadic, Robert Schittny, and Martin Wegener. An elasto-mechanical unfeelability cloak made of pentamode metamaterials. *Nature communications*, 5(1):1–6, 2014. Cited 3 times in pages 8, 35, and 36.

Tiemo Bückmann, Muamer Kadic, Robert Schittny, and Martin Wegener. Mechanical cloak design by direct lattice transformation. *Proceedings of*

the National Academy of Sciences, 112(16):4930–4934, 2015. Cited 4 times in pages 35, 67, 91, and 92.

Yu-Chin Chan, Faez Ahmed, Liwei Wang, and Wei Chen. Metaset: Exploring shape and property spaces for data-driven metamaterials design. *Journal of Mechanical Design*, 143(3), 2021. Cited in page 36.

Yu-Chin Chan, Daicong Da, Liwei Wang, and Wei Chen. Remixing functionally graded structures: data-driven topology optimization with multiclass shape blending. *Structural and Multidisciplinary Optimization*, 65(5):1–22, 2022. Cited 5 times in pages 11, 21, 38, 98, and 99.

Xubing Cheng, Chang Liu, Weisheng Zhang, Zhiyuan Tang, Yongquan Liu, Shan Tang, Zongliang Du, Tianchen Cui, and Xu Guo. A compatible boundary condition-based topology optimization paradigm for static mechanical cloak design. *Extreme Mechanics Letters*, 65:102100, 2023. Cited 7 times in pages 21, 38, 39, 62, 68, 70, and 88.

Hayoung Chung and Zongliang Du. Optimized design of multi-material cellular structures by a level-set method with guyan reduction. *Journal of Mechanical Design*, 143(10):101702, 2021. Cited in page 39.

Eugene Cosserat and François Cosserat. *Théorie des corps déformables*. A. Hermann et fils, 1909. Cited in page 35.

Andrew D Cramer, Vivien J Challis, and Anthony P Roberts. Microstructure interpolation for macroscopic design. *Structural and Multidisciplinary Optimization*, 53(3):489–500, 2016. Cited in page 33.

Steven A Cummer, Bogdan-Ioan Popa, David Schurig, David R Smith, John Pendry, Marco Rahm, and Anthony Starr. Scattering theory derivation of a 3d acoustic cloaking shell. *Physical review letters*, 100(2):024301, 2008. Cited in page 34.

Christopher Czech. *Design of Meta-materials outside the homogenization limit using multiscale analysis and topology optimization*. PhD thesis, Clemson University, 2012. Cited in page 39.

MR Dias, PR Fernandes, JM Guedes, and SJ Hollister. Permeability analysis of scaffolds for bone tissue engineering. *Journal of biomechanics*, 45(6): 938–944, 2012. Cited in page 29.

Zongliang Du, Xiao-Yi Zhou, Renato Picelli, and H Alicia Kim. Connecting microstructures for multiscale topology optimization with connectivity index

constraints. *Journal of Mechanical Design*, 140(11):111417, 2018. Cited 2 times in pages 33 and 98.

Yalchin Efendiev, Victor Ginting, and Thomas Y Hou. Multiscale finite element methods for nonlinear problems and their applications. 2004. Cited in page 28.

Víctor D Fachinotti, Ignacio Peralta, and Alejandro E Albanesi. Optimization-based design of an elastostatic cloaking device. *Scientific Reports*, 8(1):1–8, 2018. Cited 12 times in pages 12, 19, 35, 67, 68, 82, 85, 86, 88, 91, 92, and 97.

Mohamed Farhat, Stefan Enoch, Sébastien Guenneau, and AB Movchan. Broadband cylindrical acoustic cloak for linear surface waves in a fluid. *Physical review letters*, 101(13):134501, 2008. Cited in page 34.

Federico Ferrari and Ole Sigmund. Revisiting topology optimization with buckling constraints. *Structural and Multidisciplinary Optimization*, 59(5): 1401–1415, 2019. Cited in page 18.

Frédéric Feyel. A multilevel finite element method (fe2) to describe the response of highly non-linear structures using generalized continua. *Computer Methods in applied Mechanics and engineering*, 192(28-30):3233–3244, 2003. Cited in page 28.

Eric Garner, Helena MA Kolken, Charlie CL Wang, Amir A Zadpoor, and Jun Wu. Compatibility in microstructural optimization for additive manufacturing. *Additive Manufacturing*, 26:65–75, 2019. Cited 2 times in pages 29 and 33.

Oliver Giraldo-Londoño and Glaucio H Paulino. Polystress: a matlab implementation for local stress-constrained topology optimization using the augmented lagrangian method. *Structural and Multidisciplinary Optimization*, 63:2065–2097, 2021. Cited 2 times in pages 61 and 82.

Jeroen P Groen and Ole Sigmund. Homogenization-based topology optimization for high-resolution manufacturable microstructures. *International Journal for Numerical Methods in Engineering*, 113(8):1148–1163, 2018. Cited 2 times in pages 8 and 26.

Sebastien Guenneau, Claude Amra, and Denis Veynante. Transformation thermodynamics: cloaking and concentrating heat flux. *Optics Express*, 20 (7):8207–8218, 2012. Cited in page 34.

Robert J Guyan. Reduction of stiffness and mass matrices. *AIAA journal*, 3 (2):380–380, 1965. Cited 3 times in pages 62, 104, and 105.

Zvi Hashin and Shmuel Shtrikman. A variational approach to the theory of the elastic behaviour of multiphase materials. *Journal of the Mechanics and Physics of Solids*, 11(2):127–140, 1963. Cited in page 28.

Scott J Hollister. Porous scaffold design for tissue engineering. *Nature materials*, 4(7):518–524, 2005. Cited in page 29.

Scott J Hollister and Noboru Kikuchi. A comparison of homogenization and standard mechanics analyses for periodic porous composites. *Computational mechanics*, 10(2):73–95, 1992. Cited in page 29.

Gerhard A Holzapfel. Nonlinear solid mechanics: a continuum approach for engineering science, 2002. Cited 2 times in pages 41 and 43.

Thomas Y Hou and Xiao-Hui Wu. A multiscale finite element method for elliptic problems in composite materials and porous media. *Journal of computational physics*, 134(1):169–189, 1997. Cited in page 28.

Thomas JR Hughes. *The finite element method: linear static and dynamic finite element analysis*. Courier Corporation, 2003. Cited in page 46.

Bruce Irons. Structural eigenvalue problems-elimination of unwanted variables. *AIAA journal*, 3(5):961–962, 1965. Cited in page 62.

Dongchan Jang and Julia R Greer. Transition from a strong-yet-brittle to a stronger-and-ductile state by size reduction of metallic glasses. *Nature materials*, 9(3):215–219, 2010. Cited in page 28.

George Kazakis and Nikos D Lagaros. A simple matlab code for material design optimization using reduced order models. *Materials*, 15(14):4972, 2022. Cited in page 39.

Jessica M Kemppainen and Scott J Hollister. Tailoring the mechanical properties of 3d-designed poly (glycerol sebacate) scaffolds for cartilage applications. *Journal of Biomedical Materials Research Part A: An Official Journal of The Society for Biomaterials, The Japanese Society for Biomaterials, and The Australian Society for Biomaterials and the Korean Society for Biomaterials*, 94(1):9–18, 2010. Cited in page 29.

Lily Kharevych, Patrick Mullen, Houman Owhadi, and Mathieu Desbrun. Numerical coarsening of inhomogeneous elastic materials. *ACM Transactions on graphics (TOG)*, 28(3):1–8, 2009. Cited in page 30.

Nam-Ho Kim. *Introduction to nonlinear finite element analysis*. Springer Science & Business Media, New York, NY, 2015th edition, 2014. ISBN 978-1-4419-1745-4. doi: 10.1007/978-1-4419-1746-1. Cited in page 47.

Ulf Leonhardt. Optical conformal mapping. *science*, 312(5781):1777–1780, 2006. Cited 3 times in pages 18, 34, and 103.

Hui Liu, Yiqiang Wang, Hongming Zong, and Michael Yu Wang. Efficient structure topology optimization by using the multiscale finite element method. *Structural and Multidisciplinary Optimization*, 58(4):1411–1430, 2018. Cited in page 28.

Yifu Lu and Liyong Tong. Concurrent multiscale topology optimization of metamaterials for mechanical cloak. *Computer Methods in Applied Mechanics and Engineering*, 409:115966, 2023. Cited in page 38.

Yunfeng Luo, Wenjiong Chen, Shutian Liu, Quhao Li, and Yaohui Ma. A discrete-continuous parameterization (dcp) for concurrent optimization of structural topologies and continuous material orientations. *Composite Structures*, 236:111900, 2020. Cited in page 75.

EH Mansfield. Neutral holes in plane sheet: Reinforced holes which are elastically equivalent to the uncut sheet. arc 13, 728—strut 1407, sept. 1950; published as r. and m. no. 2815, 1956. Cited in page 34.

G Thomas Mase, Ronald E Smelser, and George E Mase. *Continuum mechanics for engineers*. CRC press, Boca Raton, Fl, 2nd edition, 1999. Cited in page 41.

Lucas R Meza, Satyajit Das, and Julia R Greer. Strong, lightweight, and recoverable three-dimensional ceramic nanolattices. *Science*, 345(6202): 1322–1326, 2014. Cited 3 times in pages 8, 27, and 28.

Graeme W Milton, Marc Briane, and John R Willis. On cloaking for elasticity and physical equations with a transformation invariant form. *New journal of physics*, 8(10):248, 2006. Cited in page 35.

HP Mlejnek. Some aspects of the genesis of structures. *Structural optimization*, 5(1):64–69, 1992. Cited in page 26.

David J Munk, Douglass J Auld, Grant P Steven, and Gareth A Vio. On the benefits of applying topology optimization to structural design of aircraft components. *Structural and Multidisciplinary Optimization*, 60(3):1245–1266, 2019. Cited in page 18.

Andrew N Norris and Alexander L Shuvalov. Elastic cloaking theory. *Wave Motion*, 48(6):525–538, 2011. Cited in page 35.

J Tinsley Oden. *Finite elements of nonlinear continua*. Courier Corporation, 2006. Cited in page 48.

Olivier Pantz and Karim Trabelsi. A post-treatment of the homogenization method for shape optimization. *SIAM Journal on Control and Optimization*, 47(3):1380–1398, 2008. Cited in page 30.

H Patel. Multidisciplinary design optimization with superelements in msc/-nastran. In *4th Symposium on Multidisciplinary Analysis and Optimization*, page 4732, 1992. Cited in page 39.

Neal M Patel, Byung-Soo Kang, John E Renaud, and Andrés Tovar. Crashworthiness design using topology optimization. *Journal of mechanical design*, 131(6), 2009. Cited in page 18.

John B Pendry, David Schurig, and David R Smith. Controlling electromagnetic fields. *science*, 312(5781):1780–1782, 2006. Cited 5 times in pages 8, 18, 34, 35, and 102.

Agustí Pérez-Foguet, Antonio Rodríguez-Ferran, and Antonio Huerta. Numerical differentiation for local and global tangent operators in computational plasticity. *Computer Methods in Applied Mechanics and Engineering*, 189 (1):277–296, 2000. Cited in page 78.

Bogdan-Ioan Popa, Lucian Zigoneanu, and Steven A Cummer. Experimental acoustic ground cloak in air. *Physical review letters*, 106(25):253901, 2011. Cited in page 34.

Kepeng Qiu, Weihong Zhang, Matthieu Domaszewski, and Dominique Chamoret. Topology optimization of periodic cellular solids based on a superelement method. *Engineering Optimization*, 41(3):225–239, 2009. Cited 2 times in pages 39 and 62.

Zu-Qing Qu. *Model order reduction techniques with applications in finite element analysis*. Springer Science & Business Media, 2004. Cited 2 times in pages 62 and 105.

Arash Radman, Xiaodong Huang, and YM Xie. Topology optimization of functionally graded cellular materials. *Journal of Materials Science*, 48(4): 1503–1510, 2013. Cited in page 32.

Singiresu S Rao. *Engineering optimization: theory and practice*. John Wiley & Sons, 2019. Cited in page 60.

ED Sanders, MA Aguiló, and GH Paulino. Optimized lattice-based metamaterials for elastostatic cloaking. *Proceedings of the Royal Society A*, 477(2253): 20210418, 2021a. Cited 4 times in pages 8, 36, 37, and 67.

ED Sanders, A Pereira, and GH Paulino. Optimal and continuous multilattice embedding. *Science Advances*, 7(16):eabf4838, 2021b. Cited 3 times in pages 8, 32, and 75.

Emily D Sanders, Anderson Pereira, Miguel A Aguiló, and Glaucio H Paulino. Polymat: an efficient matlab code for multi-material topology optimization. *Structural and Multidisciplinary Optimization*, 58(6):2727–2759, 2018. Cited 4 times in pages 75, 76, 80, and 96.

Christian Schumacher, Bernd Bickel, Jan Rys, Steve Marschner, Chiara Daraio, and Markus Gross. Microstructures to control elasticity in 3d printing. *ACM Transactions on Graphics (Tog)*, 34(4):1–13, 2015. Cited 5 times in pages 8, 20, 30, 31, and 33.

R Schwaiger, LR Meza, and X Li. The extreme mechanics of micro-and nanoarchitected materials. *MRS Bulletin*, 44(10):758–765, 2019. Cited in page 28.

Fernando V Senhora, Emily D Sanders, and Glaucio H Paulino. Optimally-tailored spinodal architected materials for multiscale design and manufacturing. *Advanced Materials*, page 2109304, 2022. Cited 3 times in pages 8, 33, and 38.

Fernando Vasconcelos Senhora, Emily D Sanders, and Glaucio H Paulino. Unbiased mechanical cloaks. *Proceedings of the National Academy of Sciences*, 122(19):e2415056122, 2025. Cited in page 21.

Ole Sigmund. Materials with prescribed constitutive parameters: an inverse homogenization problem. *International Journal of Solids and Structures*, 31 (17):2313–2329, 1994. Cited in page 30.

Ole Sigmund. On the design of compliant mechanisms using topology optimization. *Journal of Structural Mechanics*, 25(4):493–524, 1997. Cited in page 18.

Ole Sigmund. A 99 line topology optimization code written in matlab. *Structural and multidisciplinary optimization*, 21(2):120–127, 2001. Cited in page 26.

Ole Sigmund and Kurt Maute. Topology optimization approaches. *Structural and Multidisciplinary Optimization*, 48(6):1031–1055, 2013. Cited in page 18.

Carlo Sinigaglia, Davide E Quadrelli, Andrea Manzoni, and Francesco Braghin. Fast active thermal cloaking through pde-constrained optimization and reduced-order modelling. *Proceedings of the Royal Society A*, 478(2258): 20210813, 2022. Cited in page 39.

M Smith. Abaqus 2016 documentation collection, 2015. Cited in page 26.

Jan Sokolowski and Antoni Zochowski. On the topological derivative in shape optimization. *SIAM journal on control and optimization*, 37(4):1251–1272, 1999. Cited in page 27.

Fabio Sozio, Mostafa Faghih Shojaei, and Arash Yavari. Optimal elastostatic cloaks. *Journal of the Mechanics and Physics of Solids*, 176:105306, 2023. Cited 2 times in pages 9 and 67.

Jan Stegmann and Erik Lund. Discrete material optimization of general composite shell structures. *International Journal for Numerical Methods in Engineering*, 62(14):2009–2027, 2005. Cited 3 times in pages 36, 75, and 76.

Rani W Sullivan and Steven M Arnold. An annotative review of multiscale modeling and its application to scales inherent in the field of icme. *Models, databases, and simulation tools needed for the realization of Integrated Computational Material Engineering*, pages 6–23, 2011. Cited in page 54.

James Utama Surjadi, Libo Gao, Huifeng Du, Xiang Li, Xiang Xiong, Nicholas Xuanlai Fang, and Yang Lu. Mechanical metamaterials and their engineering applications. *Advanced Engineering Materials*, 21(3):1800864, 2019. Cited in page 27.

K Svanberg. MMA and GCMMA - two methods for nonlinear optimization. *Optimization and Systems Theory, Department of Mathematics. KTH - Royal Institute of Technology in Stockholm, Sweden*, pages 1–16, 2007. Cited in page 85.

Krister Svanberg. The method of moving asymptotes—a new method for structural optimization. *International journal for numerical methods in engineering*, 24(2):359–373, 1987. Cited in page 61.

Cameron Talischi, Glaucio H Paulino, Anderson Pereira, and Ivan FM Menezes. PolyTop: a matlab implementation of a general topology optimization framework using unstructured polygonal finite element meshes. *Structural and Multidisciplinary Optimization*, 45(3):329–357, 2012. Cited in page 26.

Salvatore Torquato and HW Haslach Jr. Random heterogeneous materials: microstructure and macroscopic properties. *Appl. Mech. Rev.*, 55(4):B62–B63, 2002. Cited 2 times in pages 29 and 55.

Mathias Wallin and Daniel A Tortorelli. Nonlinear homogenization for topology optimization. *Mechanics of Materials*, 145:103324, 2020. Cited in page 34.

Chao Wang, Zhi Zhao, Ming Zhou, Ole Sigmund, and Xiaojia Shelly Zhang. A comprehensive review of educational articles on structural and multidisciplinary optimization. *Structural and Multidisciplinary Optimization*, 64(5): 2827–2880, 2021. Cited in page 26.

Fengwen Wang, Boyan Stefanov Lazarov, and Ole Sigmund. On projection methods, convergence and robust formulations in topology optimization. *Structural and Multidisciplinary Optimization*, 43(6):767–784, 2011. Cited in page 84.

Liwei Wang, Yu-Chin Chan, Faez Ahmed, Zhao Liu, Ping Zhu, and Wei Chen. Deep generative modeling for mechanistic-based learning and design of metamaterial systems. *Computer Methods in Applied Mechanics and Engineering*, 372:113377, 2020a. Cited 2 times in pages 8 and 37.

Liwei Wang, Yu-Chin Chan, Zhao Liu, Ping Zhu, and Wei Chen. Data-driven metamaterial design with laplace-beltrami spectrum as "shape-dna". *Structural and multidisciplinary optimization*, 61(6):2613–2628, 2020b. Cited 4 times in pages 21, 30, 31, and 36.

Liwei Wang, Jagannadh Boddapati, Ke Liu, Ping Zhu, Chiara Daraio, and Wei Chen. Mechanical cloak via data-driven aperiodic metamaterial design. *Proceedings of the National Academy of Sciences*, 119(13):e2122185119, 2022. Cited 5 times in pages 11, 19, 38, 92, and 93.

Jun Wu, Ole Sigmund, and Jeroen P Groen. Topology optimization of multiscale structures: a review. *Structural and Multidisciplinary Optimization*, 63 (3):1455–1480, 2021. Cited 5 times in pages 29, 30, 33, 54, and 105.

Liang Xia and Piotr Breitkopf. Recent advances on topology optimization of multiscale nonlinear structures. *Archives of Computational Methods in Engineering*, 24(2):227–249, 2017. Cited in page 34.

Yeming Xian, Glaucio H Paulino, and David W Rosen. Integration of additive manufacturing process-induced material characteristics into topology optimization. *Computer Methods in Applied Mechanics and Engineering*, 434: 117503, 2025. Cited in page 60.

Yi Min Xie and Grant P Steven. A simple evolutionary procedure for structural optimization. *Computers & structures*, 49(5):885–896, 1993. Cited in page 27.

Xianchen Xu, Chen Wang, Wan Shou, Zongliang Du, Yangyang Chen, Beichen Li, Wojciech Matusik, Nassar Hussein, and Guoliang Huang. Physical realization of elastic cloaking with a polar material. *Physical review letters*, 124(11):114301, 2020. Cited in page 37.

Fan Yang, Zhong Lei Mei, Tian Yu Jin, and Tie Jun Cui. Dc electric invisibility cloak. *Physical Review Letters*, 109(5):053902, 2012. Cited in page 34.

RJ Yang and CM Lu. Topology optimization with superelements. *AIAA journal*, 34(7):1533–1535, 1996. Cited in page 39.

Masayuki Yano, Tianci Huang, and Matthew J Zahr. A globally convergent method to accelerate topology optimization using on-the-fly model reduction. *Computer Methods in Applied Mechanics and Engineering*, 375:113635, 2021. Cited in page 39.

Gil Ho Yoon. Structural topology optimization for frequency response problem using model reduction schemes. *Computer Methods in Applied Mechanics and Engineering*, 199(25-28):1744–1763, 2010. Cited in page 39.

Sajjad Zargham, Thomas Arthur Ward, Rahizar Ramli, and Irfan Anjum Badruddin. Topology optimization: a review for structural designs under vibration problems. *Structural and Multidisciplinary Optimization*, 53(6): 1157–1177, 2016. Cited in page 18.

Shuang Zhang, Dentcho A Genov, Cheng Sun, and Xiang Zhang. Cloaking of matter waves. *Physical Review Letters*, 100(12):123002, 2008. Cited in page 34.

Shiwei Zhou and Qing Li. Design of graded two-phase microstructures for tailored elasticity gradients. *Journal of Materials Science*, 43(15):5157–5167, 2008. Cited in page 32.

Olek C Zienkiewicz, Robert L Taylor, and Jian Z Zhu. *The finite element method: its basis and fundamentals*. Elsevier Butterworth-Heinemann, Amsterdam, North Holland, 6th edition, 2005. ISBN 0-7506-6320-0. Cited in page 52.

Olgierd Cecil Zienkiewicz and Robert Leroy Taylor. *The finite element method for solid and structural mechanics*. Elsevier, 2005. Cited in page 46.

A
Sensitivity Analysis

The sensitivity of the objective function and the constraints are needed for the gradient-based optimization algorithm. Here, we present the derivation for the sensitibity objective function detailed in Section 4.2, as the gradient of the box constraints is trivial.

Let $\mathcal{F}$ be a function of an arbitrary vector of design variables $\boldsymbol{z}$. The chain rule of the gradient of $\mathcal{F}$ with respect to some component z_i yields

$$\frac{\partial \mathcal{F}}{\partial z_i} = \sum_{e=1}^{\mathrm{N}^{(e)}} \frac{\partial \mathcal{F}}{\partial \rho^{(e)}} \frac{\partial \rho^{(e)}}{\partial \boldsymbol{z}_i}, \tag{A-1}$$

where ρ is a density-like variable associated with each one of the $\mathrm{N}^{(e)}$ elements in the finite element discretization of the structural problem, and the relationship between $\boldsymbol{\rho}$ and $\boldsymbol{z}$ depends on the formulation.

In what follows, we derive the term $\partial\mathcal{F}/\partial\rho^{(e)}$ and then the specific details related to each formulation separately.

A.1
Objective Function: CBC paradigm

We implement the adjoint method to derive the sensitivity of the objective function based on the CBC paradigm, discussed in Chapter 4. Adding a nonzero term to Equation (4-11a) leads to

$$\mathcal{F} = (\Delta\mathbf{f}_{\mathrm{out}})^T \Delta\mathbf{f}_{\mathrm{out}} + \boldsymbol{\lambda}_{\mathrm{free}}^T \left(\overline{\mathbf{f}} - \mathbf{K}\mathbf{u}\right)_{\mathrm{free}}, \tag{A-2}$$

where the term multiplying the adjoint vector is the difference between the target external forces ($\overline{\mathbf{f}}$) and their current internal counterpart ($\mathbf{K}\mathbf{u}$) at the free DOFs (i.e., those without prescribed displacement). The subscripts "free" and "out" denote the free DOFs and those at Γ_{out}, respectively. The difference in the parenthesis is null because equilibrium is enforced in Equation (4-11c), and the nodal force vector ($(\mathbf{K}\mathbf{u})_{\mathrm{free}} = \mathbf{f}_{\mathrm{free}}$) approaches the target ($\overline{\mathbf{f}}_{\mathrm{free}}$) in an optimal design.

Deriving Equation (A-2) with respect to $\rho^{(e)}$ yields

$$\frac{\partial \mathcal{F}}{\partial \rho^{(e)}} = 2\Delta\mathbf{f}_{\mathrm{out}}^T \frac{\partial(\Delta\mathbf{f}_{\mathrm{out}})}{\partial \rho^{(e)}} + \frac{\partial \boldsymbol{\lambda}_{\mathrm{free}}^T}{\partial \rho^{(e)}} \cancelto{\mathbf{0}}{\left(\overline{\mathbf{f}} - \mathbf{K}\mathbf{u}\right)_{\mathrm{free}}} + \boldsymbol{\lambda}_{\mathrm{free}}^T \frac{\partial}{\partial \rho^{(e)}} \left(\overline{\mathbf{f}} - \mathbf{K}\mathbf{u}\right)_{\mathrm{free}}, \tag{A-3}$$

where the canceled term in parenthesis is naught owing to equilibrium.

In the following, we introduce a $\mathrm{N}_{\mathrm{free}} \times N$ constant gather matrix $\mathbf{L}_{\mathrm{free}}$ that collects the free DOFs, with N and $\mathrm{N}_{\mathrm{free}}$ being the total and free

DOFs. Likewise, $\mathbf{L}_{\text{out}}$ is its "outer-DOFs" counterpart. Expanding the terms in Equation (A-3) and collecting terms with $\mathbf{u}$ and $\partial\mathbf{u}/\partial\rho^{(e)}$ gives

$$\begin{aligned}\frac{\partial\mathcal{F}}{\partial\rho^{(e)}} &= 2(\Delta\mathbf{f}_{\text{out}})^T \Bigg(\mathbf{L}_{\text{out}}\frac{\partial\mathbf{K}}{\partial\rho^{(e)}}\mathbf{u} + \mathbf{L}_{\text{out}}\mathbf{K}\frac{\partial\mathbf{u}}{\partial\rho^{(e)}} - \cancelto{\mathbf{0}}{\frac{\partial\bar{\mathbf{f}}_{\text{out}}}{\partial\rho^{(e)}}} \Bigg) \\ &+ \boldsymbol{\lambda}_{\text{free}}^T \cancelto{\mathbf{0}}{\frac{\partial\bar{\mathbf{f}}_{\text{out}}}{\partial\rho^{(e)}}} - \boldsymbol{\lambda}_{\text{free}}^T \left(\mathbf{L}_{\text{free}}\frac{\partial\mathbf{K}}{\partial\rho^{(e)}}\mathbf{u} + \mathbf{L}_{\text{free}}\mathbf{K}\frac{\partial\mathbf{u}}{\partial\rho^{(e)}} \right) \\ &= \left(2\mathbf{L}_{\text{out}}^T\Delta\mathbf{f}_{\text{out}} - \mathbf{L}_{\text{free}}\boldsymbol{\lambda}_{\text{free}}\right)^T \frac{\partial\mathbf{K}}{\partial\rho^{(e)}}\mathbf{u} \\ &+ \left(2\mathbf{K}\mathbf{L}_{\text{out}}^T\Delta\mathbf{f}_{\text{out}} - \mathbf{K}\mathbf{L}_{\text{free}}^T\boldsymbol{\lambda}_{\text{free}}\right)^T \frac{\partial\mathbf{u}}{\partial\rho^{(e)}}. \end{aligned} \tag{A-4}$$

We can vanish the term with $\partial\mathbf{u}/\partial\rho^{(e)}$ in Equation (A-4) by setting the terms in the parenthesis to zero, yielding the following linear system for λ:

$$\mathbf{K}\mathbf{L}_{\text{free}}^T\boldsymbol{\lambda}_{\text{free}} = 2\mathbf{K}\mathbf{L}_{\text{out}}^T\Delta\mathbf{f}_{\text{out}}, \tag{A-5}$$

which is solved for the free DOFs to avoid singularity.

Once $\boldsymbol{\lambda}_{\text{free}}$ is computed, we can finally obtain the gradient of the objective function from Equation (A-4) as

$$\frac{\partial\mathcal{F}}{\partial\rho^{(e)}} = \left(2\mathbf{L}_{\text{out}}^T\Delta\mathbf{f}_{\text{out}} - \mathbf{L}_{\text{free}}^T\boldsymbol{\lambda}_{\text{free}}\right)^T \frac{\partial\mathbf{K}}{\partial\rho^{(e)}}\mathbf{u}, \tag{A-6}$$

where we remark that it is imperative the consistent use of gather matrices in Equations (A-5) and (A-6) to correctly compute the sensitivity.

The partial derivative in Equation (A-6) is computed by assembling the element-level contributions from Equation (3-40b), yielding

$$\frac{\partial\mathbf{K}}{\partial\rho^{(e)}} = \sum_e \left(\mathbf{L}^{(e)}\right)^T \frac{\partial\mathbf{K}^{(e)}}{\partial\rho^{(e)}}\mathbf{L}^{(e)}, \tag{A-7}$$

where, in general, the stiffness matrix of a given element depends only on its own density $\rho^{(e)}$, which can reduce Equation (A-7) to

$$\frac{\partial\mathbf{K}}{\partial\rho^{(e)}} = \left(\mathbf{L}^{(e)}\right)^T \frac{\partial\mathbf{K}^{(e)}}{\partial\rho^{(e)}}\mathbf{L}^{(e)}. \tag{A-8}$$

The derivative of the element stiffness matrix in Equation (A-8) is discussed in detail in the following sections for each formulation separately.

A.2 DCP-based multi-mematerial selection

The sensitivity of the DCP-based multi-metamaterial objective function is split in two parts, following the definition of the design variable in Equa-

tion (5-3). The element-level sensitivity for each candidate material is stored as

$$\frac{\partial \mathcal{F}}{\partial z_m^{(e)}} = \begin{bmatrix} \dfrac{\partial \mathcal{F}}{\partial \rho_m^{(e)}} & \dfrac{\partial \mathcal{F}}{\partial \xi_m^{(e)}} \end{bmatrix}, \tag{A-9}$$

where each term is computed from

$$\frac{\partial \mathcal{F}}{\partial \rho_m^{(e)}} = \left(2\mathbf{L}_{\text{out}}^T \Delta \mathbf{f}_{\text{out}} - \mathbf{L}_{\text{free}}^T \boldsymbol{\lambda}_{\text{free}}\right)^T \frac{\partial \mathbf{K}_m}{\partial \rho^{(e)}} \mathbf{u}, \qquad \text{and} \tag{A-10a}$$

$$\frac{\partial \mathcal{F}}{\partial \xi_m^{(e)}} = \left(2\mathbf{L}_{\text{out}}^T \Delta \mathbf{f}_{\text{out}} - \mathbf{L}_{\text{free}}^T \boldsymbol{\lambda}_{\text{free}}\right)^T \frac{\partial \mathbf{K}_m}{\partial \xi^{(e)}} \mathbf{u}, \tag{A-10b}$$

with

$$\frac{\partial \mathbf{K}}{\partial \rho^{(e)}} = \left(\mathbf{L}^{(e)}\right)^T \frac{\partial \mathbf{K}^{(e)}}{\partial \rho^{(e)}} \mathbf{L}^{(e)}, \qquad \text{and} \tag{A-11a}$$

$$\frac{\partial \mathbf{K}}{\partial \xi^{(e)}} = \left(\mathbf{L}^{(e)}\right)^T \frac{\partial \mathbf{K}^{(e)}}{\partial \xi^{(e)}} \mathbf{L}^{(e)} \tag{A-11b}$$

as explained in Appendix A.1.

We find the derivatives in Equation (A-11) by deriving Equation (5-9) with respect to each design variable, which gives:

$$\begin{aligned} \frac{\partial \mathbf{K}^{(e)}}{\partial \rho_m^{(e)}} &= \left(\overline{\mathbf{w}}^{(e)}\right)^T \frac{\mathbf{C}_{11}^{(e)}}{\partial \rho_m^{(e)}} \mathbf{K}_{11}^{(e)} + \left(\overline{\mathbf{w}}^{(e)}\right)^T \frac{\mathbf{C}_{22}^{(e)}}{\partial \rho_m^{(e)}} \mathbf{K}_{22}^{(e)} \\ &\quad + \left(\overline{\mathbf{w}}^{(e)}\right)^T \frac{\mathbf{C}_{33}^{(e)}}{\partial \rho_m^{(e)}} \mathbf{K}_{33}^{(e)} + \left(\overline{\mathbf{w}}^{(e)}\right)^T \frac{\mathbf{C}_{12}^{(e)}}{\partial \rho_m^{(e)}} \mathbf{K}_{12}^{(e)}. \qquad \text{and} \end{aligned} \tag{A-12}$$

$$\begin{aligned} \frac{\partial \mathbf{K}^{(e)}}{\partial \xi_m^{(e)}} &= \left(\frac{\overline{\mathbf{w}}^{(e)}}{\partial \xi_m^{(e)}}\right)^T \mathbf{C}_{11}^{(e)} \mathbf{K}_{11}^{(e)} + \left(\frac{\overline{\mathbf{w}}^{(e)}}{\partial \xi_m^{(e)}}\right)^T \mathbf{C}_{22}^{(e)} \mathbf{K}_{22}^{(e)} \\ &\quad + \left(\frac{\overline{\mathbf{w}}^{(e)}}{\partial \xi_m^{(e)}}\right)^T \mathbf{C}_{33}^{(e)} \mathbf{K}_{33}^{(e)} + \left(\frac{\overline{\mathbf{w}}^{(e)}}{\partial \xi_m^{(e)}}\right)^T \mathbf{C}_{12}^{(e)} \mathbf{K}_{12}^{(e)}, \end{aligned} \tag{A-13}$$

For sensitivities to the densities in Equation (A-12), we recall that the vectors $\mathbf{C}_{ij}^{(e)}$ defined in Equation (5-8b) contain elements that are functions of the densities themselves. Deriving the k-th component vector with respect to an arbitrary density $\rho_m^{(e)}$ yields

$$\frac{C_k^{(e)}}{\partial \rho_m^{(e)}} = \begin{cases} \dfrac{\partial C_m(\rho_m^{(e)})}{\partial \rho_m^{(e)}} & \text{if } k = m, \text{ and} \\ 0 & \text{otherwise,} \end{cases} \tag{A-14}$$

where we dropped the implied (ij) index for readability.

In this work, we fitted the homogenized elasticity tensor components to polynomial data, so their derivative with respect to the density comes from Equation (3-51), which gives

$$\frac{\partial C_m(\rho_m^{(e)})}{\partial \rho_m^{(e)}} = \sum_{n=1}^{N_{\text{fit}}} n c_n \left(\rho_m^{(e)}\right)^{n-1}. \tag{A-15}$$

To determine the derivative of the normalized weight vector with respect to $\xi_m^{(e)}$, we derive each component $\overline{w}_m^{(e)}$ separately. Deriving Equation (5-6) with respect to $\xi_m^{(e)}$ using the quotient rule yields

$$\frac{\partial \overline{w}_i^{(e)}}{\partial \xi_m^{(e)}} = \frac{\dfrac{\partial w_i^{(e)}}{\partial \xi_j^{(e)}} W^{(e)} - w_i^{(e)} \dfrac{\partial W_e}{\partial \xi_j^{(e)}}}{\left(W^{(e)}\right)^2}. \tag{A-16}$$

Since the DMO formula in Equation (5-5) has an operator that distinguishes if $k = i$ or not, its derivative becomes the following expresion:

$$\frac{\partial w_i^{(e)}}{\partial \xi_m^{(e)}} = \begin{cases} p\left(\xi_m^{(e)}\right)^{p-1} \prod_{k=1,k\neq i}^{M} \left[1 - \gamma\left(\xi_k^{(e)}\right)^p\right] & \text{if } i = j, \\ -\gamma p \left(\xi_i^{(e)}\right)^p \left(\xi_m^{(e)}\right)^{p-1} \prod_{k=1,k\neq i,m}^{M} \left[1 - \gamma\left(\xi_k^{(e)}\right)^p\right] & \text{if } i \neq j. \end{cases} \tag{A-17}$$

Finally, the last term related to the material selection flag comes from deriving Equation (5-7) with respect to $\xi_m^{(e)}$, so we get:

$$\frac{\partial W^{(e)}}{\partial \xi_m^{(e)}} = \sum_{i=1}^{M} \frac{\partial w_i^{(e)}}{\partial \xi_m^{(e)}}, \tag{A-18}$$

where the derivatives on the right-hand side come from Equation (A-17), finishing this derivation.

A.3
Weighted Displacement Norm Objective Function

In this section, the derivative of $\mathcal{F}$ in Equation (6-7) with respect to a design variable $\mathbf{z}$ is computed via the adjoint method. first adding a null term $\boldsymbol{\lambda}^T(\mathbf{f} - \mathbf{K}^T\mathbf{u})$ to the objective function, where $\mathbf{f}$ is the constant external load vector, and $\boldsymbol{\lambda}$ is the adjoint vector. Deriving $\mathcal{F}$ with respect to the i-th component of the design vector yields

$$\begin{aligned} \mathcal{F} &= (\Delta\mathbf{u}^*)^T \mathbf{W} \Delta\mathbf{u}^* + \boldsymbol{\lambda}^T(\mathbf{K}\mathbf{u} - \mathbf{f}) \\ \therefore \frac{\partial \mathcal{F}}{\partial z_i} &= \frac{\partial (\Delta\mathbf{u}^*)^T}{\partial z_i} \mathbf{W} \Delta\mathbf{u}^* + (\Delta\mathbf{u}^*)^T \frac{\partial \mathbf{W}}{\partial z_i} \Delta\mathbf{u}^* \\ &\quad + (\Delta\mathbf{u}^*)^T \mathbf{K} \frac{\partial \Delta\mathbf{u}^*}{\partial z_i} + \frac{\partial \boldsymbol{\lambda}^T}{\partial z_i}(\mathbf{K}\mathbf{u} - \mathbf{f}) \\ &\quad + \boldsymbol{\lambda}^T \left[\frac{\partial (\mathbf{K}\mathbf{u})}{\partial z_i} - \frac{\partial \mathbf{f}}{\partial z_i}\right]. \end{aligned} \tag{A-19}$$

Since $\overline{\mathbf{u}}^*$ is constant, $\partial \Delta\mathbf{u}^*/\partial z_i = -\partial \mathbf{u}^*/\partial z_i$. Moreso, both $\mathbf{K}\mathbf{u} - \mathbf{f}$ and $\partial \mathbf{f}/\partial z_i$ equals $\mathbf{0}$ owing to the equilibrium and $\mathbf{f}$ being a constant vector,

respectively. Hence,

$$\begin{aligned}\frac{\partial \mathcal{F}}{\partial z_i} &= -\frac{\partial \mathbf{u}^{*T}}{\partial z_i}\mathbf{W}\Delta\mathbf{u}^* + (\Delta\mathbf{u}^*)^T\frac{\partial \mathbf{W}}{\partial z_i}\Delta\mathbf{u}^* \\ &\quad - (\Delta\mathbf{u}^*)^T\mathbf{W}\frac{\partial \mathbf{u}^*}{\partial z_i} + \frac{\partial \boldsymbol{\lambda}^T}{\partial z_i}\cancelto{\mathbf{0}}{(\mathbf{f}-\mathbf{K}\mathbf{u})} \\ &\quad + \boldsymbol{\lambda}^T\left[\frac{\partial(\mathbf{K}\mathbf{u})}{\partial z_i} - \cancelto{\mathbf{0}}{\frac{\partial \mathbf{f}}{\partial z_i}}\right] \\ &= -(\mathbf{W}\Delta\mathbf{u}^*)^T\frac{\partial \mathbf{u}^*}{\partial z_i} + (\Delta\mathbf{u}^*)^T\frac{\partial \mathbf{W}}{\partial z_i}\Delta\mathbf{u}^* \\ &\quad - (\mathbf{W}^T\Delta\mathbf{u}^*)^T\frac{\partial \mathbf{u}^*}{\partial z_i} + \boldsymbol{\lambda}^T\frac{\partial \mathbf{K}}{\partial z_i}\mathbf{u} + \boldsymbol{\lambda}^T\mathbf{K}\frac{\partial \mathbf{u}}{\partial z_i}. \end{aligned} \tag{A-20}$$

Since $\mathbf{W}$ is an arbitrary weight matrix, rearranging Equation (A-20) yields

$$\begin{aligned}\frac{\partial \mathcal{F}}{\partial z_i} &= -\left[(\mathbf{W}+\mathbf{W}^T)\Delta\mathbf{u}^*\right]^T\left(\mathbf{L}^*\frac{\partial \mathbf{u}}{\partial z_i}\right) + (\Delta\mathbf{u}^*)^T\frac{\partial \mathbf{W}}{\partial z_i}\Delta\mathbf{u}^* \\ &\quad + \boldsymbol{\lambda}^T\frac{\partial \mathbf{K}}{\partial z_i}\mathbf{u} + (\mathbf{K}\boldsymbol{\lambda})^T\frac{\partial \mathbf{u}}{\partial z_i}. \end{aligned} \tag{A-21}$$

Here, we introduce a diagonal boolean matrix $\mathbf{L}^*$ that maps the chosen DOFs from the global system. Owing to the symmetry of $\mathbf{L}^*$, the first term can be rewritten as follows:

$$\begin{aligned}\left[(\mathbf{W}+\mathbf{W}^T)\Delta\mathbf{u}^*\right]^T\frac{\partial \mathbf{u}^*}{\partial z_i} &= \left[(\mathbf{W}+\mathbf{W}^T)\mathbf{L}^*\Delta\mathbf{u}\right]^T\left(\mathbf{L}^*\frac{\partial \mathbf{u}}{\partial z_i}\right) \\ &= \left[\mathbf{L}^*(\mathbf{W}+\mathbf{W}^T)\mathbf{L}^*\Delta\mathbf{u}\right]^T\frac{\partial \mathbf{u}}{\partial z_i}. \end{aligned} \tag{A-22}$$

Substituting Equation (A-22) into A-21 gives

$$\begin{aligned}\frac{\partial \mathcal{F}}{\partial z_i} &= -\left[\mathbf{L}^*(\mathbf{W}+\mathbf{W}^T)\mathbf{L}^*\Delta\mathbf{u}\right]^T\frac{\partial \mathbf{u}}{\partial z_i} + (\mathbf{K}\boldsymbol{\lambda})^T\frac{\partial \mathbf{u}}{\partial z_i} \\ &\quad + (\Delta\mathbf{u}^*)^T\frac{\partial \mathbf{W}}{\partial z_i}\Delta\mathbf{u}^* + \boldsymbol{\lambda}^T\frac{\partial \mathbf{K}}{\partial z_i}\mathbf{u} \\ &= \left[-\mathbf{L}^*(\mathbf{W}+\mathbf{W}^T)\mathbf{L}^*\Delta\mathbf{u} + \mathbf{K}\boldsymbol{\lambda}\right]^T\frac{\partial \mathbf{u}}{\partial z_i} \\ &\quad + (\Delta\mathbf{u}^*)^T\frac{\partial \mathbf{W}}{\partial z_i}\Delta\mathbf{u}^* + \boldsymbol{\lambda}^T\frac{\partial \mathbf{K}}{\partial z_i}\mathbf{u}. \end{aligned} \tag{A-23}$$

The term with $\partial\mathbf{u}/\partial z_i$ vanishes by setting the content within the first

parenthesis to $\mathbf{0}$:

$$\begin{aligned}\mathbf{0} &= -\mathbf{L}^*(\mathbf{W}+\mathbf{W}^T)\mathbf{L}^*\Delta\mathbf{u}+\mathbf{K}\boldsymbol{\lambda}\\ \mathbf{K}\boldsymbol{\lambda} &= \mathbf{L}^*(\mathbf{W}+\mathbf{W}^T)\mathbf{L}^*\Delta\mathbf{u}.\end{aligned} \tag{A-24}$$

The weight matrix adopted in this work is symmetric, thus $\mathbf{W}+\mathbf{W}^T = 2\mathbf{W}$. Assuming that $\mathbf{W}$ is invertible leads to

$$\boldsymbol{\lambda} = 2\mathbf{K}^{-1}\mathbf{L}^*\mathbf{W}\mathbf{L}^*\Delta\mathbf{u}. \tag{A-25}$$

Then, Equation (A-23) can be simplified to

$$\frac{\partial\mathcal{F}}{\partial z_i} = \boldsymbol{\lambda}^T\frac{\partial\mathbf{K}}{\partial z_i}\mathbf{u} + (\Delta\mathbf{u}^*)^T\frac{\partial\mathbf{W}}{\partial z_i}\Delta\mathbf{u}^*,. \tag{A-26}$$

For implementation purposes, the sensitivity may be further simplified by computing it components at element level. Deriving equation 3-39b with respect to an arbitrary ρ_{e^*} yields

$$\frac{\partial\mathbf{K}}{\partial\rho_{e^*}} = \sum_{e=1}^{N_e}(\boldsymbol{L}_e)^T\frac{\partial\mathbf{K}_e}{\partial\rho_{e^*}}\boldsymbol{L}_e = (\boldsymbol{L}^{e^*})^T\frac{\partial\mathbf{K}^{e^*}}{\partial\rho_{e^*}}\boldsymbol{L}^{e^*}, \tag{A-27}$$

which holds since only $\mathbf{K}^{e^*}$ depends on ρ_{e^*}. Therefore, equation A-26 can be computed at element level as

$$\frac{\partial\mathcal{F}}{\partial z_i} = \boldsymbol{\lambda}_e^T\frac{\partial\mathbf{K}_e}{\partial z_i}\mathbf{u}_e + (\Delta\mathbf{u}_e^*)^T\frac{\partial\mathbf{W}}{\partial z_i}\Delta\mathbf{u}_e^* \qquad \text{if } \mathbf{W}=\mathbf{W}(\boldsymbol{z}), \tag{A-28}$$

$$\frac{\partial\mathcal{F}}{\partial z_i} = \boldsymbol{\lambda}_e^T\frac{\partial\mathbf{K}_e}{\partial z_i}\mathbf{u}_e \qquad \text{otherwise}, \tag{A-29}$$

where

$$\begin{aligned}\mathbf{u}_e &= \boldsymbol{L}_e\mathbf{u}, \quad \mathbf{u}_e^* = \boldsymbol{L}_e\mathbf{u}^*,\\ \overline{\mathbf{u}}_e &= \boldsymbol{L}_e\overline{\mathbf{u}}, \quad \overline{\mathbf{u}}_e^* = \boldsymbol{L}_e\overline{\mathbf{u}}^*.\end{aligned}$$

Since we adopt a constant matrix as $\mathbf{W}$, we implement Equation (A-29). The derivatives for the stiffness matrix with respect to the design variable follow the steps described in Appendix A.2.